Long Distance Atom Photon Entanglement

Diplomarbeit

im Studiengang Diplom Physik

angefertigt an der Fakultät für Physik

der Ludwig-Maximilians-Universität München

Arbeitsgruppe Prof. Dr. Harald Weinfurter

von

Fredrik Hocke

München, den 2. Oktober 2007

Erstgutachter: Prof. Dr. H. Weinfurter
Zweitgutachter: Prof. Dr. E. Riedle

Contents

Chapter 1

Introduction

"Quantum mechanics is certainly imposing. But an inner voice tells me that it is not yet the real thing. The theory says a lot, but does not really bring us any closer to the secret of the Old One. I, at any rate, am convinced that He does not throw dice.", is a statement Albert Einstein wrote already in 1926 to Nils Bohr [1]. It expresses the doubts many physicist had in the early days of quantum mechanics in this new theory to be able to describe the world. Especially the Copenhagen interpretation, stated by Bohr and Heisenberg around 1927 led to vigorous discussions, because this probabilistic interpretation of quantum mechanics was contradictory to the common, deterministic physical interpretation of nature. In 1935, an additional question arose, when Einstein, Rosen and Podolsky (EPR) proposed their famous gedanken experiment, from which they concluded that quantum mechanics could not be the whole truth, because it not fulfilled the conditions they proposed to be essential for any complete physical theory: Realism and locality. This point of view inspired theories claiming that not all parameters were accessible experimentally and that these hidden parameters would be responsible for the outcome of a measurement, explaining the correlations of entangled particles. But the gedanken experiment proposed no experiment or measureable quantity to prove whether nature obeys these local hidden variable theories or not. The gedanken experiment based on non-separable two-particle states. The high correlation in the measurement results between these, so-called entangled states inspired EPR to their conclusion.

Inspired from a simplified version of the EPR-paradox derived by Bohm, who considered two spin-$\frac{1}{2}$ particles [2], Bell was the first to prove that, considering spin correlation measurements, a limit for certain expectation values exists if local hidden variable theories were right, whereas quantum mechanics can violate this upper bound [3]. Bell's inequality allowed for the first time to derive experiments testing the quantum theories.

The test of Bell's original inequality has among other equivalent formulations [4, 5, 6] been subject to many experiments. The first ones used a cascade decay in calcium atoms to create entangled photon pairs [7], improved experiments by Aspect et al. in the following years showed a very strong violation of Bell's inequality [8, 9].

The experiments so far were all subject to two loopholes, that as long as not closed, still allow to explain the correlations of entanglement with local realistic theories, although all outcomes of the measurements were in favor of quantum mechanics. The first one is the locality loophole, that claims the possibility of relativistic interactions of the different analyzers, used to perform the measurement [10]. The first experiment addressing this loophole was performed by Aspect et al. in 1982 by changing the measurement bases very fast but not randomly [11]. The first experiment really closing this loophole was performed in 1998 [12], changing the measurement bases of the spacelike separated analyzers randomly to exclude any possible exchange of information between them. This experiment was however still subject to the second loophole, the detection loophole. It states, that the performed measurements, all having very low detection efficiencies, do not represent the outcome of the whole ensemble. Thus although the outcome of an experiment is in favor of quantum mechanics, there still is the possibility that the system as a whole behaves according to local realism.

In 2001 Rowe et al. performed a test of Bell's inequality on entangled ions [13] having a much higher detection efficiency than the photon experiments and closed the detection loophole. But the ions where not spatially separated far enough to close the locality loophole. To rule out a local realistic description of nature, a final loophole free test of Bell's inequality closing both loopholes simultaneously is still outstanding.

A very promising idea to close both loopholes is the combination of the high detection efficiency of internal atomic states with a spacelike separation of the readout setups using photons as carrier of quantum information to distribute entanglement [14, 15]. A key ingredient therefore is the entanglement between atoms and photons, providing an interface between matter and light exploiting the advantages of both systems. Performing a Bell-state measurement on two photons being entangled with an atom each, the entanglement can be swapped onto the two atoms, which internal states can be read out very efficiently. The entanglement between matter and light has already been successfully proven by entangling an ion [16], a trapped single atom in a dipole trap [17] and a single atom in a cavity [18] with a photon, respectively. The entanglement swapping between two massive particles has been realized recently by Moehring et al. [19] stating with two entangled ion-photon pairs and generating an entangled ion pair. The ions were separated by one meter.

The simplest and mostly performed way for the entanglement swapping is to interfere the two photons on a beamsplitter and only considering the case when a coincident detection event occurs in both detectors. This method has already been successfully used to perform entanglement swapping with two entangled photon pairs, generated by spontaneous parametric down conversion [20]. The fidelity of this Bell state measurement and thus of the transfer of entanglement depends on different parameters like the arrival time of the photons, their frequency distribution, the beamsplitter and the detection time.

Thereby an upper bound for the fidelity of the entanglement swapping is given by the Bell state measurement.

In this thesis the link between the generation of an entangled atom-photon pair and the spatially separated photon analysis is presented to distribute entanglement between matter and light over long distances, using photons which have passed a 300 m single mode optical fiber. This is the first step to overcome the locality loophole. Together with the entanglement swapping of two atoms it will allow a final loophole free test of Bells inequality.

Overview One important problem occurring in the extension to long distances is the birefringence of the optical fiber, which guides the photon to the photonic Bell state measurement. Having a length of 300 m the birefringence of the fiber changes randomly due to temperature changes and vibrations. As a consequence the entanglement between the atom and the photon is destroyed. To minimize losses due to the random unitary transformation of the polarization of the photon, an active stabilization of the birefringence of the fiber is necessary. In the first chapter a setup capable to stabilize the polarization in an optical fiber with an accuracy of 99.8% is explained. The second chapter describes the setup to generate the entanglement between an atom and a photon [17] and the integration of the polarization control into this setup. First correlation measurements between an atom and a photon over long distances using the extendend setup are discussed, showing that the entanglement is maintained over this distance with a mean visibility of 0.75. Calculations to give the expected upper bound for the visibility of entanglement swapping and the experimental requirements are presented in the third chapter by analyzing two photon interference on a beamsplitter and its consequences for the Bell state measurement. In the fourth and last chapter, the results are summarized and an outlook is presented.

Chapter 2

Control of polarization in optical fibers

The transport of quantum mechanical information over long distances is a key element of quantum communication and information because single photons are ideal carriers of information. The information is e.g. encoded in their polarization, providing a quantum mechanical two level system. Besides free-space communication, light can also be efficiently sent over optical fibers. The remaining problem of these quantum channels is the time varying stress induced birefringence of optical fibers. This leads to depolarization, causing loss of the carried information. To prevent this loss, it is essential to be able to control the polarization in the fiber. In this section a setup is described to preserve polarization of light passing a 300m long fiber. First, a short introduction into the description of polarization is presented, then the different parts of the setup are explained, an algorithm to actively stabilize the polarization is developed, and, at the end of the chapter, experimental results are presented that show that the polarization in optical fibers can be maintained with very low residual errors.

2.1 Description of the polarization of light

A classical lightwave can be fully described by the evolution of its electric field. Except for the propagation direction, the frequency of the oscillation, the amplitude and the direction in which the electrical field points are the relevant degrees of freedom. For a plane wave the direction of the electrical field oscillation is perpendicular to the propagation direction and is called polarization direction (fig. 2.1). The most general description of the polarization properties of a plane wave, travelling in z-direction is given by a complex 2-dimensional vector, the so-called Jones vector [21]:

$$\mathbf{J} = \begin{pmatrix} E_x \\ E_y\, e^{i\varphi_1} \end{pmatrix} e^{i\varphi_2} = E_0 \begin{pmatrix} \cos\frac{\theta}{2} \\ \sin\frac{\theta}{2}\, e^{i\varphi_1} \end{pmatrix} e^{i\varphi_2} \, , \tag{2.1}$$

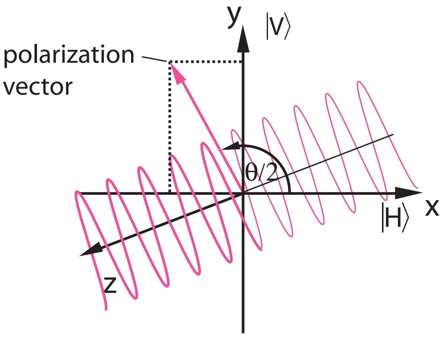

Figure 2.1: Schematic picture of the polarization of a plane wave travelling along the z-direction.

with $E_0 = E_x^2 + E_y^2$. We are not interested in the absolute intensities of light, so we choose $E_0 = 1$. The global phase φ_2 is not measurable in the case of a single wave and shall be omitted. The Jones vector reduces to:

$$\mathbf{J} = \begin{pmatrix} \cos\frac{\theta}{2} \\ \sin\frac{\theta}{2}\, e^{i\varphi_1} \end{pmatrix} \tag{2.2}$$

We define light as horizontally (vertically) polarized, when the polarization vector points into the direction of the x- (y-)axis. The quantum mechanical description of polarization is equivalent to the description of a two level system, that is described in a two dimensional $\mathbb{C}$-space as well:

$$|\Psi\rangle = \cos\frac{\theta}{2}\,|0\rangle + e^{i\varphi_1}\sin\frac{\theta}{2}\,|1\rangle \tag{2.3}$$

In case of polarization, $|0\rangle$ ($|1\rangle$) correspond to horizontal (vertical) polarization (we will also use $|H\rangle$ ($|V\rangle$)). This notation allows to represent every state $|\Psi\rangle$ as a point on a surface of a sphere with radius 1, called the Poincaré sphere (When dealing with other systems than photons, it is called Bloch sphere). The position of the state on the sphere is given by the spherical angles θ and φ_1 (fig. 2.2).

The three axes of the Poincaré sphere are defined by three bases, which are complementary in Jones space. Usually one chooses the x-axis to be the H/V-basis, where H (V) stands for horizontal (vertical) polarization. The y-axis represents the $+/-$-basis, where $+$ ($-$) means $+45^o$- (-45^o-) polarized light. Finally the z-axis gives the circularly polarization basis, with the notation R/L for right/left-circular polarization. Measuring in one of these bases gives maximal uncertainty of the others, e.g. projecting the polarization of a photon into the H/V basis, we loose all information of the state with respect to the other two bases. The three bases have the following properties:

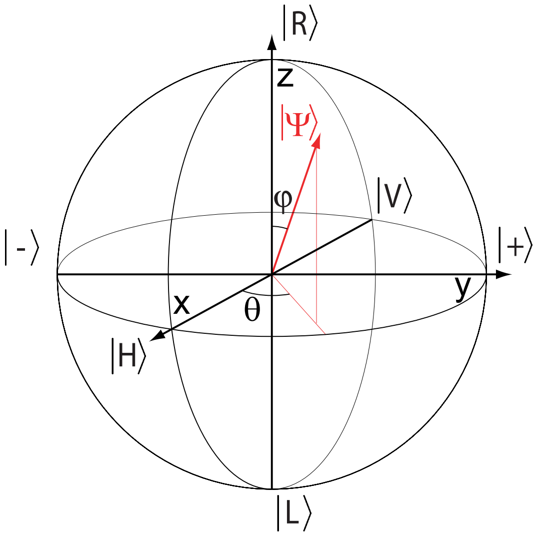

Figure 2.2: Representation of a polarization state on the so-called Poincaré sphere. Any possible state $|\Psi\rangle$ can be represented as a point on the surface of the sphere, defined by the angles θ and φ_1.

$$|+\rangle = \frac{1}{\sqrt{2}}(|H\rangle + |V\rangle) \tag{2.4}$$

$$|-\rangle = \frac{1}{\sqrt{2}}(|H\rangle - |V\rangle) \tag{2.5}$$

$$|R\rangle = \frac{1}{\sqrt{2}}(|H\rangle + \imath|V\rangle) \tag{2.6}$$

$$|L\rangle = \frac{1}{\sqrt{2}}(\imath|H\rangle + |V\rangle) \tag{2.7}$$

The vectors on the sphere expressed in Cartesian coordinates are called Stokes vectors and read:

$$\mathbf{S} = \begin{pmatrix} S_1 \\ S_2 \\ S_3 \end{pmatrix}. \tag{2.8}$$

S_i are the projections on the $x-, y-$ and z-axis respectively. This representation allows to map the $\mathbb{C}^2$-space on a three three dimensional $\mathbb{R}$-space. Working with the Poincaré sphere, one has to consider the fact, that on the Poincaré/Bloch sphere the azimuthal angle is doubled as seen already in eqn. [2.3], where the angles are given by $\frac{\theta}{2}$.

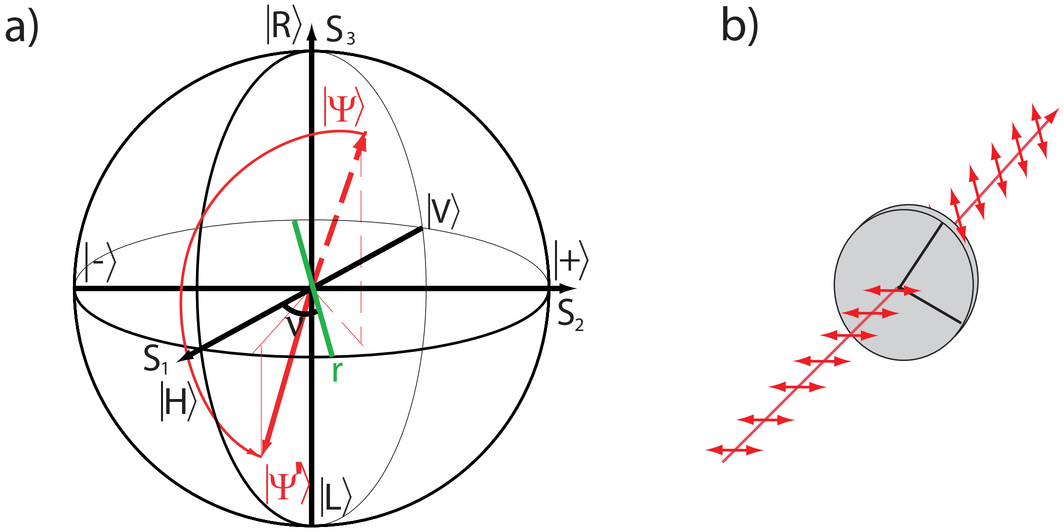

Figure 2.3: a)Visualization of the effect of a $\lambda/2$-wave plate at angle ν on a state $|\Psi\rangle$, transforming it into the state $|\Psi'\rangle$ by rotating it about an angle of π around $\mathbf{r}$. b) shows the effect of a half wave plate in the real space.

2.1.1 Manipulation of polarization

The most important linear optical components used to manipulate polarizations are retardation plates. These plates consist of a birefringent material with a well defined thickness, giving rise to a phaseshift of λ/x between the part of the light polarized parallel to the extraordinary axis and the perpendicular polarization, because of the different group velocities of light within these polarization components [22]. Therefore they are also called λ/x wave plates or, in case of $x = 2(4)$ half (quarter) wave plates. A transformation induced by such a plate is unitary and can be visualized in Stokes space [21] as a rotation. The angle ν of the waveplate, defined as the angle between the optical axis and the polarization vector of $|H\rangle$, gives a rotation-axis in the S_1S_2 plane, with an angle 2ν with respect to the S_1 axis. The transformation by the λ/x-plate thus can be visualized as a rotation of the polarization state by $2\pi/x$ around this axis (see fig. 2.3).

2.2 Polarization drifts

Nowadays, optical fibers are the most used carrier of light, giving the possibility to guide light over large distances. Problems can arise, when the information is not encoded in the intensity of the light but in its polarization state, since optical fibers are object to stress induced birefringence. Typically one has no information about the orientation of the refractive axes, as it depends not only on the material of the fiber, but also on the un-

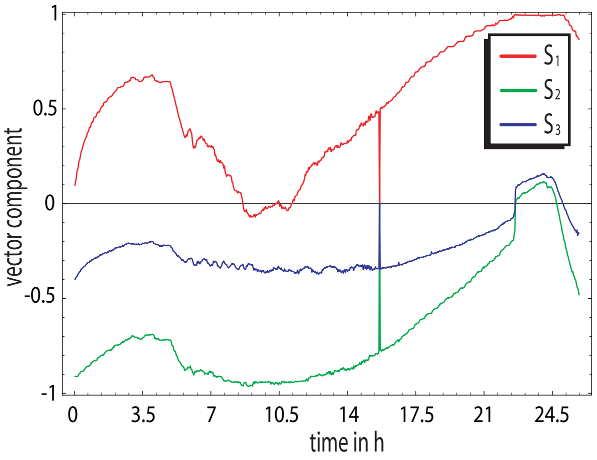

Figure 2.4: Drift of the polarization in a 300 m long fiber in our laboratory with a temperature varying about 5^o. The spikes at 15.75 h result from one measurement that failed.

known imperfections and the way the fiber is stressed. As a consequence the polarization of the light is randomly rotated on its way through the waveguide. As the fiber is subject to temperature changes and vibrations, this random rotation is time dependent (see fig. 2.4).

There are commercially available, polarization maintaining optical fibers, that can conserve the polarization (but have a higher attenuation). This kind of waveguide does not suit our purpose as it only preserves two orthogonal polarizations (e.g. $|H\rangle$ and $|V\rangle$). But as the phase between these polarization states is not maintained and still subject to e.g. temperature changes, any superposition states of $|H\rangle$ and $|V\rangle$ will still be changed randomly. To prove entanglement, or to realize entanglement swapping it is necessary to maintain all polarization states, therefore we have build a setup capable of conserving the polarization state on a timescale suitable for our experiment. To test the consequences of temperature changes in a laboratory we sent a well defined input polarization through a 300 m single mode fiber (type 630 HP from Nufern), as this is the distance we will use in the experiment. We measured the output polarization over approximately 24 h, with a temperature varying about approximately 5^o (fig. 2.4). The input state drifts approximately about 20^o/h in Stokes space, what results in an overlap[1] of 98% between the state measured at t_0 and $t_0 + 1$ h. This makes measurements lasting longer than 1 h impossible, as too much information is lost. Thus the control of the drifts of the birefringence of an

---

[1] the overlap between two states $|\Psi_1\rangle$ and $|\Psi_2\rangle$ in Jones space is defined by $|\langle\Psi_1|\Psi_2\rangle|^2$ and is used as a measure for probability.
The overlap of states in the Poincaré space is no such measure, because orthogonal states, like $|H\rangle$ and $|V\rangle$, have an overlap of -1 in the Stokes vector description. From the above equation for the overlap follows, since the angles on the Poincaré sphere are doubled with respect to the ones of the Jones description and

optical fiber is necessary to maintain the polarization state.
An additional test was made by measuring the polarization every 10 minutes and determining the drift in this time interval, because this will be the typical time between two polarization control runs. We measured that the polarization on average drifts in 10min about 4.291^o in Jones space, resulting in an overlap of 99.44%.
Finally, we tested the wavelength dependency of the fibers birefringence in a small region of $6.8GHz$ around the frequency we are working at. Changes of the fiber's birefringence were not observed.

2.3 Scheme for active stabilization of polarization in a fiber

As we have seen in the last section the control of the birefringence is of fundamental interest when information, encoded in the polarization of light has to be sent over long distances using optical fibers. In this section a scheme allowing to maintain the polarization in a fiber and to control it is presented. The setup is working at a wavelength of 780nm, corresponding to the D_2-line of ^{87}Rb .

2.3.1 General idea

The process of maintaining the polarization of light guided through a fiber can be divided into two main steps (see fig. 2.5:

- The measurement of the effect of the fiber at a suited wavelength. In order to measure the full effect of the fiber, two complementary polarizations of reference light are needed (two polarizations from non commmuting bases would be sufficient, but the visibility is best for complementary polarizations), as any transformation introduced by the fiber can be described using two variables (See next section).
- The decision what has to be done in the next step. Therefore an algorithm, capable of handling the measured data and being able to decide which transformation to apply to compensate the birefringence of the fiber is necessary. The transformation itself is realized with a so-called fiber polarization controller.

---

knowing the angle α between two Stokes vectors to be

$$\frac{\mathbf{S}_1\mathbf{S}_2}{|\mathbf{S}_1|\,|\mathbf{S}_2|} = \cos\alpha \ , \tag{2.9}$$

that the overlap P between two states is then given by

$$P = \cos^2(\alpha/2) = \cos^2(\frac{1}{2}\ \arccos\left(\frac{\mathbf{S}_1\mathbf{S}_2}{|\mathbf{S}_1|\,|\mathbf{S}_2|}\right)) \tag{2.10}$$

The normalization is done since the errors in the measurement result in a length of the Stokes vector different from 1.

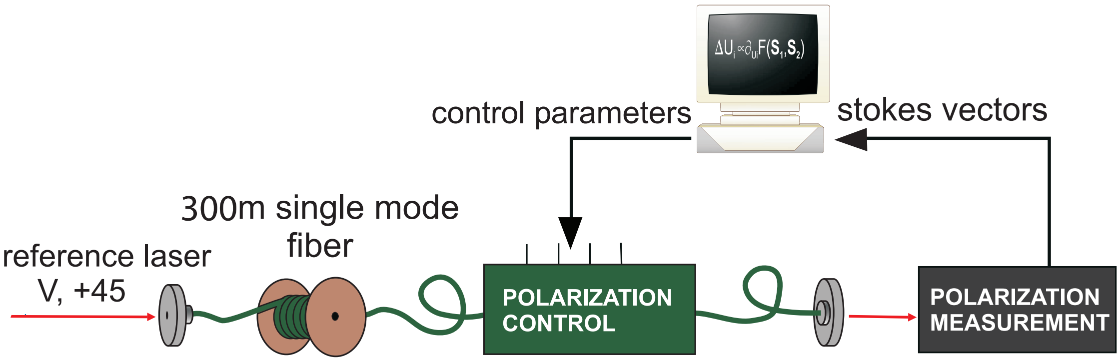

Figure 2.5: Schematic setup to maintain the polarization in a fiber

In the following subsections the components needed to realize the above steps are presented.

2.3.2 Generation of two complementary reference polarizations

For the measurement of the polarization transformation of the optical fiber, two complementary polarization directions are necessary. Stabilizing two orthogonal polarizations, what is the first intuitive choice for reference polarizations, is not sufficient.

This can be seen easily, using the notation of eqn. 2.3. The effects on the polarization state by a fiber are described by unitary transformations. A general unitary transformation (writing $|\Psi\rangle$ as a column vector) is defined by:

$$\hat{U} = \begin{pmatrix} e^{i\beta}\cos\alpha & \sin\alpha \\ -\sin\alpha & e^{-i\beta}\cos\alpha \end{pmatrix} \tag{2.11}$$

If we now suppose that we maintain $|V\rangle$ and $|+\rangle$, which are two complementary polarizations, a necessary and sufficient condition that all other polarization states are maintained is:

$$\begin{array}{rcll} \hat{U}\,|V\rangle & = & |V\rangle & (1) \\ \hat{U}\,|+\rangle & = & |+\rangle & (2) \end{array} \Leftrightarrow \hat{U} = \mathbb{1} \tag{2.12}$$

The left hand side clearly follows from the right hand side, what remains to show is the other direction. Condition (1) gives with above definition of $\hat{U}$:

$$\hat{U}\,|V\rangle = -\sin\alpha\,|H\rangle + e^{-i\beta}\cos\alpha\,|V\rangle = |V\rangle\ . \tag{2.13}$$

what yields $\alpha = 0$. Using this result in condition (2) gives:

$$\hat{U}\,|+\rangle = \frac{1}{\sqrt{2}}(e^{i\beta}\,|H\rangle + e^{-i\beta}\,|V\rangle) = |+\rangle\ . \tag{2.14}$$

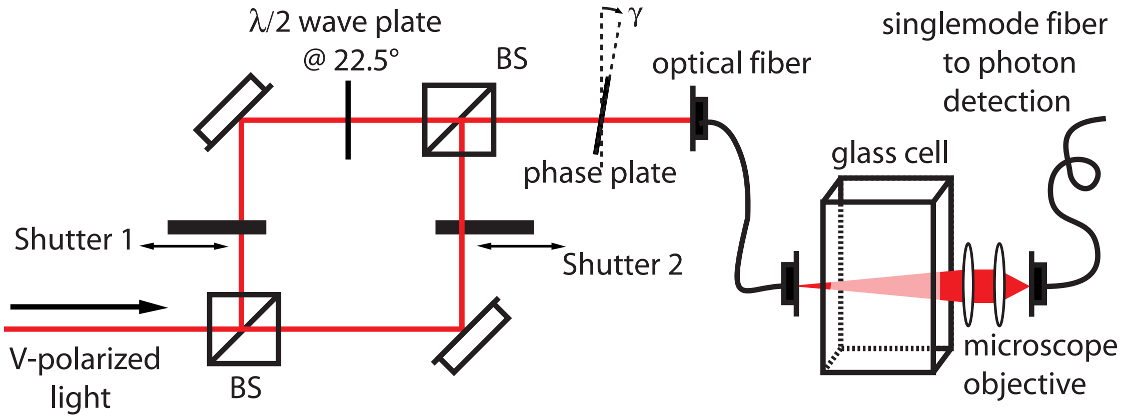

Figure 2.6: Schematic setup for the creation of two complementary reference polarizations that are alternately sent to the experimental setup and finally is coupled into the optical fiber to the photon detection setup, where the polarization analysis is located.

It follows $\beta = 0$. Thus it is shown that $\hat{U} = \mathbb{1}$, what means that no unitary rotation except from $\mathbb{1}$ can take place if these two polarizations are maintained.
If we chose $|H\rangle$ instead of $|+\rangle$ as second reference polarization, β would not have to be zero, what is seen by calculating $\hat{U}\,|H\rangle$ for $\alpha = 0$, thus a rotation can still take place, what proves that two orthogonal polarizations are not sufficient.

Setup

In our experiment we use $|V\rangle$ and $|+\rangle$ as reference polarizations. These polarizations are prepared with respect to a reference frame that defines all polarizations necessary for the main experiment. For this purpose we use light from a frequency stabilized laser diode at a wavelength of 780 nm. The two polarizations are joined with a beamsplitter. The $|V\rangle$-polarized light passes the setup without changes, as all optical components have the H/V-basis as eigenbasis. The $|+\rangle$ reference beam gains additional phases when it is reflected from mirrors. These phases are neutralized with a so-called "phase plate" or "compensation plate", which is a birefringent crystal (e.g. a YVO crystal) oriented such, that $|H\rangle$ and $|V\rangle$ are the eigenpolarizations. By rotating the plate around an axis perpendicular to the propagation axis, the phase between the two eigenpolarizations can be adjusted (fig. 2.6). To switch between the two polarizations we use self-made shutters. They are made of a relay and a razors edge, allowing a maximum switching frequency of approximately 20 Hz. The light is then guided through a fiber to the main experiment, i.e. the glass cell of the vacuum chamber, where the single atom is trapped. The photons to be guided through the detection fiber are created in this cell. Therefore, when the reference polarizations are adjusted, the polarization of the reference beams is again tested immediately before passing the glass cell, i.e. this is the point where above mentioned reference frame is defined. Behind the glass cell the light is coupled into the optical fiber leading to the single photon analysis via the detection optics (see section 3.3.2).

The prepared polarization is tested with a highly accurate polarizer, The measurement was performed directly in front of the glass cell. For $|V\rangle$-polarization we obtain an extinction ratio of 99.88% and for $|+\rangle$-polarized light of 99.80%. Thus, the quality of the generated polarizations is very good and as the detection accuracy of the polarization analysis is of the same magnitude, high enough to serve as reference polarization.

2.3.3 Polarization analysis

An important part of the polarization stabilization process is the faithful measurement of the polarization. Thereby it is important to find a compromise between a reliable and fast measurement on the one side and being able to measure at low light intensities, since we have limited amounts of test light. High light intensities increase the danger of accidentally damaging the single photon detectors used for the single photon detection of the entanglement measurement. There are different ways to realize a full polarization tomography (e.g. [23, 24]). In our experiment, we chose for simplicity the straight forward way of measuring each Stokes parameter separately. There are also commercial polarimeters, but none of them is working at our wavelength of 780 nm.

Setup

The polarization tomography has to completely determine the polarization of the incoming light. The most straight forward way to measure the Stokes vector is to measure directly the components of the vector, i.e. to measure the polarization in three complementary bases, defining the axes in the Poincaré sphere. We choose the common bases H/V, $+/-$ and L/R onto which we project the polarization state. Therefore we split the light into three beams and perform a projective polarization measurement in each arm. In case of projecting onto H/V this is done by splitting up the light with a polarizing beamsplitter (PBS) and measuring the intensities of the two parts. To project onto $+/-$ we add a half wave plate at 22.5^o before the PBS and for projection onto R/L we add a quarter wave plate at 45^o (fig. 2.8).

The detectors in each arm project the polarization state onto the corresponding basis polarization. The according Stokes parameter follows from the normalized difference of the measurement results of the polarizing beamsplitter:

$$S_i = \frac{I_{i,T} - I_{i,R}}{I_{i,T} + I_{i,R}} \quad i \in \{1, 2, 3\} \tag{2.15}$$

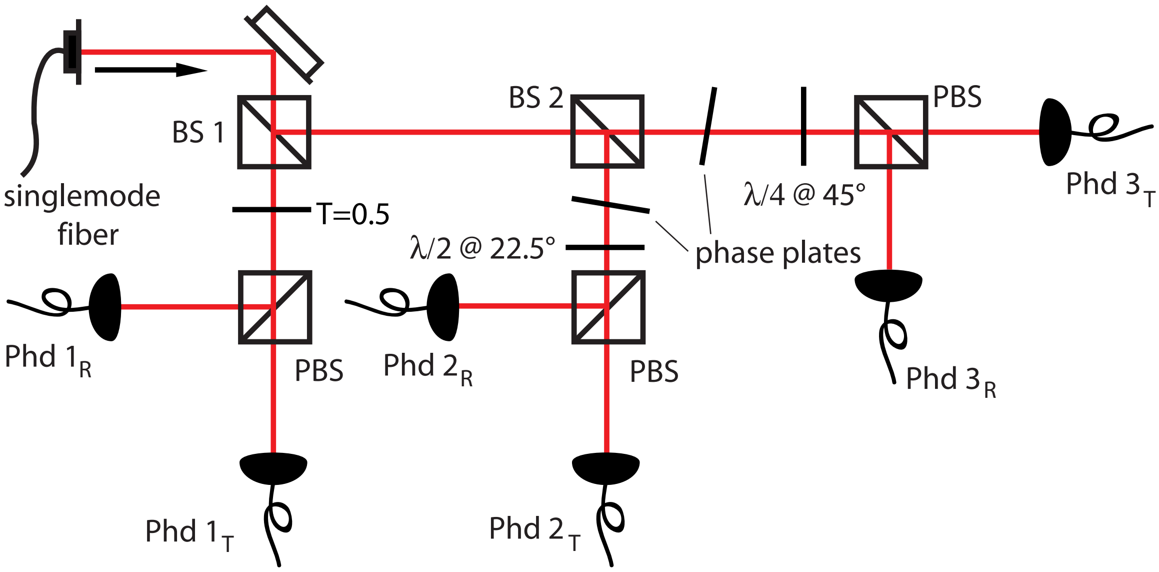

Figure 2.7: Scheme of the polarization tomography. The light is split up into three parts using the $50:50$ beamsplitters BS 1 and BS 2 in the analysis arms, where we perform a polarization measurement in the H/V-, $+/-$- and R/L-basis using a combination of half and quarter wave plates and polarizing beamsplitters (PBS). The photodiodes Phd 1 are measuring in H/V-basis, Phd 2 in $+/-$-basis and Phd 3 in R/L basis. The absorption plate in the first arm is used to guarantee same total intensities in each arm. The phase plates compensate the additional phase shifts of the polarization states when passing through the setup.

Photodetection of the incoming light

To monitor the intensity of the incoming light in each arm, photodiodes are used. In principle also single photon counters could be used, but in this case the measurement takes more time as the detectors have to gain reasonable statistics, whereas classical lightfields have negliable noise. The photodiodes are of the type BPW34 and have an efficiency of 0.589A/W. The photo current flowing through the diode when absorbing light is measured at a 1 MΩ resistor connected in series to the diode. Using a non-inverting amplifier this voltage is amplified by a factor of 10. In this way 1 μW power of the incoming light causes a voltage of about 5.89V. These voltages are read by a USB-adapter with an input range from -2V to 2V (we only use the range from $0-2$V), which defines a maximal input power of 0.34μW for each pair of photodiodes, since for the eigenpolarizations the light in one arm is directed onto one diode. The overall maximum power of the incoming light field is thus $4\times 0.35\mu\text{W} = 1.35\mu\text{W}$. Lower power gives the same results down to 0.05μW (see fig. 2.9). The duration of the polarization measurement is determined by the rise time

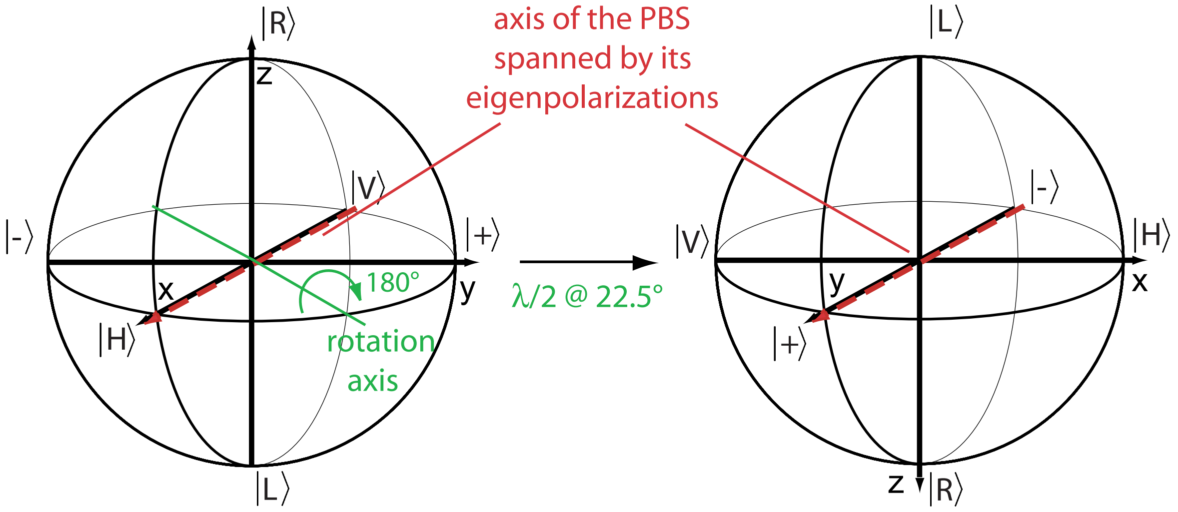

Figure 2.8: Scheme of the effects of a $\lambda/2$ wave plate at 22.5^o in front of a PBS. The polarization of the incoming light is rotated in that way, that the PBS separates the $|+\rangle$- and the $|-\rangle$-polarized part of the light

τ of the photodiodes. Which follows from the diode capacity and its resistance. With a resistance of 1MΩ and a capacity of 72pF we get a rise time of $\tau = 72\mu$s. The maximum measuring frequency is $F = \frac{1}{\tau} = 13,9$kHz.

Error sources

Errors during the measurement can be separated into errors from the electronics and errors of the optical components. The first one is dominated by electrical noise from the USB voltage converter (USB-ADC). The USB-ADC reader has a 12 bit resolution, making the digitalizing error 0.98 mV/bit, what defines the noise to be of this magnitude.
Looking at the components, there are mainly three sources that give rise to errors: The polarizing beamsplitters and the 50 : 50 beamsplitters and the wave plates. Of course there is some absorption for all components too, but this is polarization independent and thus negliable. The error arising from the PBSs is due to non-ideal splitting of H- and V-polarization. However, if we know the splitting ratios for H- and V-polarized light ($T_{H/V}, R_{H/V}$), one can show that from the measured values $I_{T,H}, I_{R,H}, I_{T,V}$ and $I_{R,V}$ (T, R indicating transmitted and reflected power respectively) the real power $I_{H,true}, I_{V,true}$ can be calculated:

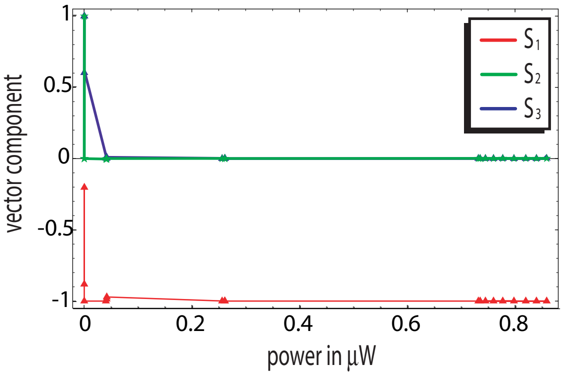

Figure 2.9: Measurement of polarization for different input intensities. The input polarization is $|V\rangle$. The dots represent the measured values.Every point was measured 3-4 times for better statistics. The measurement accuracy stays the same until the voltage output is comparable to the noise of the voltage reading unit (smaller 0.05μW).

$$I_{H,true} = \frac{1}{R_V T_H - R_H T_V}\left(R_V I_{T,H} - T_V I_{R,H}\right) \tag{2.16}$$

$$I_{V,true} = \frac{1}{R_V T_H - R_H T_V}\left(R_H I_{T,V} - T_H I_{R,V}\right). \tag{2.17}$$

This result is interesting, as it shows that no ideal polarising beamsplitters is needed. The only necessary condition is that the splitting ratio is polarization dependent. Equations 2.16 and 2.17 allow to completely eliminate errors arising from nonideal splitting ratios.

There are two non polarising beamsplitters in our setup, which are also not ideal $50:50$ beamsplitters. First, they do not have an exact $50:50$ splitting ratio. Except for the fact that in this case the intensity is not equal for all photodiode pairs this has no effect upon the measurement. The second problem is that the beamsplitters give rise to additional phases between the $|H\rangle$- and $|V\rangle$-polarized parts of the light. This can be compensated using compensation plates in each arm. When measuring in H/V-basis,this is not even necessary because here the additional phase has no effect. Additionally one has to consider that on reflection by the beamsplitter, $|+\rangle$-polarization is rotated into $|-\rangle$-polarization and vice versa (see sec. A.3). The third aspect is, that the splitting ratio is polarization dependent, so the polarization of the light is changed passing the beamsplitter. If we denote the transmitted fraction of the incoming horizontally polarized light with x (the reflected one is then $1-x$), and the vertical polarized fraction with y (and $1-y$ respectively), it follows that the overlap $|\langle\Psi_{passed}|\Psi_{initial}\rangle|^2$ with the initial polarization state is bigger than:

$$P_T = \frac{1}{2}\left|\frac{\sqrt{x}+\sqrt{y}}{\sqrt{x+y}}\right|^2 \tag{2.18}$$

$$P_R = \frac{1}{2}\left|\frac{\sqrt{1-x}+\sqrt{1-y}}{\sqrt{2-x-y}}\right|^2, \tag{2.19}$$

where $P_{T/R}$ is the probability to get the initial state after transmission/reflection when the input state was $|+\rangle$ or $|-\rangle$ (or any polarization state with equally distributed $|H\rangle$ and $|V\rangle$ fractions). These equations give the minimal overlap between the output polarization behind the beamsplitter and the initial state in front of it, when we assume that the maximal change of the polarization arises when the incident light is $|+\rangle$- or $|-\rangle$-polarized (or in any polarization state fulfilling above claim). The assumption that these polarizations are changed the most, when passing a beamsplitter is a very good approximation for the minimal overlap as long as the difference between x and y is not bigger than 0.2, which is true in our case. The beamsplitters used in our setup have the following properties (fig. 2.7):

$$BS1: \quad x = 0.550 \tag{2.20}$$

$$y = 0.495 \tag{2.21}$$

$$BS2: \quad x = 0.499 \tag{2.22}$$

$$y = 0.485 \tag{2.23}$$

They were chosen from a set of ten tested beamsplitters. With these values we obtain an overlap with the incoming polarization state of 99.93% for measuring in the H/V-basis, 99.91% for measuring in the $+/-$-basis and 99,91% for measurement in the R/L-basis. For the calculation of the last two overlaps one has to take into account, that the light passes both beamsplitters.

The main error from the waveplates originates from misalignment of about γ from the expected angle setting. This misalignment of the wave plates causes the detectors to measure a different state, resulting in an overlap of $\cos^2(2\gamma)$ between the wanted and the prepared one. In our case $\gamma \approx 0.5^o$ thus the overlap is around 99.99% and this error can be neglected.

Performance

To test the setup we prepared different polarization states oriented along three great circles (crossing the $\mathbf{S}_1$ and $\mathbf{S}_2$-, the $\mathbf{S}_1$- and $\mathbf{S}_3$- and the $\mathbf{S}_2$- and $\mathbf{S}_3$-axis, respectively)

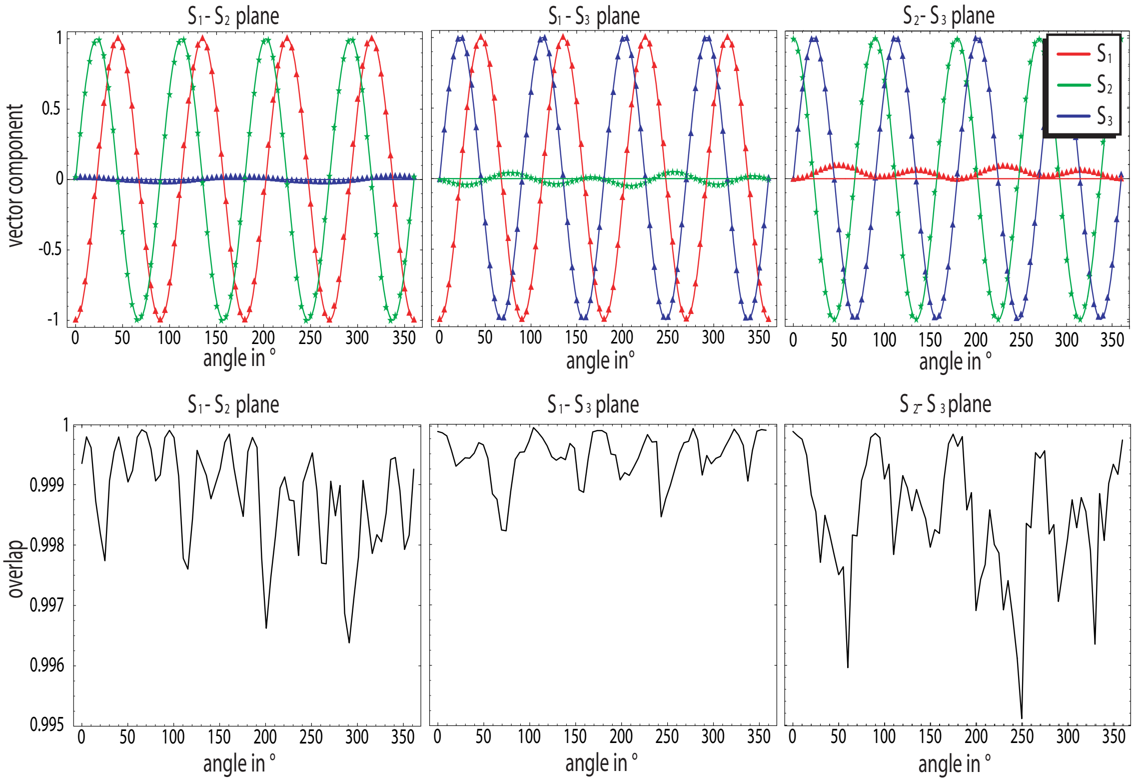

Figure 2.10: Results of measurement of the polarization along three great circles plotted versus the angle of the $\lambda/2$ wave plate, used to align the measured polarization. The dots are the measurement results and the solid lines result from the calculated values at that particular position of the wave plate. The graphs below show the overlap of the measured and the expected states.

by manually preparing the polarization with a polarizer, a half and a quarter wave plate, placed along the input laser beam before the polarization analysis. The results are shown in fig. 2.10. This measurement was done for a power of the incoming light of 0.73 μW. We expect a sinusoidal behavior of the two Stokes parameters defining the plane, where the great circle lies in, whereas the remaining parameter should be zero. Fig. 2.10 shows the measured data that follows this expected behavior.

Slight deviation is given by the Stokes parameter that is expected to be 0. It shows a small oscillation around zero with a maximum amplitude of 0.05 for the scanning of the great circle in the $\mathbf{S}_2 - \mathbf{S}_3$ plane. This is due to the fact that this parameter is most sensitive to alignment errors (proportional to sin around 0). But that is also the parameter affecting the measurement result the least.

We calculated the overlap of the prepared polarization state with the measured one

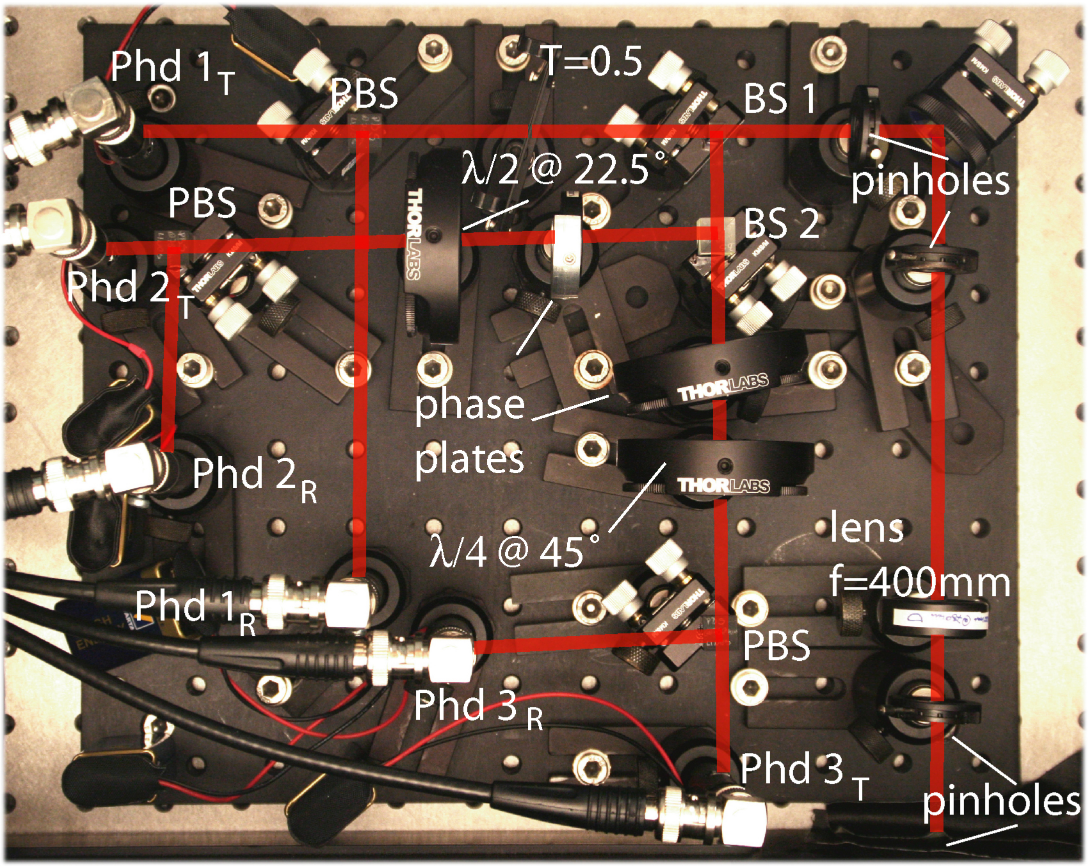

Figure 2.11: Photo of the polarization analysis setup. The light enters the setup via a pinhole at the lower right corner of the picture. The remaining pinholes are used to adjust the direction of the incoming beam. The lens focuses the beam, making its waist small enough to fully hit the photodiodes. In order to measure the full beam, we use a 400 mm lens to focus the beam from a waist of 3 mm down to a waist of approximately 30 μm much smaller then the 3 mm diameter of the photodetectors.

and than added the error occuring from misalignment of the input polarization reference system to the measurement reference frame by approximately 0.5^o around the $\mathbf{S}_3$-axis. This error occurs due to unevenness of the bread board the analysis setup is located on. From this calculation, we get an average overlap of 99.88% for the rotation in the $\mathbf{S}_1\mathbf{S}_2$-plane, 99.94% for the great circle in the $\mathbf{S}_1\mathbf{S}_3$-plane and 99.84% for the one in lying in the $\mathbf{S}_2\mathbf{S}_3$-plane. These values give a mean overlap of 99.87%, which is in good agreement with above error considerations.
As we want to use the polarizations $|V\rangle$ and $|+\rangle$ for compensation of the birefringence of the optical fiber these two polarizations are of special interest. From the measurement

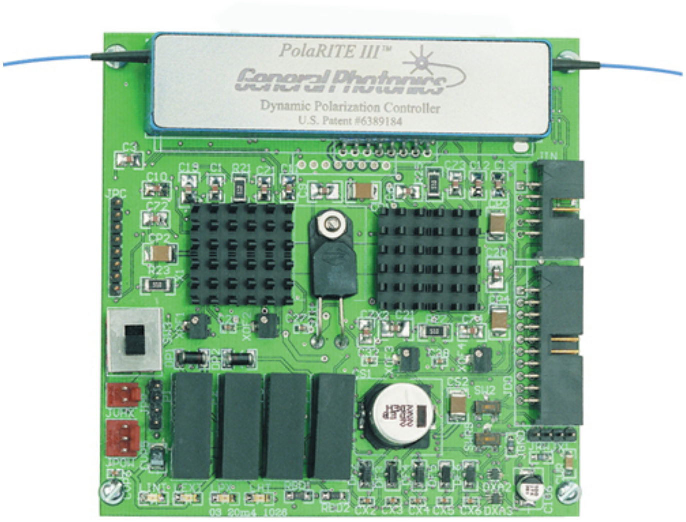

Figure 2.12: Photo of the polarization controller including the driver card (taken from the General Photonics website).

above we get an overlap for vertical polarized light of 99.96% and 99.85% for $|+\rangle$-polarized light[2].

The presented polarization analysis measures polarizations very accurate. Together with the reference polarizations it gives an ideal tool to measure the change of birefringence of the detection fiber.

2.3.4 Manipulation of polarization

The tool used to manipulate the polarization in the fiber is a ”mini dynamic polarization controller Polarite III” from General Photonics, including the driver card. It is preferable to waveplates because there are no losses due to coupling the light into and out of the fiber and it is much faster, as the rotation of the wave plates is very time consuming.

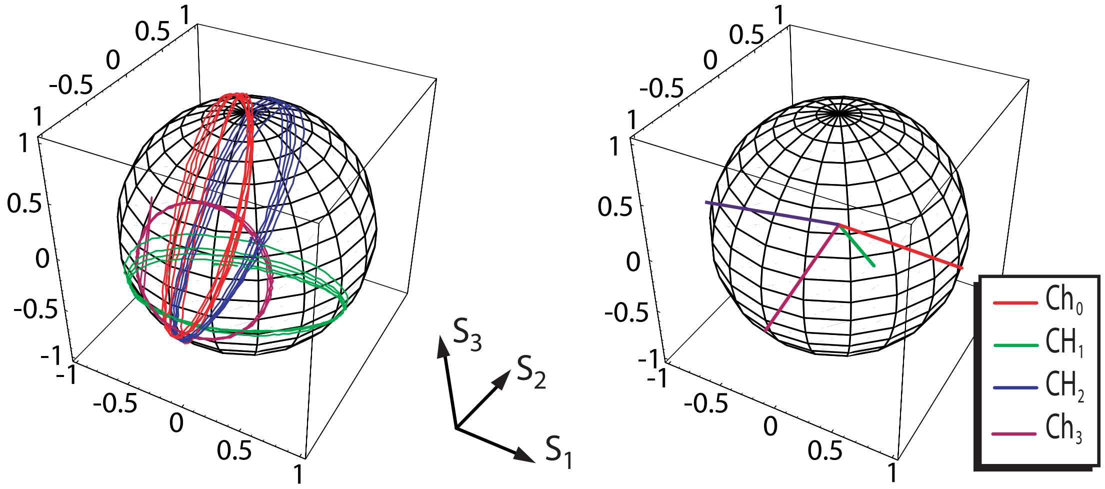

Figure 2.13: Picture of the polarization changes when the voltage at one squeezing element is manipulated and all others remaining at $0V$. The second picture shows the averaged rotation axes following from the circles on the left. The orientation follows also from the direction of the rotation with increasing voltage. The initial polarization state is the same for all four channels.

Working principle

The way the controller works is by applying pressure onto the fiber with four squeezing elements, controlled by external voltages. This changes the birefringence in a controlled way. If one visualizes the effect of one squeezing element on a certain polarization one can see, that it is rotated around a fixed axis on the Poincaré sphere, where the rotation angle depends on the applied voltage (fig. 2.13). Three of these elements are arranged in such a way that the axes are almost perpendicular to each other (input channels 0,1 and 3), channel 2 is parallel to channel 0. The squeezing elements create an overdetermined system, making resetfree manipulation of the polarization possible. Resetfree means that the effect of one squeezing element is compensated by the others, when it reaches its limits. The Stokes vector of the incoming polarization first is rotated by the first element, the new oriented vector is rotated around the axis defined by the second squeezer and so on. With this feature, the actions of the different squeezing elements depend on the action of the following ones, what arises from the fact that this kind of systems is non commutative.

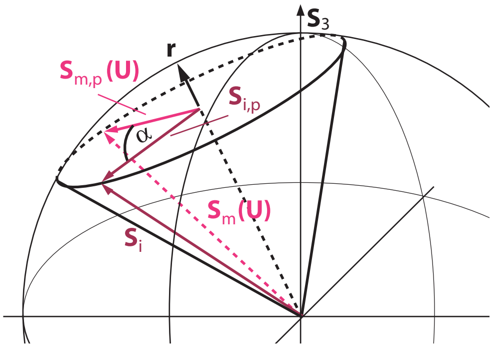

Figure 2.14: Schematic picture of the cone occurring when manipulating the voltage of one squeezing element. The rotation axis **r**, the initial Stokes vector $\mathbf{S}_i$, the measured one $\mathbf{S}_m$ and the rotation angle α are shown.

Properties

In this section we are going to present some experimental data and features of the coroller. The allowed input voltages for the squeezing elements lie between 0 V and 5 V. This voltage is internally amplified by a factor of 30. Our voltage output has a resolution of 13bit in a range from -10 to 10 V, thus we get a minimal resolution of 2.5 mV. The rotation angle per voltage is almost the same for every channel and is lying between 0.352^o/ mV (squeezer 1) and 0.472^o/mV (squeezer 0) on the Poincaré sphere (fig. 2.15). Thus the minimal angle of rotation lies between 0.86^o and 1.15^o on the Poincaré sphere. This was measured by applying voltage in steps of 0.01 V onto every squeezing element sequentially and measuring the new polarization. The rotation axis was calculated from the measured polarization changes (because the initial polarization is not perpendicular to the axis of the fiber squeezer no great circle is scanned). The rotation angle is defined as the angle between the initial and final part of the Stokes vectors perpendicular to the rotation axis (fig. 2.14). These vectors $\mathbf{S}_{i,p}$ and $\mathbf{S}_{m,p}$, representing the perpendicular part are calculated by:

$$\mathbf{S}_{i/m,p} = \mathbf{r} \times (\mathbf{S}_{i/m} \times \mathbf{r}) \ , \tag{2.24}$$

where the normalized vector **r** defines the rotation axis. The angle α can be calculated, using the scalar product of these two vectors. The resulting formula simplifies to:

$$\alpha(U) = \arccos\left(\frac{(\mathbf{S}_i \times \mathbf{r})(\mathbf{S}_m(U) \times \mathbf{r})}{|\mathbf{S}_i \times \mathbf{r}|\ |\mathbf{S}_m(U) \times \mathbf{r}|}\right) , \tag{2.25}$$

---

[2] A small detuning of the reference light of about $0.1 - 1$ nm already gives rise to measurable errors in the polarization analysis. For the future experiment however this poses no problem because we used a laser light field locked to the atomic transition in order to obtain the reference light.

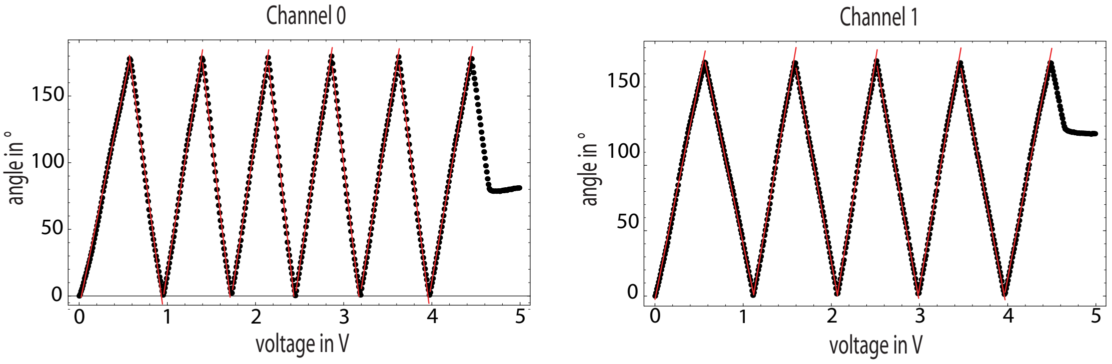

Figure 2.15: Measurement of the dependence of the rotation angle on the applied voltage for two channels of the polarization controller. We calculate the angle from eqn. 2.25, so only angles between 0^o and 180^o can occur. The dots are the measured values and the red lines are linear fits. The kinks at the end of the measurement arise because the squeezing elements saturate.

where $\mathbf{S}_i$ is the initial Stokes vector and $\mathbf{S}_m(U)$ the measured one for applied voltage U.

Stability

The stability of the adjusted polarization is also of fundamental interest. On large timescales, up to an hour, no drift of the polarization was observed. The short-time behavior is also interesting because it limits the time-interval between two adjustments of the polarization and therefore defines the maximum speed of our polarization control algorithm. Here the adjusted polarization remains stable on timescales bigger than 1 ms (the timescale of one polarization measurement), except when the voltage on one channel is changed. Fig. 2.16 shows a measurement of the short time drifts of the polarization immediately after changing the voltage from 0 V to 1.5 V at channel 0. One observes, that the polarization drifts for approximately 4 ms after applying the voltage. The measured drifts lie between 0.38^o and 7.57^o in Stokes space. When the voltage changes are smaller, this drift becomes smaller. Because the change is largest during the first microsecond and the remaining drift can be neglected when the voltage changes are very small, what is true for the polarization control algorithm. The algorithm waits for 1 ms every time the polarization is changed before measuring the changed polarization.

Bandwidth

The bandwidth with which the polarization can be manipulated is about 20kHz (3dB) for every squeezer. This was tested by applying a sawtooth voltage with an offset of 0.2V with an amplitude of 0.1V and measuring the effect on the polarization for increasing

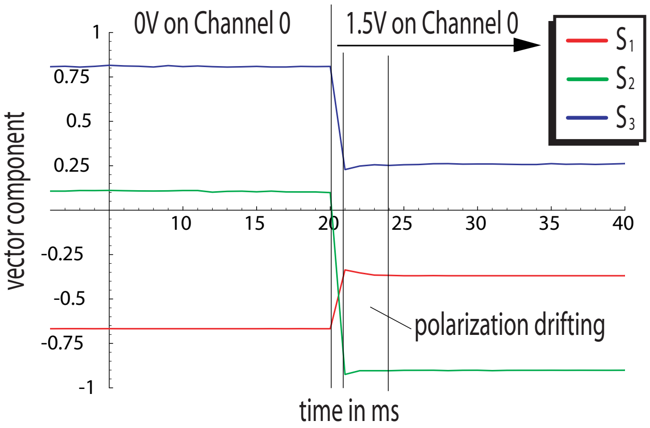

Figure 2.16: Measurement of the drift of the polarization after a sudden voltage change from 0 V to 1.5 V on channel 0.

frequencies.

2.4 Algorithm to maintain polarization

The previous section showed that we are able to measure the effect of a fiber onto two complementary polarizations with high accuracy. The next problem is to find the optimal set of parameters for the fiber controller that exactly compensates the transformation of the fiber in order to maintain the polarization of the light passing it. One possibility to realize this would be to analyze the transmitted polarization states, allowing to calculate the transformation matrix of the fiber. In the next step the parameters of the controller would have to be set accordingly to compensate this transformation. The exact calculation of the parameters is very difficult due to the lack of knowledge of the axes of the fiber controller, because the input polarizations at the controller are unknown (results from the long detection fiber, we only know the alignment of the axes relative to another). In principle these axes can be measured, but this takes time and the resulting system of equations is complex and also takes too much time to be solved.

The second method uses the principle of a gradient descent. We define a measure that gives the deviation of the measured polarizations behind the fiber from the respective input states. Then the voltages of the squeezers are varied slightly to determine the direction in which this deviation decreases. Then the parameters are changed by a small amount towards the optimal direction. This process is repeated until the output polarizations are equal to the input polarizations.

The advantage of this method is that no equations have to be solved, the electronic realization is simple and errors, occurring while adjusting the polarization are compensated immediately in the next iteration steps. Therefore we have chosen this way of maintaining the polarization. Additionally, in future this method could possibly be implemented in full electronic way which would allow a much faster compensation.

2.4.1 Definition of a measure

For the implementation of an optimization algorithm the first step is to define a measure, that gives the deviation of two polarization states from their set values, i.e. from the values of the Stokes vectors of the two reference polarizations. The function has to depend on the two input and output polarization states. For the allowed parameter set the function must be monotonous to make sure that there are no local extrema and the point where the two output polarizations are equal to the input must be a global minimum. A function which fullfills these conditions is the following one:

$$f(\mathbf{S}_{m1}, \mathbf{S}_{m2}) := |\mathbf{S}_1 - \mathbf{S}_{m1}|^2 + |\mathbf{S}_2 - \mathbf{S}_{m2}|^2 = \sum_{i=1}^{3} (S_{m1,i} - S_{1,i})^2 + (S_{m2,i} - S_{2,i})^2 \ , \quad (2.26)$$

where $\mathbf{S}_{m1}, \mathbf{S}_{m2}$ are the measured Stokes vectors and $\mathbf{S}_1, \mathbf{S}_2$ are the values we want to reach for the two polarizations respectively.
The function f has a global minimum $f = 0$ at the point $(\mathbf{S}_{m1}, \mathbf{S}_{m2}) = (\mathbf{S}_1, \mathbf{S}_2)$, $0 \leq f \leq 1$ and it is monotonously growing when the overlap between input and output states becomes smaller. In the following we shall call f the error function.

2.4.2 Calculation of the gradient of the error function

The next step is to find an algorithm to minimize the error function. Since we do not know the rotation axes of the polarization controller, the polarizations can not easily be changed in a certain direction. Instead we use the fact that we implicitly are given the errorfunction as a function of the voltages applied on the different channels of the polarization controller,
$f(\mathbf{S}_{m1}(U_0, U_1, U_2, U_3), \mathbf{S}_{m2}(U_0, U_1, U_2, U_3)) = f(U_0, U_1, U_2, U_3)$. Thus we can obtain the gradient for each set of voltages This gradient is estimated from the differential quotient in this four dimensional voltage space by applying a voltage, slightly varied about ΔU_i at every channel of the controller one after another, according to

$$(\nabla f)_i(\mathbf{U}) \approx \frac{f(\mathbf{U} + (0, .., \Delta U_i, .., 0)) - f(\mathbf{U})}{\Delta U_i} \ ; \quad i \in \{0..3\} \quad (2.27)$$

2.4.3 Correspondence of the error function to the error in the polarization

In this section we will present results achieved with the final setup, that is already implemented in the main experiment. First, we give an estimation what the value of the error function means in the worst case for the deviation of the two input polarization states from their setpoints. For small values of the error function, the biggest error for one of the input polarizations is when the other state matches perfectly the setpoint. Let the 45^o-polarized input polarization (i.e. $\mathbf{S}_2 = \mathbf{S}_{45}$) be perfectly maintained passing the fiber, i.e. $\mathbf{S}_{m2} = \mathbf{S}_{45} = (0, 1, 0)$. The deviation of the first lightfield from its vertically polarized input polarization (i.e. $\mathbf{S}_1 = \mathbf{S}_V = (-1, 0, 0)$) follows then from a rotation by an angle of ϵ around the axis defined by $\mathbf{S}_{45}$. It follows for the error function:

$$\begin{aligned} f(\mathbf{S}_{m1}, \mathbf{S}_{m2}) &= (S_{m1,1} + 1)^2 + (S_{m1,2} - 0)^2 + (S_{m1,3} - 0)^2 + (S_{m2,1} - 0)^2 + (S_{m2,2} - 1)^2 + (S_{m2,3} - 0) \\ &= (S_{m1,1} + 1)^2 + S_{m1,3}^2 = (1 - \cos\delta)^2 + (1 - cos^2\,\delta) = 2 - 2cos\,\delta, \qquad (2.28 \end{aligned}$$

$$\begin{aligned} \text{where} \qquad & (S_{m1,1} = -\cos\,\delta,\ S_{m1,2} = 0,\ S_{m1,3}^2 = 1 - S_{m1,1}^2) \\ \Rightarrow \epsilon &= \arccos(1 - \frac{1}{2} f(\mathbf{S}_{m1}, \mathbf{S}_{m2})) \qquad (2.29 \end{aligned}$$

The angle by which the two input polarizations are rotated when passing through the fiber is smaller than ϵ on the Poincaré sphere and smaller than $\frac{1}{2}\epsilon$ in Jones space. This means the overlap with the initial polarization state is better than $\cos^2(\frac{1}{2}\epsilon)$. We will use these values as an upper bound for the error of the polarization control.

2.4.4 Minimizing the error function

The locally determined gradient ∇f can be used to minimize f by changing the voltage $\mathbf{U} := (U_0, U_1, U_2, U_3)$ in small steps in the direction $-\nabla f$. For a monotonous function this procedure converges to the global minimum. This is realized in the following algorithm that is implemented in a C-program:

- Open the shutter to send light of the first reference polarization through the fiber.
- Measure the output polarization. Measure the output polarization for a slightly varied voltage $U_i + \Delta U_i$ at all channels, respectively (and reset it after the measurement).
- Close the shutter and repeat the procedure for the second reference polarization. From these 10 polarization measurements we obtain $f(\mathbf{U})$ and, according to sec. 2.4.2, $\nabla f(\mathbf{U})$

- Change each of the voltages in the opposite direction of $\nabla f(\mathbf{U})$, multiplied with a scaling factor $0 < D < 1$, which defines the step size[3]:

$$\mathbf{U} \rightarrow \mathbf{U} - D\nabla f(\mathbf{U}) \tag{2.30}$$

- If the new voltage is smaller than 0 V or bigger than 5 V, it is reset to 1 V.

- If the errorfunction $f(\mathbf{U})$ is smaller than a previously defined threshold ϵ_1, the gradient gets smaller and the convergence of the algorithm gets slower. Therefore, in this regime we implemented a direct calculation of the optimal setting to reach $f = 0$:

  - We want to directly reach the set values, i.e. minimize the error function within the next step, where the change of the voltage will be $D_g\Delta\mathbf{U}$:

$$f(\mathbf{U} + D_g\Delta\mathbf{U}) = 0 \tag{2.31}$$

  - The error function can approximated by the first element of its Taylor series:

$$0 = f(\mathbf{U} + D_g\Delta\mathbf{U}) \approx f(\mathbf{U}) + \nabla\mathbf{U} \cdot D_g\Delta\mathbf{U} \tag{2.32}$$

  - $\nabla\mathbf{U}$ is approximated by the differential quotient (eqn. 2.27).

$$0 \approx f(\mathbf{U}) + \sum_{i=0}^{3} \left[\frac{f(\mathbf{U} + (0,..,\Delta U_i,..,0)) - f(\mathbf{U})}{\Delta U_i} \right] D_g(\Delta\mathbf{U})_i \tag{2.33}$$

  - The change of the voltage will only be slightly different from the amount the voltage is varied to get the differential quotient. We can suppose $\Delta U_i = (\Delta\mathbf{U})_i$, because the variation to estimate the gradient will be approximately equal to the needed voltage change. It follows with $f(\mathbf{U}+(0,..,\Delta U_i,..,0)) - f(\mathbf{U}) =: \Delta f_i(\mathbf{U})$

$$D_g = -\frac{f(\mathbf{U})}{\sum_{i=0}^{3} \Delta f_i(\mathbf{U})} \tag{2.34}$$

  - We have estimated a new scaling factor that is calculated from the last measurement. Experimentally, additionally scaling down D_g has given better results (see table on next page).

- If the error function is below a second threshold ϵ_2 even smaller than ϵ_1, given by the resolution limit of the polarization control, the voltages are not changed at all, as it is likely that the measured gradient points in the wrong direction (see fig. 2.17).

---

[3] Too big steps lead to errors due to the approximation of the gradient only being valid in a very small region around $\mathbf{U}$

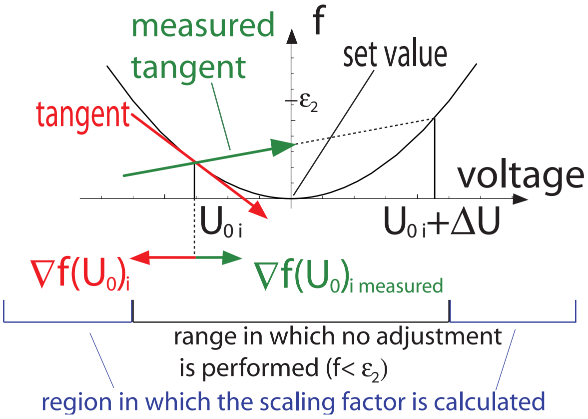

Figure 2.17: Scheme of estimating the differential quotient of the errorfunction f for values near to the setpoints in one dimension. Because the minimum could be passed by changing the voltage, it is possible that the measured gradient points in the wrong direction and the correction step will move away from the minimum. Therefore, within the region with $f < \epsilon_2$, no correction is performed. Within the first threshold (blue region), the calculated scaling factor D_g is used.

- repeat above procedure until the error function is below a third threshold f_{break} for 5 consecutive iterations ($\epsilon_1 > f_{break} > \epsilon_2$). This is done to exclude the function being below the threshold because of a measurement error and stopping the polarization control without stabilizing the birefringence.

- when reaching the condition to stop, the final voltage settings are stored into a file and used as the start values for the next time the polarization stabilization algorithm is used.

The optimal values of the three thresholds ϵ_1, f_{break}, ϵ_2, the scaling factor D and the step size ΔU_i to estimate the differential quotient were determined experimentally.

2.5 Characterization of the polarization control setup

2.5.1 Parameter-set of the algorithm

The parameter set was optimized manually with respect to the convergence, the iteration number and the stability. The following table shows the optimal values obtained from experimental tests:

INTENT	VARIABLE	VALUE	COMMENT
first threshold from which on the error function is linearly approximated	ϵ_1	0.01	resulting overlap with initial value is better than 99.74%
second threshold from which on the voltages are not corrected	ϵ_2	0.0008	resulting overlap with initial value is better than 99.96%
The value the voltage is changed to get the differential quotient	ΔU	20 mV 9 mV	if $f > \epsilon_1$ if $\epsilon_2 < f < \epsilon_1$
scaling factor for the change of the voltage	D	0.400 0.405	if $f > \epsilon_1$ if $\epsilon_2 < f < \epsilon_1$
termination condition $f < f_{break}$	f_{break}	0.008	-resulting overlap with initial value is better than 99.80% -has to be true for 5 consecutive iterations
allowed iterations	n_{run}	100	the polarization control is allowed to take max. 1min

2.5.2 Convergence and reliability

The most important property of the polarization control is the number of iterations necessary to get to the desired polarization value. Having adjusted the polarizations, it is necessary to know if the polarization control has converged to a stable point or if the set value was hit by accident. To show that the algorithm really converges the polarization control was running continuously for approximately 12 h. Fig. 2.18 shows the measured Stokes vector components over this measurement time. One observes a stable output for both reference polarizations except some peaks, arising from the fact that the shutters do not open or close exactly at the time they are supposed to. This feature arises from the high CPU load, which could not be lowered yet

The mean value of the errorfunction over the whole measurement is $f_{mean} = 0.00579$ with a standard deviation of $\sigma = 0.00018$. The value $f_{mean} = 0.00579 \pm 0.00018$ results in an mean overlap between 99.925% and 99.930%. Thus once the controller has adjusted the polarizations, they are maintained except from small variations around the set value and the maloperation of the shutters, which occurs on average every 15 min, displacing the polarization again for max. 20 iterations.

In a typical operation the polarization control starts with initial values slightly changed from optimum value, as the birefringence of the fiber is compensated every 10 min (for the typical drifts and the resulting overlap see sec. 2.2). There are two characteristics that

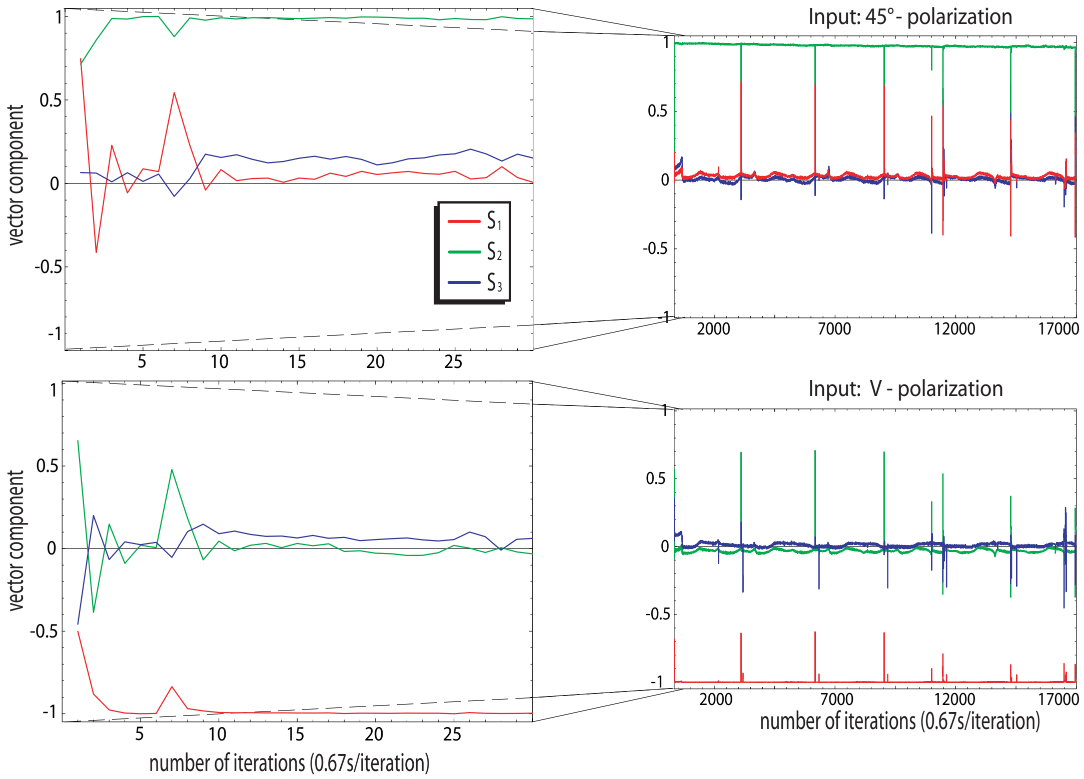

Figure 2.18: Part (3h) of a polarization control continuously running for 12h. The polarization states converge after 10 iterations to a region in which the error function is smaller than 0.02. Although sometimes measuring wrong values (all 15 minutes on average), the polarizations are maintained accurately. The errorfunction proves this fact, resulting in an average value of approximately 0.0058 (see fig. 2.19).

become interesting in this mode of operation:
How many iterations are needed to reach the stopping condition and which percentage of control runs converges at all. In fig. 2.18 and in fig.2.19 we see that the polarization has almost converged after 10 iterations, as it starts with a random value. After these 10 iterations the measured polarizations are in a region where the corresponding value of the error function is comparable to the typical start value of a polarization control when used every 10 minutes. Normally the iteration number lies in between $15 - 20$ iterations. This region, in which the drifting states are near to the input states (the value of the error function is smaller than 0.02) is reached every time whenever the polarization control starts with random values.
However from here on the input polarizations do not always consecutively reach the threshold f_{break} often enough within the allowed 100 iterations. In some measurements

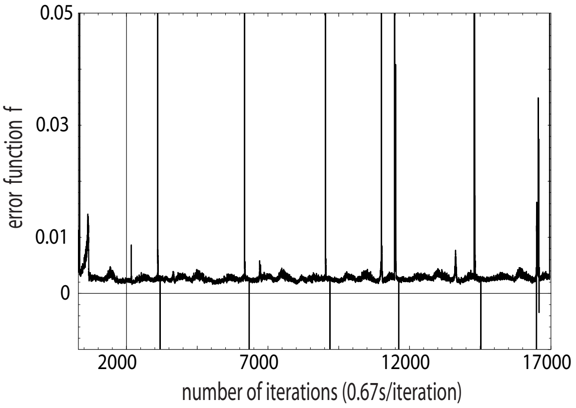

Figure 2.19: The errorfunction of the measurement shown in fig. 2.18. It is very close to zero except from some peaks, resulting from malfunctions of the shutters.

the threshold was not reached at all. This is due to bad alignment of the two input polarization states, i.e. the angle between the two complementary polarizations is not exactly 45^o. In this case the maintenance breaks with a mean value of the errorfunction of 0.0419 ± 0.0129. Readjusting of the reference polarizations solved this problem. Thus the quality of the maintenance of polarization is mainly dominated by the proper alignment of the reference polarizations. If the control converges, it takes on average 16.9 ± 1.1 iterations to stop with a mean value of the errorfunction of 0.0037 ± 0.0001. We see, that the overlap with the initial states on average is better than the threshold of 99.80%. If the input polarizations are aligned properly, the stop condition is always reached We see that the polarization control is a reliable tool to control the polarization passing through long optical fibers. Its quality depends on the alignment of the reference polarizations. This enables us to extend experiments to long distances that are using the polarization degree of freedom of light to encode information, without having significant losses.

2.5.3 Ideas for improvement

The speed of the polarization control is mainly limited by the speed of the mechanical shutters, ensuring that only one input polarization is sent through the fiber. Due to the high CPU load they cannot be driven at full speed, because this would increase the number of maloperations, i.e. switching the shutters at the wrong time. At the moment, one iteration takes 0.67 s, without driving the shutters at their limits. Implementing the control algorithm electronically or lowering the CPU load could thus increase the speed by about a factor 5.

The next step would be to replace the shutters by an AOM.This would decrease the time needed for one iteration. The new limit then is given by the photodiodes, whose rise time

is a factor 10^3 longer than the one of an AOM. With a rise time of 72 μs and 10 measurements per iteration the maximum frequency will be 1.39kHz. These ideas have not been realized as at the present setup, since the current speed is sufficient.
Although the accuracy of the maintained output polarizations is very high it is limited by the used voltage output, with a maximum resolution of 2.5 mV. These errors could be reduced by a factor of at least 4 by using a voltage output card with a better resolution or an output range matched to $0 - 5$ V.

2.6 Conclusion

In this chapter we have presented all tools necessary to provide an active control of the polarization of light running through an optical fiber. Furthermore, a compensation algorithm was implemented that allows to actively compensate the polarization errors introduced by the birefringence of the optical fiber. The two reference polarizations are adjusted with a mean accuracy of 99.84%, the polarization tomography measures the polarization with an error less than 0.13% and the polarization controller can manipulate the polarization with an minimal resolution of the angle between 0.86^o and 1.15^o in Stokes space. The results of the polarization control working with these components were presented, showing that it is a reliable, sufficiently fast and precise instrument to maintain the polarization of light through fibers, when the dephasing elements like temperature-drifts are on the same timescale as the control frequency. Within an average of 22 iteration steps, the overlap between the reference polarizaions and the measured ones behind the fiber is better than 99.80%. This ensures that experiments where spatial distances of several hundred meters are needed can be performed, without having additional noise due to the fluctuations of the polarization.

Chapter 3

Distribution of atom-photon entanglement over long distances

A key elemtent in many applications of quantum information, communication and computation is entanglement [25]. By entangling light and matter it is possible to create an interface between material based quantum memories and photonic communication channels. The ideal carrier of quantum information is light, as already mentioned in the last chapter. Quantum memories are provided by ions, atomic clouds or single atoms due to their long coherence times up to several microseconds and under special conditions even up to seconds. So far experiments entangling photons with ions or single atoms over distances of some meters have already successfully been performed [16, 17]. To reach the long term goal of a loophole free test of Bell's inequality, it is necessary to create entanglement between two quantum memories, separated by several hundred meters due to the finite measurement time of approximately 1 μs. One step in this direction is to separate both particles of an entangled atom-photon pair up to this distance. This can be achieved by separating the photon detection from the trapped atom by a 300 m long optical fiber. In the following chapter the setup to create an entangled atom-photon pair will be described, the extension to large distances by using a 300 m single mode optical fiber to connect the point of creation and the detection of the photon is explained and the results are presented.

3.1 Quantum mechanical two level systems

Quantum mechanical two level systems are key elements in applications of quantum information, communication and computation, as they provide the classical analog to the classical bit, the so-called qubit.

As already mentioned in the previous chapter a quantum mechanical two level system is fully described by:

$$|\Psi\rangle = cos\frac{\theta}{2}\,|\uparrow\rangle + e^{i\phi}sin\frac{\theta}{2}\,|\downarrow\rangle \tag{3.1}$$

where $|\Psi\rangle$ can be represented as a point on the Bloch sphere. As the most famous two level system we will refer to spin-$\frac{1}{2}$ particles with the two basis states $|\uparrow\rangle$ and $|\downarrow\rangle$.

3.1.1 Measurement

The measurement of a quantum system is described by a projection onto the eigenstates of a Hermitian operator $\hat{A}$. This operator is called observable and the possible outcomes of the measurement are given by the eigenvalues of $\hat{A}$. The expectation value of a measurement of $\hat{A}$ on a system $|\Psi\rangle$ is $\left\langle \hat{A} \right\rangle = \langle\Psi|\,\hat{A}\,|\Psi\rangle$. A complete set of complementary operators for spin-$\frac{1}{2}$ systems and also general two level systems are the so-called Pauli-matrices

$$\sigma_x = \begin{pmatrix} 0 & 1 \\ 1 & 0 \end{pmatrix}, \qquad \sigma_y = \begin{pmatrix} 0 & \imath \\ -\imath & 0 \end{pmatrix}, \qquad \sigma_z = \begin{pmatrix} 1 & 0 \\ 0 & -1 \end{pmatrix} \tag{3.2}$$

with eigenvalues ±1 and the corresponding eigenstates

$$|\uparrow\rangle_x = \frac{1}{\sqrt{2}}\left(|\downarrow\rangle_z + |\uparrow\rangle_z\right) \tag{3.3}$$

$$|\downarrow\rangle_x = \frac{1}{\sqrt{2}}\left(|\downarrow\rangle_z - |\uparrow\rangle_z\right) \tag{3.4}$$

$$|\uparrow\rangle_y = \frac{1}{\sqrt{2}}\left(|\downarrow\rangle_z + \imath\,|\uparrow\rangle_z\right) \tag{3.5}$$

$$|\downarrow\rangle_y = \frac{1}{\sqrt{2}}\left(\imath\,|\downarrow\rangle_z + |\uparrow\rangle_z\right) \tag{3.6}$$

where $|\uparrow\rangle_z$ and $|\downarrow\rangle_z$ are the eigenstates of σ_z. One sees that the three Pauli matrices project a general two level state states onto one of the three axes of the Bloch sphere each (fig. 2.2).

3.2 Entanglement

If we consider quantum states with n particles, a class of states exists, which cannot be written as a product state of the single particle states $|\Psi\rangle_1, |\Psi\rangle_2, ..., |\Psi\rangle_n$:

$$|\Psi\rangle \neq |\Psi\rangle_1 \otimes |\Psi\rangle_2 \otimes ... \otimes |\Psi\rangle_n\,. \tag{3.7}$$

This class of states is called entangled, in contrast to separable states, where above equation yields a " = ". The interesting feature of entanglement is, that the Hilbert space describing the particle is not separable into subspaces, what leads to strong correlations between the measurement performed on one particle and the state describing the remaining particles, although this measurement gives random outcome. That means in this case we can not consider the states $|\Psi\rangle_1, |\Psi\rangle_2, ..., |\Psi\rangle_n$ alone. Most clearly one can see this for a system consisting of two spin-$\frac{1}{2}$ particles. A basis consisting of separable states is defined by:

$$|\uparrow\rangle_z |\uparrow\rangle_z\,,\ |\downarrow\rangle_z |\downarrow\rangle_z\,,\ |\uparrow\rangle_z |\downarrow\rangle_z\,,\ |\downarrow\rangle_z |\uparrow\rangle_z \tag{3.8}$$

In contrast we can also provide a basis consisting of four maximally entangled states, the so-called Bell states:

$$\left|\Psi^-\right\rangle = \sqrt{\frac{1}{2}}\left(|\uparrow\rangle_z |\downarrow\rangle_z - |\downarrow\rangle_z |\uparrow\rangle_z\right) \tag{3.9}$$

$$\left|\Psi^+\right\rangle = \sqrt{\frac{1}{2}}\left(|\uparrow\rangle_z |\downarrow\rangle_z + |\downarrow\rangle_z |\uparrow\rangle_z\right) \tag{3.10}$$

$$\left|\Phi^-\right\rangle = \sqrt{\frac{1}{2}}\left(|\uparrow\rangle_z |\uparrow\rangle_z - |\downarrow\rangle_z |\downarrow\rangle_z\right) \tag{3.11}$$

$$\left|\Phi^+\right\rangle = \sqrt{\frac{1}{2}}\left(|\uparrow\rangle_z |\uparrow\rangle_z + |\downarrow\rangle_z |\downarrow\rangle_z\right) \tag{3.12}$$

$|\Psi^-\rangle$ is the antisymmetric singlet state and the other three are symmetric triplet states. This means that exchanging the particles gives a global minus-sign on the anti-symmetric states or in the symmetric case the state remains the same.

One further feature is, that entanglement does not depend on the choice of the measurement basis. For example we can rewrite $|\Psi^+\rangle$ in terms of eigenvectors of σ_x and σ_y:

$$\left|\Psi^+\right\rangle = \sqrt{\frac{1}{2}}\left(|\downarrow\rangle_x |\downarrow\rangle_x + |\uparrow\rangle_x |\uparrow\rangle_x\right) \tag{3.13}$$

$$= \sqrt{\frac{1}{2}}\left(|\downarrow\rangle_y |\downarrow\rangle_y - |\uparrow\rangle_y |\uparrow\rangle_y\right). \tag{3.14}$$

The most interesting feature of two maximally entangled two level systems is the fact, that by performing a measurement on one of the particle, although having completely random outcomes, the state of the second particle is strictly correlated. This strong correlation between the two particles is a purely quantum mechanical feature and raised many questions about the physical description of reality resulting in the EPR paradox and Bell's inequality.

3.2.1 The EPR paradox and Bell's inequality

The fact that the measurement on one particle could completely determine the state of the second particle lead to controversial discussions [26, 27]. In 1935 Einstein, Podolsky and Rosen (EPR) published an article "*Can Quantum-Mechanical Description of Physical Reality Be Considered Complete?*" [26] in which they stated that quantum mechanics can not be a complete theory in describing the physical reality. They gave three basic conditions, that every physical theory has to fulfill:

1. Completeness: *"Every element of the physical reality must have a counterpart in the physical theory"*
2. Realism: *"If, without in any way disturbing a system, we can predict with certainty (i.e. with probability equals to unity) the value of a physical quantity, then there exists an element of physical reality corresponding to this physical quantity"*
3. Locality: Physical systems can be separated such, that their interaction can be neglected (e.g. by sufficient large distances).

Then, they proposed a gedanken experiment using two particles being entangled in momentum and position degree of freedom and separated far enough from each other to provide locality, i.e. the particles are separated far enough to exclude interactions of the particles, when the measurements are performed. By measuring the position of particle 1, the position of particle 2 can be determined with certainty. They inferred that thus the position is an element of physical reality. Suppose we now measure the momentum of particle 1, being an element of physical reality, too. By this particle 2 has a well defined position and a well defined momentum. But this violates the Heisenberg uncertainty principle. The three authors concluded that, by this the quantum theory can not be complete because it violates above stated assumptions.

The conclusion of the EPR-gedanken experiment inspired the construction of local hidden variable theories (LHV). These theories explain the correlations in the measurements by introducing unknown, so called hidden variables, which are not experimentally accessible. By these variables the outcome of a measurement is absolutely defined. Thus, the LHV theories claim, that nature is deterministic. The results of the measurement only seem to have a probabilistic behavior due to the lack of knowledge about the hidden variables. Bohr replied [27] that the proposed gedanken experiment contradicted quantum mechanics as the measurement processes Einstein et al. had considered could not be performed simultaneously, because two different (complementary) measurement setups were needed to gather information about the values of the two observables. He concludes that it is not justified to consider these complementary degrees of freedom as parts of a simultaneous reality, thus he objects to their conclusion of quantum mechanics being incomplete. A summary of these results was given by Schrödinger in the same year [28]. In these articles Schrödinger also introduced the term "*Verschränkung*" ("entanglement").

The original EPR-paradox is difficult to understand as it deals with continuous variables, namely space and momentum, making the mathematics complicated. Bohm transferred

the EPR-paradox onto the meanwhile best known version; the entanglement is described between two spin-$\frac{1}{2}$ particles, being in a singlet state, resulting from a decay of a spin-0 particle, simplifying the mathematical description.
The existence of entangled systems, showing the behavior that was proposed in the EPR-paradox, formulated by Bohm was shown in 1950 by Wu and Shaknov by creating two entangled γ-quanta from the annihilation of a positron-electron pair [29]. But until 1964 there was no way to experimentally disprove either LHV-theories or the completeness of quantum mechanics. In this year, Bell developed an inequality [30],that must hold for any of these theories to describe local reality. Quantum mechanics, if being complete, indeed predicts a violation of this inequality being possible. There are different approaches to get an equality accessible by experiments [4, 5, 6]. The most famous one is a version of Bell's inequality generalized by CHSH [4] and later on by Bell again [3]. The final inequality reads:

$$S(\mathbf{a{,}a'{,}b{,}b'}) = |E(\mathbf{a{,}b}) - E(\mathbf{a{,}b'})| + |E(\mathbf{a'{,}b}) + E(\mathbf{a'{,}b'})| \leq 2 \tag{3.15}$$

$E(\mathbf{a{,}b})$ represents the expectation value of a measurement of particle 1 with the analyzer setting **a** and of particle 2 with the analyzer setting **b**. Quantum mechanics predicts a maximal value of $S(\mathbf{a{,}a'{,}b{,}b'}) = 2\sqrt{2}$ what contradicts inequality 3.15. The violation of the above inequality has been shown in many experiments, giving strong indications or the completeness of quantum mechanics [8, 9, 11, 12, 13]. But up to now additional assumptions have to be made, leading to the following two loopholes:

1. Detection loophole: Due to limited detection efficiencies, not all particles are detected. Although the detected events violate Bell's inequality, there is a certain probability that the whole ensemble (consisting of detected and not detected particles) does not. One has to assume the detected particles being a representative part of the ensemble. This assumption is called "fair sampling".

2. Locality loophole: In principle the measurement apparatuses to determine the properties of the two particles respectively, can interact with the speed of light. To close this loophole they have to be separated in a way that no relativistic transport of information about the other analyzer is possible at the time of the measurement. This can be done by spatially separating the analysis of both particles with respect to the needed measurement time.

The detection loophole was closed by analyzing entangled ions [13], the locality loophole was closed by measurements performed on entangled photons [12]. But so far no experiment was able to close both loopholes at the same time.
Except from this fundamental point of view to prove entanglement, it has also important applications in quantum information and quantum communication as we will see in section 4.1 of the next chapter.

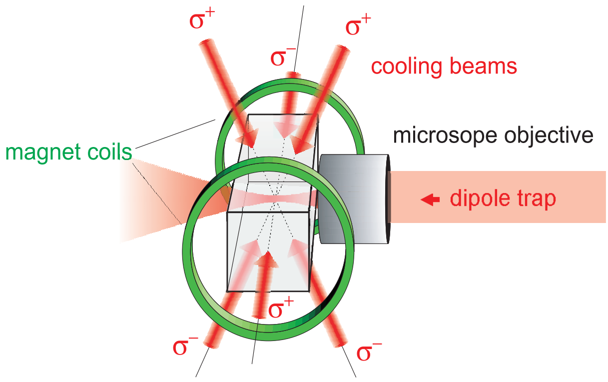

Figure 3.1: Schematic setup of the MOT and the dipole trap. The lasercooling is provided by three counterpropagating beam pairs. Together with the coils in anti-Helmholtz configuration the magneto-optical trap is realized, providing a dissipative force towards the center of the dipole trap. The two beam pairs in the horizontal plane are not perpendicular, but include an angle of 34^o, due to restricted space around the glass cell.

3.3 Atom-photon-entanglement

3.3.1 The existing experiment

So far our group has successfully entangled a ^{87}Rb -atom with a photon generated by spontaneous decay [17]. In this section we will describe the actual setup and present the scheme how the entanglement is obtained. The current setup can be divided into four main parts: The trapping of a single atom, the generation of entanglement by spontaneous decay, the readout of the internal atomic state and the measuring of the photonic state.

These different steps of the performed experiments are presented in the next sections.

3.3.2 Trapping of a single ^{87}Rb -atom

We want to generate entanglement via spontaneous decay. Therefore a Λ decay scheme with two degenerated energy levels is needed. The question which kind of atom is to be used to match the above condition gives raise to the question in which way a single atom can be trapped. We do not want to use ions, which in principle are as usable as atoms, but mostly have transitions in the ultraviolet, what increases the absorption loss when the photons are transported over long distances. To prevent these losses it is preferable to work with atoms with emission lines in the visible or near-infrared region. We are working with neutral ^{87}Rb , having weak coupling to the environment. The internal structure is optimal for our purposes, as its decay scheme is an almost perfect Λ decay and the first exited states, the D_1- and the D_2-line are addressable by commercially available laser diodes (795 nm and 780 nm respectively).

But still, the choice of the atomic species does not show which trap can be used. In principle Magneto-optical traps (MOTs) are not useful, as they affect the internal states using dissipative forces, namely radiation pressure to trap the atom, what makes the needed internal state readout impossible. Since the entanglement should result from spontaneous decay, the trap may also not affect the Zeeman sub-levels, otherwise making them distinguishable and leading to decoherence, what destroys the entanglement. This excludes magnetic traps. An alternative is the use of an optical dipole trap, relying on the interaction between the induced dipole-moment of the atom and the electric field of light. Using a far red-detuned, strongly focused laser, this interaction creates a conservative trapping potential, that is independent of the Zeeman and hyperfine state, if the light is linearly polarized [31]. Being focused tightly enough, a blockde effect prevents more than one atom from being trapped at the same time.

experimental frame

To make a trapping possible and to gain reasonable lifetimes of a single ^{87}Rb -atom in the dipole trap, the experiments are performed in ultra high vacuum at a background pressure of 10^{-10} mbar. The vacuum is maintained by an ion getter pump (Varian Star, 24 l/s). The source for the ^{87}Rb -atoms is a Rubidium dispenser operating slightly above threshold (2.5 A). The experiment takes place in a commercial, uncoated spectroscopy glass cell, connected with the vacuum system by an indium gasket.

Magneto-optical trap

A dipole trap has a very low depth and the trapping potential is conservative. To make trapping in it possible a friction force is needed. This force is provided by a MOT, consisting of the light of the cooling and the repump laser and a magnetic quadrupole field. The two lasers are locked to atomic transitions via Doppler-free saturation spectroscopy and provide a long term frequency stability better than 2 MHz and a spectral line width of less than 700 kHz [14]. The frequency and power fine tuning is realized by the use of acousto optical modulators, and finally the power of the light of both laser diodes is monitored by a photo diode, providing the possibility to stabilize the power of both fields. The light of the two diodes is combined, guided to the experiment and split up into three pairs of counterpropagating orthogonally circularly polarized beams intersecting at the position of the dipole trap (see fig. 3.1). The cooling mechanism itself is realized with the cooling laser operating red detuned by 5-6 linewidths (24-30 MHz) to the transition $5^2S_{1/2}, F = 2$ to $5^2P_{3/2}, F' = 3$. Due to the detuning of the cooling laser the transition is not closed. Offresonant excitation to $F' = 2$ occurs. From this energy level, the atom decays into the non-resonant $F = 1$ state. To pump the atom back into the cooling cycle and thus forming a closed transition the repump laser is needed. It is resonant with $5^2S_{1/2}, F = 1$ to

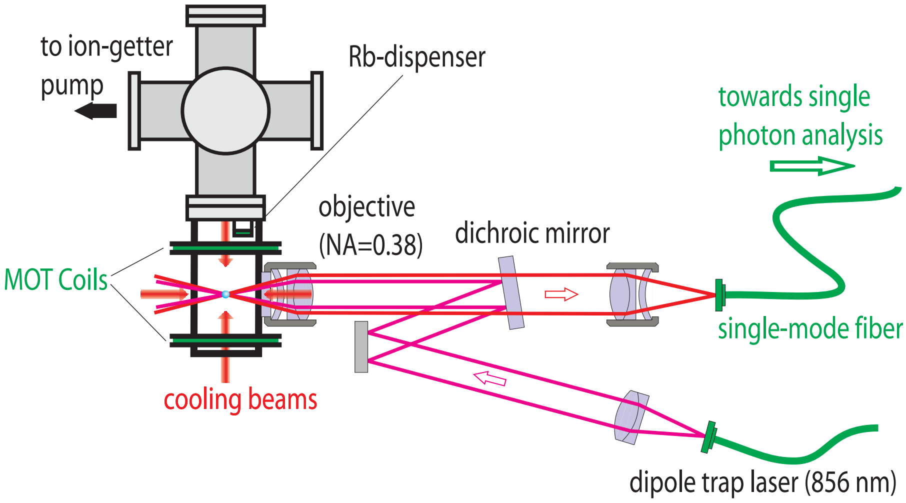

Figure 3.2: Scheme of the dipole trap an the collection optics from above. The dipole trap is realized by a single mode laser diode, focused into the center of the MOT. The light from the spontaneous decay of the atom is collected by a confocal arrangement with the dipole trap. The light is coupled into a single mode optical fiber for spatial filtering.

$5^2P_{3/2}, F' = 2$. Thus, in the region of intersection sub-Doppler cooling mechanisms should occur cooling down the atoms to a final temperature below the Doppler limit of ^{87}Rb of 146 μK [32].
The MOT is created by the three counterpropagating beam pairs and two coils in anti-Helmholtz configuration, with the center of their quadrupole field in the overlap section of the beams. The coils are operated at a maximum current of 2 A and can generate a magnetic field gradient of up to $\partial B/dz = 11$ G/cm. The waists of the cooling beams have 1mm, allowing to store about 3×10^4 cold atoms. Using the MOT, the loading rate of the dipole trap is more than 1 atom per second.

Dipole trap

The dipole trap is realized with light from a single mode laser diode with a wavelength of 856nm what is far red-detuned from the first exited states of ^{87}Rb (780 nm and 795 nm). The peak power of the diode is 200 mW. A Gaussian beam profile is ensured by spatially filtering the light with a single mode optical fiber. In order to trap only one atom, we use a blockade effect occurring for dipole traps with a beam waist below 4 μm limiting the maximum atom number in the trap to one, if the loading rate is not too high [33, 34, 15]. A commercial microscope objective (NA 0.38) is used to focus the trap light to a beam waist of $\omega_0 = 3.5 \pm 0.2$ μm (see fig. 3.2). The intensity of the light is stabilized by monitoring it via a phot diode and using an AOM to adjust the power. We achieve laser powers of 30

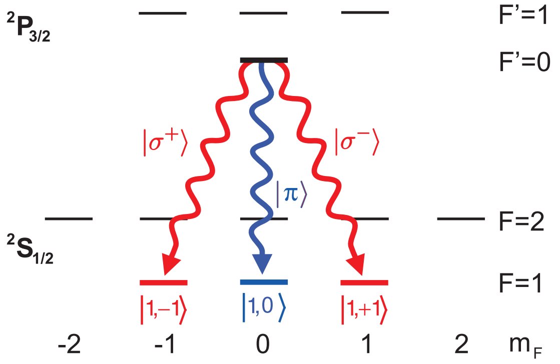

Figure 3.3: Spontaneous decay from the first exited state into the three possible ground states $|1,\pm1\rangle$ and $|1,0\rangle$. The decay into the latter state is colored blue to symbolize, that this transition is not observed with the detection optics.

mW at the trap region, what corresponds to a trap depth of approximately 860 μK, with a longitudinal (transverse) trap frequency of 1.4 kHz (26 kHz) and a photon scattering rate from the trapping beam of 20 s^{-1}.
By spectrally analyzing the fluorescence light of the atom with a scanning Fabry-Perot interferometer, the mean temperature of the trapped atom was measured, being

$$T_{atom} = 105 \pm 25^{+15}_{-17} \mu\mathrm{K} \ , \tag{3.16}$$

resulting from the mean kinetic energy of the atom in the trap [14].

3.3.3 Generation of entanglement by spontaneous decay

The entangled atom-photon state

The entangled atom-photon pair is, as already mentioned, created by spontaneous decay. To create a maximally entangled atom-photon state, the Λ-type decay of a atomic transition is used. We consider the decay of ^{87}Rb from the first exited state $5^2P_{3/2}, F' = 0$ into $5^2S_{1/2}, F = 1$. After the decay, the atom is in the ground state with total angular momentum $F = 1$. The conservation of angular momentum leads to nonclassical correlations of the polarization of the emitted photon and the magnetic quantum number $m_F = \pm1, 0$ of the atom. The final state reads:

$$\begin{aligned} |\Psi\rangle \ &= \ \sqrt{\frac{1}{8\pi}} \left[\sqrt{\frac{1}{2}(1+\cos^2\theta)} \left(\left|\sigma^+\right\rangle |1,-1\rangle + \left|\sigma^-\right\rangle |1,+1\rangle \right) + \sin\theta \, |\pi\rangle \, |0,0\rangle \right] \\ & \quad \otimes \sum_{\theta,\omega} g_\omega \, |\theta,\omega\rangle \ , \end{aligned} \tag{3.17}$$

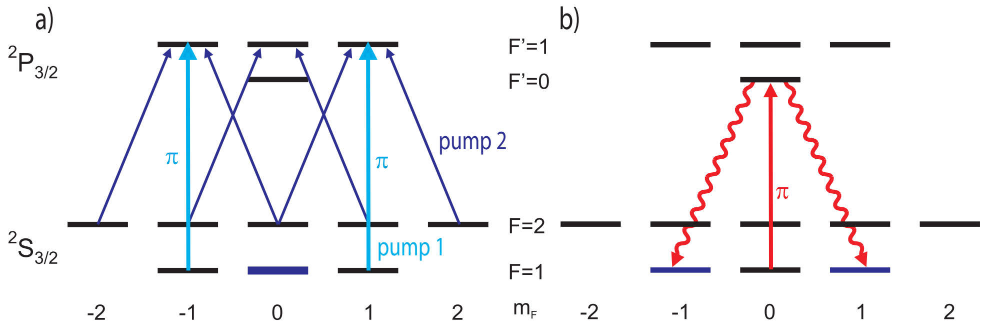

Figure 3.4: Transition scheme to prepare the ^{87}Rb atom in the state from where the entangled atom-photon pair is created. a) Optical pumping to prepare the atomic population in $F = 1, m_F = 0$, done by two pumping beams resonant to the $F = 1 \rightarrow F' = 1$ and $F = 0 \rightarrow F' = 1$ transitions. b) The atom is transferred into its first exited state with a resonant π-pulse.

where the prefactors are given by the emission probability into the different modes, defined by the characteristics of dipole radiation [35]. The atomic ground state is labeled by $|F, m_F\rangle$, the photonic polarization state is given by $|\sigma^\pm\rangle$ and $|\pi\rangle$, θ is the angle relative to the quantization axis and $\sum_{\theta,\omega} g_\omega |\theta, \omega\rangle$ describes the spatial and frequency modes of the emitted photon.

Due to the alignment of detection optics along the quantization axis and the zero overlap of the $|\pi\rangle$-polarized photon-state with the eigenmode of the single mode fiber, π-decays can not observed [14]. By not being able to distinguish the decay-channels spectrally, the final atom-photon state entering the detection optics becomes a maximally entangled Bell state. The entangled atom-photon state reads:

$$|\Psi\rangle = \sqrt{\frac{1}{2}} \left(\left|\sigma^+\right\rangle |1, -1\rangle + \left|\sigma^-\right\rangle |1, +1\rangle \right) \tag{3.18}$$

preparation of the atom

Being located in the dipole trap a ^{87}Rb -atom is not initially in the $\left|5^2P_{3/2}, F' = 0\right\rangle$-state as the MOT mixes the atomic states due to its different polarized lightfields. The preparation is realized in two steps. First, optical pumping transfers the atom into the Zeeman ground state $F = 1, m_F = 0$. For this purpose two light fields are used, resonant to the transitions $F = 1 \rightarrow F' = 1$ and $F = 2 \rightarrow F' = 1$, respectively. To prevent the atom from populating a dark state of the $F = 2$ level, the cooling light is applied simultaneously, redistributing the population in the $F = 2$ ground level.

Having finished the optical pumping, the atomic population is transferred to the exited state $F' = 0$ via an optical π-pulse resonant to this transition. The length of the pulse

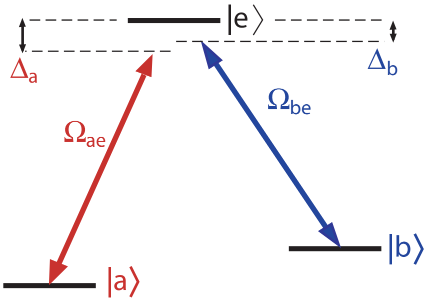

Figure 3.5: Schematic three level system with two ground states and two lightfields Ω_{ae} and Ω_{be}, being almost resonant to the transitions $|a\rangle \rightarrow |e\rangle$ and $|b\rangle \rightarrow |e\rangle$, respectively.

is chosen to be approximately 20 ns, being the lifetime of the exited state to prevent the population of the $F' = 1$ and the $F' = 2$ states. The pumping process yields a preparation efficiency of approximately 50% [14]. Thereafteremissionn of a photon occurs, which is collected by the same microscope objective to focus the light of the dipole trap.

3.3.4 Readout of internal atomic states

The verification of entanglement between the internal atomic states and the polarization of the photon requires a precise and effective readout of the atomic state. This is done in three steps.

First, we use a stimulated adiabatic Raman passage (STIRAP) to adiabatically transfer one well defined superposition of the Zeeman sublevels of the $F = 1$ hyperfine groundlevels to the $F = 2$ hyperfine level, whereas the orthogonal superposition remains in $F = 1$. Second, we use a projection pulse resonant to the $F = 2 \rightarrow F' = 3$ transition, what leads to a loss of the atom out of the trap.Third, a fluorescence detection is performed to check if the atom was removed from the trap or not. The result of the detection gives us the information, which state the atom was projected into from theprecedingg steps.

STIRAP and state-selective transitions

Coherent dark states Let us consider an atomic system, consisting out of two ground states $|a\rangle, |b\rangle$ and one exited state $|e\rangle$, with the transition frequencies ω_{ae} and ω_{be}.

Considering the case where two nearly resonant light fields with Rabi-frequencies Ω_{ae} (almost resonant to the transition $|a\rangle \rightarrow |e\rangle$) and Ω_{be} (almost resonant to the transition $|b\rangle \rightarrow |e\rangle$) are incident on the atom, one can show that in the case where the detuning of the light fields is equal ($\Delta_a = \Delta_b$, see fig. 3.5) a stationary eigenstate of the corresponding Hamiltonian occurs [14]. In the interaction picture it is given by:

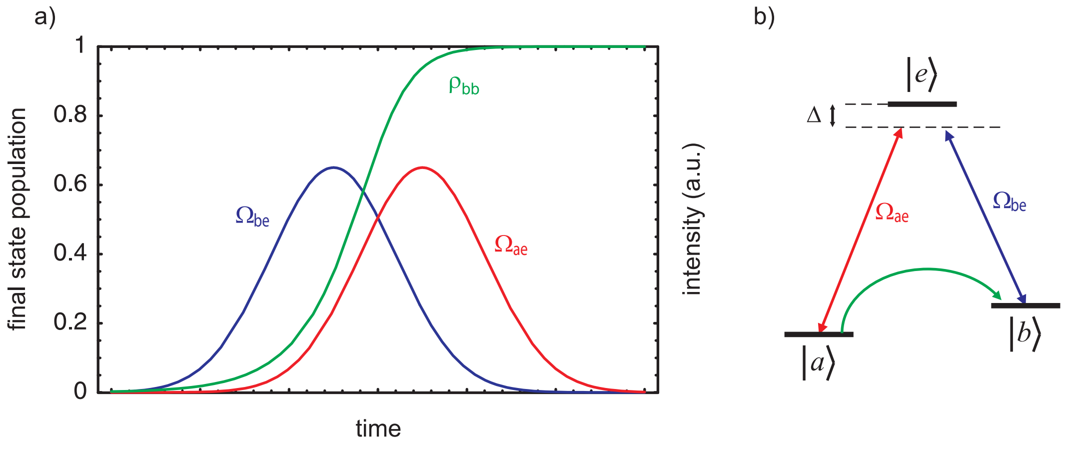

Figure 3.6: a) Typical pulse sequence in a STIRAP process in order to transfer all population from the state $|a\rangle$ to the final state $|b\rangle$, according to the level scheme, presented in b). The population transfer occurs, when both pulses overlap, represented by ρ_{bb}.

$$|\Psi\rangle = \cos\theta\,|a\rangle - e^{-i\phi}\sin\theta\,|b\rangle\ , \tag{3.19}$$

where θ is the mixing angle defined by:

$$\tan\theta = \frac{\Omega_{ae}}{\Omega_{be}}\ . \tag{3.20}$$

and ϕ is the initial phase difference of the two light fields.

The state in eqn 3.19 is stable against spontaneous decay as no exited state contributes. No coupling to the the light fields Ω_{ae} and Ω_{be} can occur as $|\Psi_D(t)\rangle$ is stationary. It is a dark state with respect to the two light fields Ω_{ae} and Ω_{be}.

Stimulated Raman adiabatic passage (STIRAP) Using a STIRAP process, the complete population of one atomic state $|a\rangle$ can adiabatically be transferred into another state $|b\rangle$ [36]. For this purpose, first a light field, almost resonant to the transition from the final state $|b\rangle$ to one exited state $|e\rangle$ is incident to the atom, followed by a second pulse almost resonant to the transition from the initial state $|a\rangle$ to $|e\rangle$ (see fig. 3.6). By this procedure, an adiabatic transfer of the population in $|a\rangle$ to $|b\rangle$ can be obtained. This can be understood by making the mixing angle θ (eqn. 3.20) time dependent.

The dark state of these two light fields is then given according to eqn. 3.19 by

$$|\Psi(t)\rangle = \cos\theta(t)\,|a\rangle - e^{-i\phi}\sin\theta(t)\,|b\rangle\ , \tag{3.21}$$

The initial condition we consider is the case where the atom is in the state $|\Psi\rangle = |a\rangle$ and only the light field Ω_{be} is present ($\theta = 0$). When Ω_{ae} is increased while Ω_{be} is reduced

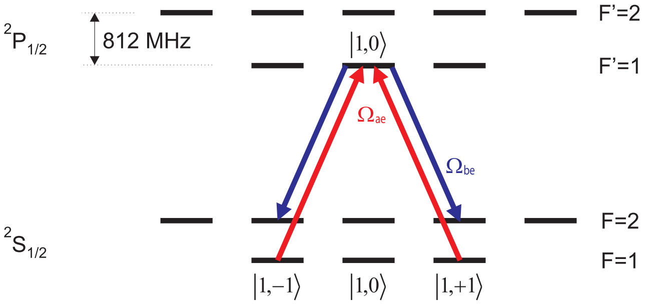

Figure 3.7: Tripod-STIRAP transition using the hyperfine level $5^2P_{1/2}, F' = 1, m_F = 0$ in ^{87}Rb . Both STIRAP-fields consist of σ^- and σ^+ components to achieve high detection accuracy.

at the same time until it is switched off, the mixing angle θ changes from 0 to $\pi/2$ until the final dark state $|\Psi\rangle = |b\rangle$ is reached. If the intensities of the light fields are changed adiabatically[1], the atom stays in the dark state the whole time. In this case, all population is transferred from the initial state $|a\rangle$ to the state $|b\rangle$ without populating the exited state $|e\rangle$. A typical pulse sequence of the two light fields and the corresponding population ρ_{bb} of the final state $|b\rangle$ are shown in fig. 3.6.

In our experiment, this STIRAP technique is used to analyze superposition states of the $5^2S_{1/2},\ F = 1$ hyperfine ground level of ^{87}Rb . In this case the initial state $|a\rangle$ (see eqn. 3.21) consists of a coherent superposition of $|1, \pm 1\rangle$ states, depending on the polarization of the incident light field Ω_{ae}. If the light is traveling along the quantization axis and the polarization vector is:

$$\mathbf{P} = \cos\alpha \cdot \sigma^- + e^{\imath\varphi} \sin\alpha \cdot \sigma^+ \tag{3.22}$$

the initial state $|a\rangle$ reads:

$$|a\rangle \quad = \quad \sin\alpha\ |1, -1\rangle - \cos\alpha\ e^{\imath\varphi}\,|1, +1\rangle \tag{3.23}$$

The population of this state is transferred to the $F = 2$ level via the STIRAP process using the intermediate level $5^2P_{1/2},\ F' = 1$. The state orthogonal to $|a\rangle$ is not affected by this process, because in analogy to sec. 3.3.4 *"Coherent dark states"* it is in a coherent dark state with respect to Ω_{ae}. It stays in $F = 1$. This tripod STIRAP technique enables us to make state selective transfers of well defined atomic superposition states, where in essence the polarization of the STIRAP light fields defines our measurement basis.

In our experiment this transfer is realized using two light fields, one resonant to the transition $F = 1 \rightarrow F' = 1$ with the polarization state $\mathbf{P}$ (according to eqn. 3.22) and

---

[1] Adiabacity is given as long as the time scale of the intensity changes of the two light fields are much bigger than the inverse of the effective Rabi frequency Ω_{eff} [14].

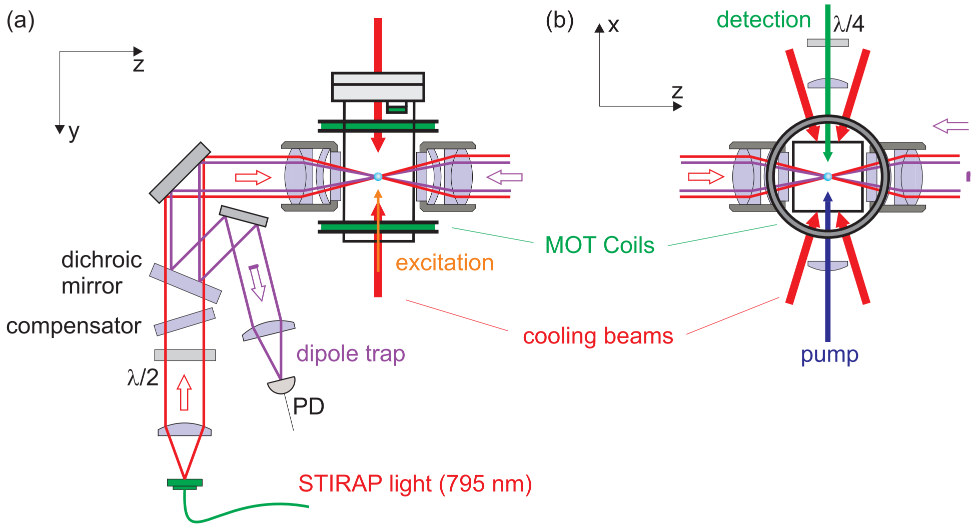

Figure 3.8: Experimental setup to cool down and trap one single ^{87}Rb atom, to prepare it into the $F' = 0$ state to create an entangled atom-photon pair via the pump beam and to make the state selective readout using the STIRAP process and the projection pulse. The STIRAP beams are focused to the position of the dipole trap, having a waist of approximately 8 μm. To separate light from the dipole trap and the STIRAP light, a dichroic mirror is used. a) is the top view, b) the side view.

a second field resonant to the $F = 2 \rightarrow F' = 1$ transition. The light is generated from two independently frequency stabilized laser diodes at a wavelength of 795 nm resonant to the D_1-line of ^{87}Rb . The shaping of the pulse sequence is realized by AOM's, allowing a minimum pulse width and transfer time down to approximately 20 ns.

Projection pulse and state detection

So far different superpositions of the Zeeman levels $m_F = \pm 1$ of the $F = 1$ state of a single ^{87}Rb atom can be selected and transferred into the $F = 2$ state. To distinguish between population in $F = 1$ and $F = 2$, we use a projection pulse, resonant to the $F = 2 \rightarrow F' = 3$ transition, with a typical puls length of 6 μs. If the atom is in the $F = 2$ state, it scatters photons and acquires an additional momentum for every scattering event. After approximately 50 scattering events, the total momentum gained from this scattering process leads to a loss of the atom from the dipole trap.

Now one has to distinguish two possibilities: Either the atom was not transferred to $F = 2$ by the STIRAP process and is still in the trap, or the atom has been transferred to the $F = 2$ state and has been removed from the trap.

To find out which of these two cases is true, the cooling beams of the MOT are switched

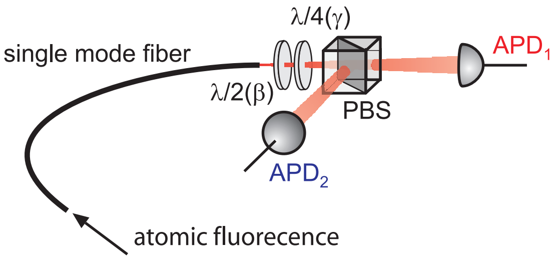

Figure 3.9: Setup to detect single photons. The measurement basis is changed by a half- and a quarter-wave plate.

on and the fluorescence is observed. If the measured fluorescence corresponds to the background rate of the detectors, the atom was removed from the trap. Otherwise, the atom still is in the trap, what means the atom was not affected by the STIRAP process.

In following discussions we shall call the state, that stays in the trap when the readout process takes place, the dark state $|\Psi_D\rangle$ of the STIRAP process, as it is not affected by the STIRAP light fields. The state that is removed by the projection pulse is called the bright state $|\Psi_B\rangle$ (in terms of the description of the STRAP process $|\Psi_B\rangle$ corresponds to $|a\rangle$). It is important not to mix up the dark states introduced in the previous section with $|\Psi_D\rangle$. They are used in another context and have a completely different meaning than $|\Psi_D\rangle$.

This state-selective readout, realized in our setup has a detection efficiency of $a_D \approx 93\%$ and $a_B \approx 97\%$ for the detection of the dark state and the bright state respectively, giving a mean accuracy of 95% [14].

3.3.5 Single photon detection

For the detection of the atomic fluorescence, as well as of the single photons of the entangled atom-photon pair, we use two actively quenched avalanche photo diodes (APDs) with a dark count rate of approximately 50 counts/s. To suppress unwanted stray light of any kind interference filters are used with a 1 nm transmission region (FWHM) around the center wavelength of 780 nm in front of the detectors. The detection events are registered with a time-stamp card allowing a time resolution of 2 ns. The probability to detect a photon from a spontaneous decay is 0.05%, resulting out of non detectable π-decays, the finite numerical aperture of the microscope objective and absorption in the fiber. Therefore the pump-excitation cyclus is repeated approximately 200 times until the photon is detected.

The single photon detection is done in one polarization basis, using two APDs and a partially polarizing beamsplitter (PBS) (see fig. 3.9). The measurement basis can be changed

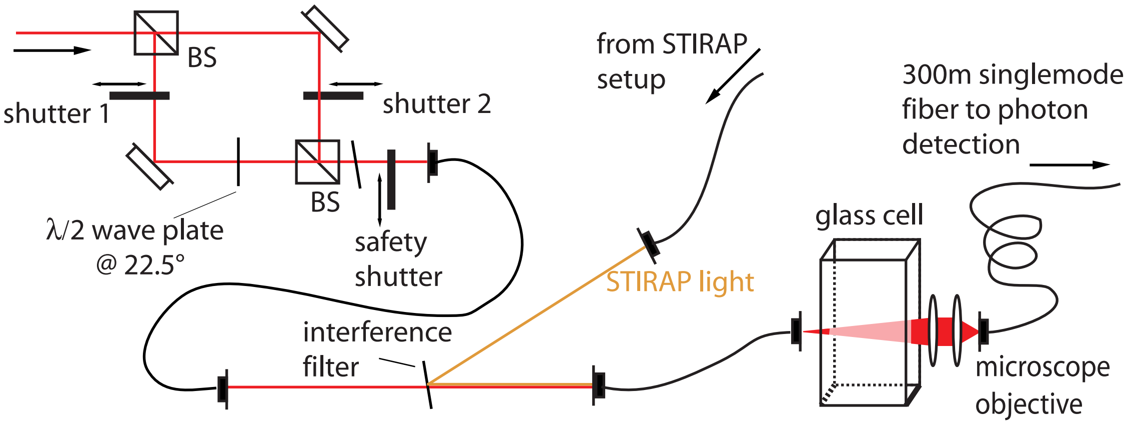

Figure 3.10: Schematic setup to create two complementary polarizations. The light is coupled into a fiber together with the STIRAP light. An interference filter transmitting at 780 nm is used as dichroic mirror. The polarization is adjusted to be $|V\rangle$ and $|+\rangle$,respectively, in front of the glass cell.

by a $\lambda/2$- and a $\lambda/4$-wave plate in front of the PBS. The PBS has a transmission efficiency of $T_H = 99,80\%$ and $T_V = 0.62\%$ for horizontally and vertically polarized light respectively. This also defines the detection accuracy for these two polarizations ($1-T_V$ for $|V\rangle$), i.e. the probability of detecting a horizontally (vertically) polarized photon in the detector "APD_1" ("APD_2"), see fig. 3.9. The mean detection accuracy is $a_{photon} = 99.56\%$, neglecting the darkcounts of the APDs.

3.4 Extension to long distances

The entanglement of a ^{87}Rb atom with a photon has been verified so far over an optical fiber link of 5 m [14, 15]. As described in the previous chapter, using 300 m optical fiber connecting laboratories in different buildings, makes the stabilization of the photonic polarization on its way through the fiber necessary. Therefore all elements, described in the previous chapter are integrated into the current setup together with the control algorithm.

3.4.1 Integration of the polarization control setup

Polarization controller

To get light, collected by the microscope objective, into the detection fiber with reasonable efficiency (at the moment, the short detection fiber has a coupling efficiency of around 20%) is very difficult. To avoid this incoupling procedure at the microscope objec-

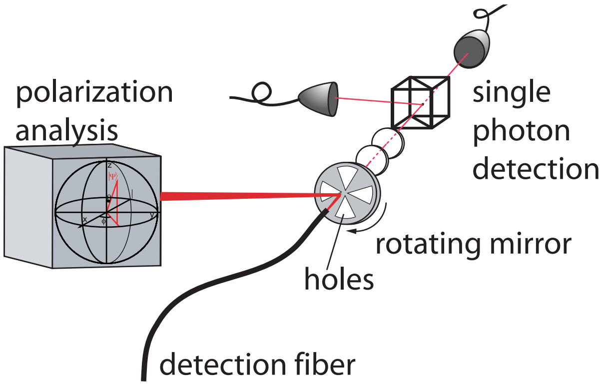

Figure 3.11: Scheme of the setup to include the polarization measurement. While the polarization is readjusted, the mirror deflects the light to the polarization measurement and makes sure that no light comes to the APDs to prevent them from damage.

tive, the 300 m fiber was connected to the short detection fiber. The coupling efficiency is 79.7%. The polarization controller was integrated into the setup by coupling the light out of the 300 m detection fiber and immediately into the fiber of the controller, which is necessary due to different core sizes (controller fiber: 4.6 μm; detection fiber: 4.8 μm). There we achieve a coupling efficiency of 82%. Afterwards, the light is guided through the controller to the single photon detection.

Generation of two complementary polarizations

The generation of two reference polarizations was integrated into the setup, by using light from the repump-master laser, creating the two polarizations according to Sec. 2.3.2, and coupling the light into the fiber which also guides the STIRAP laser to the glass cell (see fig. 3.10). This is done by using a 783 nm interference filter with 5nm transmission region (FWHM) as dichroic mirror. The polarizations were adjusted to be $|V\rangle$ and $|+\rangle$ directly in front of the glass cell, which is the point where all polarizations are defined. The starting power of the light is 8 mW at the beginning. It reduces due to coupling losses into the fiber, losses when joining the two beams, and losses at the interference filter, so we end up with approximately 200 μW for each of the beams in front of the glass cell.

Polarization analysis

The polarization analysis of the laser pulses providing the reference polarizations, is located at the end of the detection fiber. To separate it from the single photon measurement setup, a turnable mirror, built of a stepmotor and a silver-coated mirror is used. When the entanglement measurement is stopped to readjust the polarization, the mirror is flipped before switching on the alignment light, deflecting the beam to the polarization measurement setup and blocking all light to the APDs at the same time (fig. 3.11). The mirror maintains the polarization except transforming $|+\rangle$ to $|-\rangle$, what has to be considered when adjusting the measurement by exchanging the role of the measured transmitted and the reflected intensity at the polarizing beamsplitter in the $+/-$-analysis in the subsequent calculation.

Protection of single photon measurement

The APDs are extremely sensitive to high photon fluorescence. If, for example strong laser light from the polarization control hits the APDs they will be destroyed. To prevent this, light from the reference beams must be prevented from passing the fiber when the mirror does not block the single photon measurement. To ensure that no light passes before this is done, an additional safety shutter is placed before the test light is coupled into the fiber (see fig. 3.10). The safety shutter is initially closed. It can only be opened when the rotating mirror is in the position to allow the polarization tomography. This is realized by an interlock using a button that connects the shutter with the power supply. The button has to be pressed to close the connection, i.e. the shutter can only be opened, when the button is pressed. The button is placed in a way, that the rotating mirror presses it, if the mirror is in the position that blocks the APDs and allows to measure the polarization. The second safety feature is an electronic shut-down automatic for the APDs, shutting off the power supply when the countrate exceeds a maximum of around 3×10^5 counts/s.

Control scheme

The use of a longer detection fiber requires some changes in the measurement process. As light needs 1.5 μs to pass the 300 m long optical fiber (the refraction index of optical fibers is approximately $n = 1.5$), the detection window of the single photon has to be delayed about this time and additionally 0.5 μs, due to electronic delays resulting from longer cables, resulting from the fact that the single photon detection is further away from the processing unit than before. The measuring scheme has also to consider the time the polarization control needs to eliminate the birefringence of the fiber. This is done by giving the polarization control a time window of approximately 1 min (100 iterations) before analysis of the entangled atom-photon state starts.

Stability between measurements

The timescale of the drifts of the birefringence of the detection fiber defines how often the polarization control is necessary. Using the above scheme, this is done every ten minutes. In Sec. 2.2 of the first chapter we presented the mean drift of the detection fiber

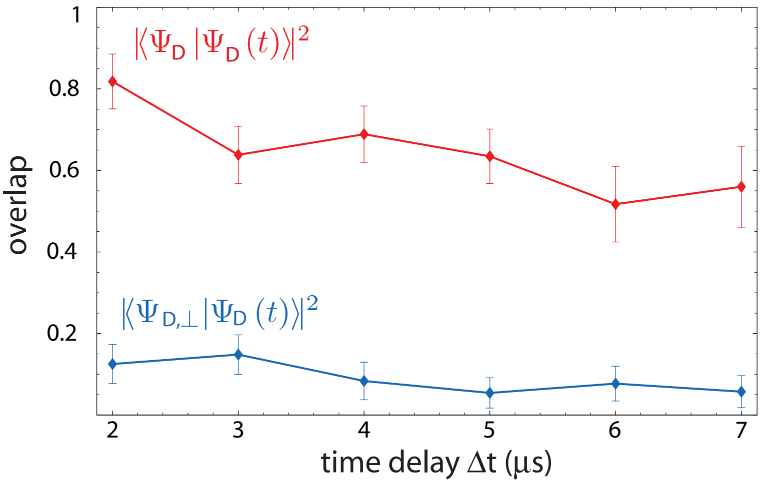

Figure 3.12: Measured overlap between the initially prepared state $|\Psi_D\rangle$ (see eqn. 3.25) and the measured state $|\Psi_D(t)\rangle$ (blue curve) and the overlap between the measured one and the corresponding orthogonal state $|\Psi_{D,\perp}\rangle$ (red curve) for different delay times. A weak magnetic guiding field of $B = 30$ mG, stabilizing the bright state was applied.

during 10 minutes. The mean deviation from the input state after 10 min is 0.56%, which is negligible for the analysis of atom-photon entanglement.

3.5 Long distance atom-photon entanglement

3.5.1 Coherence time measurement

The measurement of the correlations between the atomic state and the polarization state of the photon takes place with a delay of 2 μs between the generation and analysis due to the extension to the 300 m optical fiber. During this time, the atom states couple due to magnetic field fluctuations, leading to an effective decoherence of the atomic state. It is important to know on which timescale the decoherence of the atom takes place, as it gives an upper bound for the expected fidelity of the atom-photon correlations.

The measurement of the coherence time is realized by preparing the atom in a well defined state $|\Psi_D\rangle$ and delaying its readout for a time Δt. By repeating the measurement we get a histogram, containing the overlap between the detected state $|\Psi_D(t)\rangle$ and the initial one $|\Psi_D\rangle$.

Practically, the preparation is realized by projecting the atom in the state $|\Psi_D\rangle$ using the single photon detection. After a time delay the atomic state is read out by the STIRAP process. The analysis basis is chosen in a way that $|\Psi_D(t)\rangle$ is the dark state of the STIRAP light field. If the atom is still trapped in the dipole trap after applying the projection pulse,

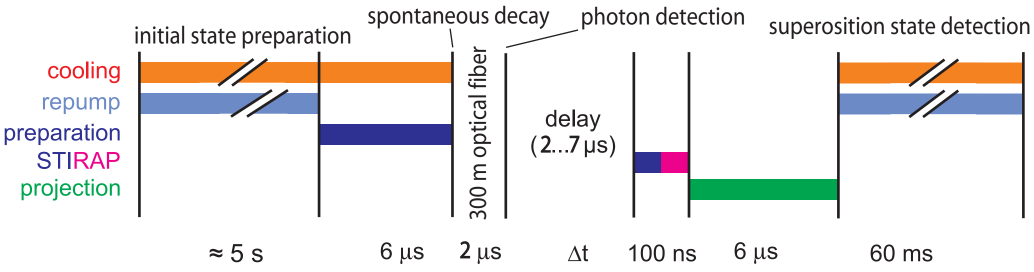

Figure 3.13: Timing sequence of the coherence time measurement. First the atom is prepared according to sec. 3.3.3. Then the spontaneous decay takes place and the emitted photon is guided through the fiber and finally detected, projecting the atom into the desired states. After an additional time delay the atomic state is read out with the procedure explained in sec. 3.3.4.

the final atomic state was projected onto $|\Psi_D\rangle$. Otherwise, the evolved state is projected into a state $|\Psi_{D,\perp}\rangle$ orthogonal to $|\Psi_D\rangle$. $|\Psi_{D,\perp}\rangle$ is a superposition of the bright state $|\Psi_B\rangle$ of the STIRAP light and the $F = 1,\ m_F = 0$ state.

In the performed measurement the photon was detected in the H/V basis and the STIRAP light field was horizontally polarized to get maximal contrast. The atom-photon state in this basis reads:

$$|\Psi\rangle = \frac{1}{\sqrt{2}}(|\Psi_D\rangle\,|H\rangle + |\Psi_B\rangle\,|V\rangle), \tag{3.24}$$

with the prepared and analyzed dark state

$$|\Psi_D\rangle = \frac{1}{\sqrt{2}}(|1,-1\rangle + |1,+1\rangle) \tag{3.25}$$

and the corresponding bright state

$$|\Psi_B\rangle = \frac{1}{\sqrt{2}}(|1,-1\rangle - |1,+1\rangle) \tag{3.26}$$

Fig. 3.12 shows this coherence time measurement. The graphs show the measured overlaps of the detected state $|\Psi_D(t)\rangle$ with the prepared one $|\Psi_D\rangle$ and the orthogonal state $|\Psi_{D,\perp}\rangle$. The measurement starts at a time delay of approximately 2 μs, which is the time delay induced by the 300 m fiber, but we know from previous measurements that the overlap with $|\Psi_D\rangle$ is approximately 0,9 at $\Delta t = 0$. The timing sequence of the measurement is shown in fig. 3.13.

From the measurement we obtain a coherence of approximately 5 μs and the overlap with the initial state after 2 μs is approximately 0.82. For this measurement a guiding

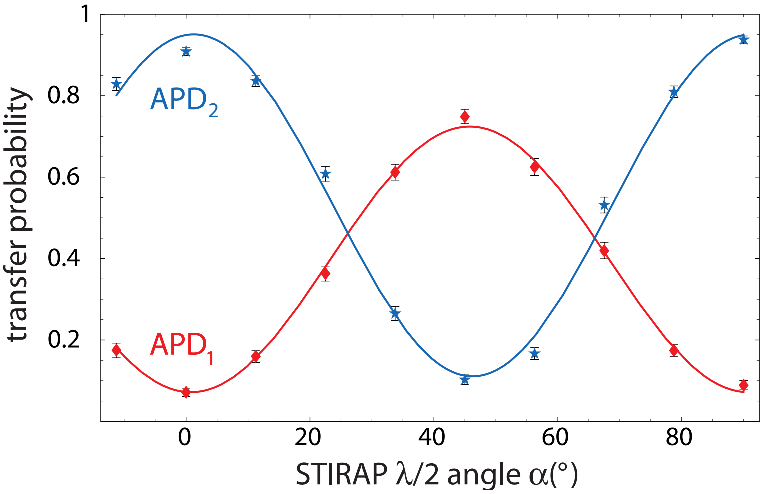

Figure 3.14: Graphs of the measurement of atom-photon correlations. The figure shows the transfer probability of the STIRAP process as a function of the setting of the half wave plate defining the STIRAP polarization. The photonic detection basis is H/V. The solid curves are sinusoidal fits of the measured data.

magnetic field perpendicular to the quantization axis was applied, stabilizing the bright state of above STIRAP configuration. This field of B=30 mG, caused an energy splitting of less than 50kHz, being negligible to the natural linewidth of 6MHz for the spontaneous decay.

3.5.2 Correlation measurement

To show that entanglement between the atomic and the photonic state still exists a correlation measurement was performed (fig. 3.14) by generating entanglement between an atom and a photon and sending the latter through the 300 m detection fiber.
In this measurement the polarization of the STIRAP light was rotated with a $\lambda/2$-wave plate to analyze the atom in different bases following from the polarization. The analysis basis of the atom is given by the dark and bright state of the atom with respect to the STIRAP light field (see sec. 3.3.4), defined by the angle α of the half wave plate (the light field is initially vertically polarized):

$$|\Psi_{at,D}(\alpha)\rangle = \frac{1}{\sqrt{2}}(|1,-1\rangle - e^{-4i\alpha}|1,+1\rangle) \tag{3.27}$$

$$|\Psi_{at,B}(\alpha)\rangle = \frac{1}{\sqrt{2}}(|1,-1\rangle + e^{-4i\alpha}|1,+1\rangle) \tag{3.28}$$

The photon was analyzed in the H/V-basis. The same guiding field as in the coherence time measurement was applied. The measurement of the photon projects the atom into

$$|\Psi_{at,\pm}\rangle = \frac{1}{\sqrt{2}}(|1,-1\rangle \pm |1,+1\rangle), \tag{3.29}$$

where the "+" sign corresponds to the detection of the photon in APD_1 (projection onto $|H\rangle$) and the "$-$" sign to a detection event in APD_2 (projection onto $|V\rangle$), respectively. The overlap of the atomic state $|\Psi_{at,\pm}\rangle$ with the dark state $|\Psi_{at,D}(\alpha)\rangle$ of the STIRAP process for the halfwave plate at an angle α is

$$|\langle\Psi_{at,D}(\alpha)|\Psi_{at,\pm}\rangle|^2 = \frac{1}{2}(1 \mp \cos(4\alpha)) \tag{3.30}$$

The measurement in fig. 3.14 shows this expected behavior. The solid lines are sinusoidal fits to the measured data. From the two fits we obtain a visibility (defined as peak to peak amplitude) of $V_V = 0.65 \pm 0.01$ and $V_H = 0.84 \pm 0.01$ resulting in an average visibility of $V_{av} = 0.75 \pm 0.01$. The difference between the visibilities is due to the guiding field, stabilizing the dark state of the vertically polarized STIRAP light (eqn. 3.27 with $\alpha = 0$). The magnetic field does not help against decoherence of the dark state of the horizontally polarized STIRAP light field as it is no eigenstate of the magnetic field and thus the decoherence is stronger, resulting in above visibilities.

Despite of decoherence effects, the measurement shows strong correlations between the atomic and the photonic state and therefore clearly indicate that the combined atom-photon state is still entangled after the 300 m optical fiber.

3.6 Summary

This chapter explained the importance of entanglement from a fundamental point of view, namely to disprove LHV theories by violating Bell's inequality. The way entanglement between a single ^{87}Rb atom and a photon can be achieved was described as well as the experimental realization. The extension of the experiment to verify atom-photon entanglement over long distances was performed by implementing the necessary polarization control setup. Finally, the achieved results show strong correlations between matter and light that passed a distance of 300 m with an average visibility of $V_{av} = 0.75 \pm 0.01$ with a coherence time of the atomic state of approximately 5 μs. This is an important step towards the entanglement of two atoms, that are spatially separated far enough to close the locality loophole. The high detection efficiency of their internal states together with a space-like separation would then allow a final, loophole-free test of Bell's inequality.

Chapter 4

Towards quantum teleportation and entanglement swapping

One of the key elements of quantum information and quantum computation protocols is the Bell-state measurement which projects the measured particles onto the basis defined by the four Bell-states. The experiments that are being set up by our group will exploit two of these protocols: The quantum teleportation of a polarization state of a photon onto the spin-state of a single ^{87}Rb atom and the entanglement swapping between two atom-photon pairs to generate an entangled pair of ^{87}Rb atoms. In this chapter these protocols and their feasibility will be analyzed. Because there is no way to perform a full Bell state analysis with only linear interactions, we analyze the two-photon interference at a beamsplitter that allows to distinguish one of the four Bell states from the others ($|\Psi^+\rangle$ or $|\Psi^-\rangle$, depending on the beamsplitter; see the next but one section). Therefore, in this chapter, we will first have a closer look at two photon interference for photons generated by spontaneous decay. At the end of this chapter typical values for the different parameters of these photons are provided to give an overview of the expected results from the upcoming measurements.

4.1 Protocols

The following section introduces two basic protocols, quantum teleportation [37, 38] used to distribute arbitrary quantum states and entanglement swapping [20] allowing to generate entanglement between remote systems.

4.1.1 Quantum teleportation

The main idea behind quantum teleportation is to transfer an unknown quantum state from one system to another spatially separated one [37, 38]. For this purpose the

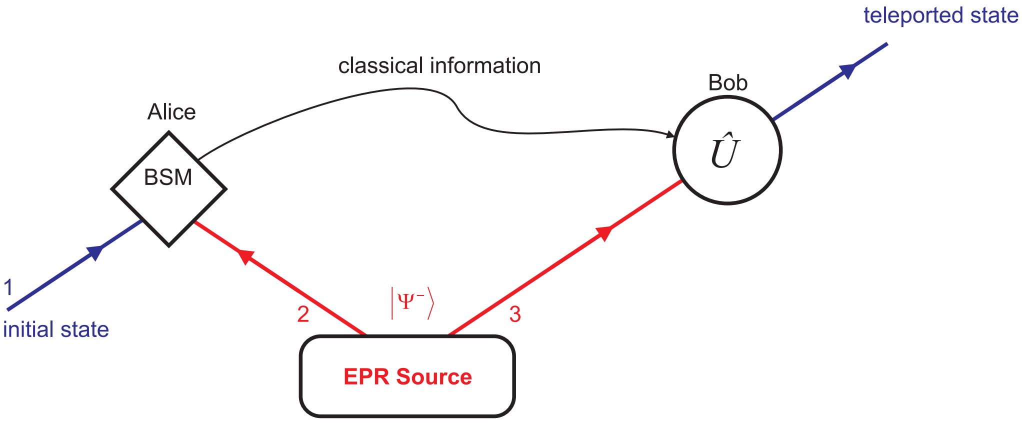

Figure 4.1: Scheme of quantum teleportation. The initial particle (1) and one of the entangled state (2) are sent to Alice, who performs a Bell-state measurement (BSM) on these particles. Depending on her outcome she tells Bob which unitary transformation he has to use on particle (3) to reconstruct the initial state.

Sender "Alice" and the Receiver "Bob" share a pair of entangled particles and use classical information channels.

Measuring the state of the particle and just sending the result to Bob does not enable Alice to fulfill the task, since according to the projection postulate the measurement will destroy the quantum state not leaving the necessary information to reconstruct it. To bypass this problem Alice and Bob have to initially share an entangled state, let's say a $|\Psi^-\rangle$-state. If we label the incoming particle $|\Psi\rangle = \alpha\,|0\rangle + \beta\,|1\rangle$ by 1 and the entangled particles by 2 and 3 (see fig. 4.1) the combined three photon state can be written as

$$\begin{aligned}|\Psi\rangle_{123} = |\Psi\rangle_1 \otimes |\Psi^-\rangle_{23} \quad = \quad & \tfrac{1}{2}[|\Psi^-\rangle_{12}\,(-\alpha\,|0\rangle_3 - \beta\,|1\rangle_3) \\ & +|\Psi^+\rangle_{12}\,(-\alpha\,|0\rangle_3 + \beta\,|1\rangle_3) \\ & +|\Phi^-\rangle_{12}\,(+\beta\,|0\rangle_3 + \alpha\,|1\rangle_3) \\ & +|\Phi^+\rangle_{12}\,(-\beta\,|0\rangle_3 + \alpha\,|1\rangle_3)].\end{aligned} \tag{4.1}$$

Performing a measurement on the particles 1 and 2 in the Bell-basis, Alice projects particle 3 into one of four possible states (see eqn. [4.1]). If, for example, Alice measures $|\Psi^-\rangle_{12}$, particle 3 is, except from a global phase, in the same state as particle 1 was before the measurement took place. In the remaining three cases Bob has to perform a unitary transformation that depends on Alice's measurement outcome. This information is sent from Alice to Bob via classical communication channels. Thus by sending two bit of classical information it is possible to realize a full transfer of an unknown state from Alice to Bob.

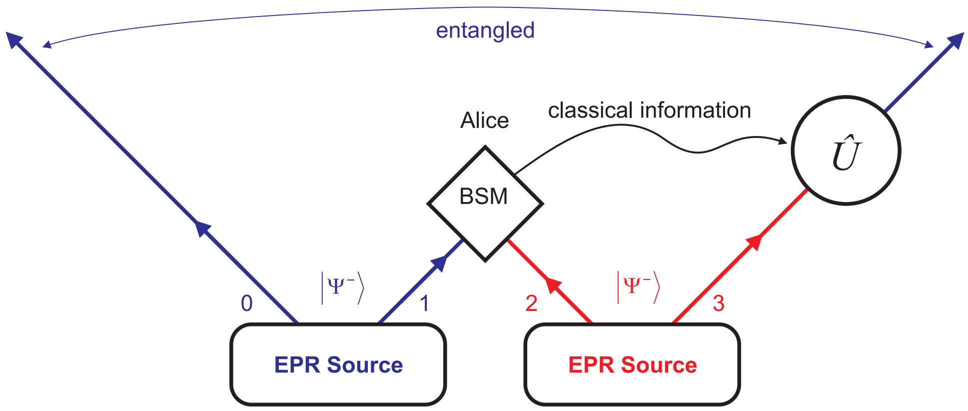

Figure 4.2: Entanglement swapping scheme. After Alice has performed a Bell-state measurement on the particles (1) and (2) the particles (0) and (3) are entangled.

4.1.2 Entanglement swapping

The main idea of this protocol is to entangle two particles that never interacted with each other. It is an extension of the teleportation protocol [20]. The main difference is that the initial particle 1 now is part of an entangled pair itself. Assuming particle 1 to be entangled with a new particle 0 (in a $|\Psi^-\rangle_{01}$-state; see fig. 4.2) we can write the combined four particle state as

$$\begin{aligned} |\Psi\rangle_{0123} = |\Psi^-\rangle_{01} \otimes |\Psi^-\rangle_{23} \quad = \quad & \tfrac{1}{2}[|\Psi^+\rangle_{03}\,|\Psi^+\rangle_{12} - |\Psi^-\rangle_{03}\,|\Psi^+\rangle_{12} \\ & - |\Phi^-\rangle_{03}\,|\Phi^-\rangle_{12} + |\Phi^+\rangle_{03}\,|\Phi^+\rangle_{12}]. \end{aligned} \tag{4.2}$$

If Alice now performs a measurement in the Bell-basis on the particles 1 and 2 the remaining two particles are left in an entangled state. If Bob uses the same unitary transformations as in the teleportation protocol the final entangled state $|\Psi\rangle_{03}$ is in the same state as the initial one $|\Psi\rangle_{01}$ was before the measurement took place. This protocol allows in principle to entangle particles over arbitrary distances without the need of direct interaction, what makes it important for quantum information and communication tasks.

4.1.3 Action of a beamsplitter

The two presented protocols rely on the Bell state measurement. A measurement, distinguishing all four Bell states can not be realized with only linear optical elements. The simplest way to perform a Bell state analysis is to overlap two photons on a beamsplitter. Depending from the outcome behind the beamsplitter, one can distinguish the projection of the photons onto one of the Bell states from the projection onto the other three (see

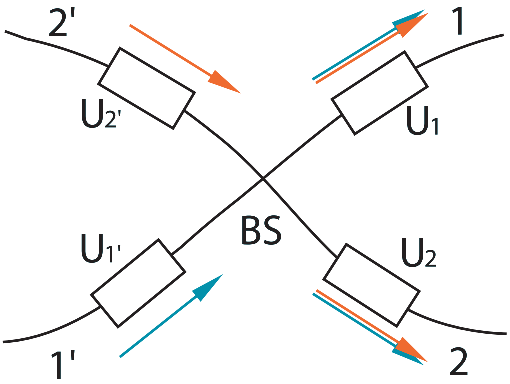

Figure 4.3: Scheme of two lightfields passing a fiber beamsplitter, the transformations of the polarizations caused by birefringence in the fiber are given by unitary transformations U_i.

below, sec. 4.2). This is the method we have chosen for the experimental realization of above protocols. A crucial point therefore is the full knowledge of the used beamsplitter. In Appendix A.3, the general requirements the theoretical description of a beamsplitter has to obey are shown and the behavior of a commercially available free space beamsplitter and a fiber beamsplitter is explained.

In the upcoming experiment we will use a fiber beamsplitter to perform the Bell state measurement, because the splitting ratio is much better than the one of a free space beamsplitter, the mode overlap is perfect and interference can be optimized by transforming the birefringence of the incoming fibers.

We want the beamsplitter to split up the $|\Psi^-\rangle$-state, as its representation is the same in all measurement bases. The condition therefore is, that the photons arriving at the beamsplitter have passed the same unitary transformations, i.e. $U_{1'} = U_{2'}$ (see Appendix A.3.3).

We suppose that the beamsplitter is adjusted such, that the eigenpolarizations of the system are $|H\rangle$ and $|V\rangle$. The transformation of the polarization of light fields reads (for a general fiber BS with transmittances x and y for $|H\rangle$- ($|V\rangle$-) polarized light):

$$\hat{c}_{\chi,H,1'} \overset{\hat{BS}}{\rightarrow} \sqrt{x}\,\hat{c}_{\chi,H,1} + \sqrt{1-x}\,\hat{c}_{\chi,H,2} \tag{4.3}$$

$$\hat{c}_{\chi,H,2'} \overset{\hat{BS}}{\rightarrow} -\sqrt{1-x}\,\hat{c}_{\chi,H,1} + \sqrt{x}\,\hat{c}_{\chi,H,2} \tag{4.4}$$

$$\hat{c}_{\chi,V,1'} \overset{\hat{BS}}{\rightarrow} \sqrt{y}\,\hat{c}_{\chi,V,1} + \sqrt{1-y}\,\hat{c}_{\chi,V,2} \tag{4.5}$$

$$\hat{c}_{\chi,V,2'} \overset{\hat{BS}}{\rightarrow} -\sqrt{1-y}\,\hat{c}_{\chi,V,1} + \sqrt{y}\,\hat{c}_{\chi,V,2} \tag{4.6}$$

The states of the photons $\hat{c}_{\chi,H/V,i}$ are explained in Appendix A.2.3 and describe a single photon in the time domain being in mode i with the polarization H/V at the point

$z = 0$ (where the beamsplitter is located) and an temporal amplitude distribution function $\chi(t)$. Other choices of the phases are also possible (see App. A.3.3). But, since they doesn't change the two-photon interference, we chose the ones most comfortable for calculations. The calculations presented in the next section are made using above description of a beamsplitter.

We will describe the states in the H/V-basis later on . Therefore, the transformation of the following basis-states describing two photon states with each photon being in a different spatial input mode are considered:

$$
\begin{aligned}
|i_{HH}\rangle &= \hat{c}^{(\dagger)}_{\chi,H,1'}\hat{c}'^{(\dagger)}_{\chi',H,2'}|0\rangle && (4.7)\\
|i_{VV}\rangle &= \hat{c}^{(\dagger)}_{\chi,V,1'}\hat{c}'^{(\dagger)}_{\chi',V,2'}|0\rangle && (4.8)\\
|i_{VH}\rangle &= \hat{c}^{(\dagger)}_{\chi,V,1'}\hat{c}'^{(\dagger)}_{\chi',H,2'}|0\rangle && (4.9)\\
|i_{HV}\rangle &= \hat{c}^{(\dagger)}_{\chi,H,1'}\hat{c}'^{(\dagger)}_{\chi',V,2'}|0\rangle && (4.10)
\end{aligned}
$$

using $\hat{c}'^{(\dagger)}_{\chi',H/V,j} := \hat{c}^{(\dagger)}_{\chi',H/V,j}(t'_0,\omega'_0,\tau')$, χ' and χ arbitrary functions that do not necessarily need to be equal and $j \in \{1,2\}$ representing the spatial mode. Behind the BS these initial states are transformed into $|f_m\rangle = \hat{BS}\,|i_m\rangle$. These final states are:

$$
\begin{aligned}
|f_{HH}\rangle &= (\sqrt{x}\,\hat{c}^\dagger_{\chi,1,H} + \sqrt{1-x}\,\hat{c}^\dagger_{\chi,2,H})(-\sqrt{1-x}\,\hat{c}^\dagger_{\chi',1,H} + \sqrt{x}\,\hat{c}^\dagger_{\chi',2,H})\,|0\rangle = \\
&= [\sqrt{x(1-x)}(-\hat{c}^\dagger_{\chi,1,H}\hat{c}^\dagger_{\chi',1,H} + \hat{c}^\dagger_{\chi,2,H}\hat{c}^\dagger_{\chi',2,H}) \\
&\quad + x\,\hat{c}^\dagger_{\chi,1,H}\hat{c}^\dagger_{\chi',2,H} + (x-1)\,\hat{c}^\dagger_{\chi,2,H}\hat{c}^\dagger_{\chi',1,H}]\,|0\rangle && (4.11)\\
|f_{VV}\rangle &= [\sqrt{y(1-y)}(-\hat{c}^\dagger_{\chi,1,V}\hat{c}^\dagger_{\chi',1V} + \hat{c}^\dagger_{\chi,2,V}\hat{c}^\dagger_{\chi',2,V}) \\
&\quad + y\,c^\dagger_{\chi,1,V}\hat{c}^\dagger_{\chi',2,V} + (y-1)\,\hat{c}^\dagger_{\chi,2,V}\hat{c}^\dagger_{\chi',1,V}]\,|0\rangle && (4.12)\\
|f_{VH}\rangle &= [-\sqrt{(1-x)y}\,\hat{c}^\dagger_{\chi,1,V}\hat{c}^\dagger_{\chi',1,H} + \sqrt{(1-y)x}\,\hat{c}^\dagger_{\chi,2,V}\hat{c}^\dagger_{\chi',2,H} \\
&\quad + \sqrt{xy}\,\hat{c}^\dagger_{\chi,1,V}\hat{c}^\dagger_{\chi',2,H} - \sqrt{(x-1)(y-1)}\,\hat{c}^\dagger_{\chi,2,V}\hat{c}^\dagger_{\chi',1,H}]\,|0\rangle && (4.13)\\
|f_{HV}\rangle &= [-\sqrt{(1-y)x}\,\hat{c}^\dagger_{\chi,1,H}\hat{c}^\dagger_{\chi',1,V} + \sqrt{(1-x)y}\,\hat{c}^\dagger_{\chi,2,H}\hat{c}^\dagger_{\chi',2,V} \\
&\quad + \sqrt{xy}\,\hat{c}^\dagger_{\chi,1,H}\hat{c}^\dagger_{\chi',2,V} - \sqrt{(x-1)(y-1)}\,\hat{c}^\dagger_{\chi,2,H}\hat{c}^\dagger_{\chi',1,V}]\,|0\rangle && (4.14)
\end{aligned}
$$

Later on, the point of interest is the probability of having one photon in every output mode of the beamsplitter. In the above equations only terms with $\hat{c}^\dagger_1$ as well as $\hat{c}^\dagger_2$ are describing this situation. Thus, only these terms will contribute. We should mention that every superposition of the initial states before the beamsplitter transforms into the superposition of the according final states.

4.2 Two-photon interference

In this section the interference of two independent photons, generated by spontaneous decay arriving at a beamsplitter in different spatial modes will be calculated. First, we will give introduction into the description of single photon and joint two photon detection without time resolution what leads to the Hong-Ou-Mandel dip [39] considering the probability for a click in both detectors each (a conincidence). Next,time-resolved two photon detection is theoretically analyzed. This will lead to a beat in the coincidence probability. In the last part of this section we apply this theory on our experimental situation and calculate the expected efficiency of the entanglement swapping and teleportation protocol.

4.2.1 Theory of (two-) photon detection

The $G^{(1)}$-function and single photon detection

The detection of a single photon corresponds to the measurement of the expectation value of the normally ordered product $\hat{E}^{-}(\mathbf{r},t)\hat{E}^{+}(\mathbf{r},t)$ since this represents the expectation value of an atom being photoionized by the photon. The electric field operators $\hat{E}^{-}(\mathbf{r},t)$ and $\hat{E}^{+}(\mathbf{r},t)$ are defined in App. A.3.4. The detection probability of a single photon in the time interval dt around the time t_0 is given by [40]

$$P^{(1)}(z_0,t_0,dt) = \eta \int_{t_0-dt/2}^{t_0+dt/2} dt'\, G^{(1)}(z_0,t')\ , \tag{4.15}$$

where η defines the quantum efficiency of the detector and $G^{(1)}(z_0,t')$ refers to the first order correlation function $G^{(1)}(z_0,t_1,t_2)$ for $t_1 = t_2 := t'$. This function is defined by the expectation value of the normally ordered product of the electrical field operators

$$G^{(1)}(z_0,t_1,t_2) := \left\langle \hat{E}^{-}(z_0,t_1)\hat{E}^{+}(z_0,t_2)\right\rangle \tag{4.16}$$

Replacing $\hat{a}_s(\omega)$ by $\hat{a}_s(q)$ in $\hat{E}^{-}(\mathbf{r},t)$ and $\hat{E}^{+}(\mathbf{r},t)$ (see eqn.[A.18]) and just looking at $z_0 = 0$, the correlation function becomes

$$G^{(1)}(z_0=0,t_1,t_2) = G^{(1)}(t_1,t_2) = \sum_s \left\langle \hat{a}_s^{\dagger}(t_1)\hat{a}_s(t_2)\right\rangle . \tag{4.17}$$

The $G^{(2)}$-function and joint two-photon detection

Two-photon interference effects are to revealed by the correlation of the signals of two detectors. The description of photon detection so far must be extended to the joint measurement of two photons at two independent detectors with the same time resolution. The probability of a joint photon-detection, detecting one photon in one detector each, placed at distances r_1,r_2 from the source in the time-window dt around t_{01} and t_{02} respectively is analog to eqn. [4.15]

$$P^{(2)}(t_{01}, t_{02}, r_1, r_2, dt) = \eta_1\eta_2 \int_{t_0-dt/2}^{t_{01}+dt/2} dt_1 \int_{t_0-dt/2}^{t_{02}+dt/2} dt_2\, G^{(2)}(t_1, t_2, r_1, r_2) \tag{4.18}$$

From now one we will set $r_1, r_2 = 0$, what means that both detectors have the same distance from the photon source, i.e. the beamsplitter. The quantum efficiency of both detectors is given by η_1 and η_2 respectively. $G^{(2)}(t_1, t_2)$ is the second-order correlation function [41], that can be expressed using the narrow-band condition for the electric fields (see App. A.3.4):

$$G^{(2)}(t_1, t_2) = \sum_{s,s'} \left\langle \hat{a}^\dagger_{1,s}(t_1)\hat{a}^\dagger_{2,s'}(t_2)\hat{a}_{1,s}(t_1)\hat{a}_{2,s'}(t_2)\right\rangle . \tag{4.19}$$

The subscripts 1 and 2 indicate the spatial mode and $s, s' \in \{H, V\}$. Applying this to the case of two photon interference on a beamsplitter, the expectation value has to be taken with respect to the states behind the beamsplitter:

$$G^{(2)}_m(t_1, t_2) = \sum_{s,s'} \langle f_m| \hat{a}^\dagger_{1,s}(t_1)\hat{a}^\dagger_{2,s'}(t_2)\hat{a}_{1,s}(t_1)\hat{a}_{2,s'}(t_2) |f_m\rangle \ , \tag{4.20}$$

where m denotes the initial polarization state in the H/V-basis. This can be rewritten by using the completeness of $|f_m\rangle$, i.e. $\sum_{m\in\{HH,VV,HV,VH\}} |f_m\rangle \langle f_m| = \mathbb{1}$ to

$$G^{(2)}_m(t_1, t_2) = \sum_{s,s'} \left|\hat{a}_{1,s}(t_1)\hat{a}_{2,s'}(t_2) |f_m\rangle\right|^2 \ . \tag{4.21}$$

Because

$$\langle f_{VV}| \hat{a}^\dagger_{1,s}(t_1)\hat{a}^\dagger_{2,s'}(t_2)\hat{a}_{1,s}(t_1)\hat{a}_{2,s'}(t_2) |f_{HH}\rangle = 0 \ , \tag{4.22}$$

the second order correlation function of the Bell-states $|\Phi^\pm\rangle = \frac{1}{\sqrt{2}} (|i_{HH}\rangle \pm |i_{VV}\rangle)$ reads, after the beamsplitter:

$$G^{(2)}_{\Phi^\pm} = \frac{1}{2}\left(G^{(2)}_{HH} + G^{(2)}_{VV}\right) \tag{4.23}$$

Thus it is sufficient to consider only $|f_{HH}\rangle$ and$|f_{VV}\rangle$ since the superpositions of these states won't give any new features concerning the two-photon interference. Calculating the expectation values using eqn. [A.21] we get the result (only terms with $s = s'$ contribute):

$$G^{(2)}_{HH}(t_1, t_2) = \left|x\ \chi(t_1)\chi'(t_2) + (x-1)\ \chi(t_2)\chi'(t_1)\right|^2 \tag{4.24}$$

$$G^{(2)}_{VV}(t_1, t_2) = \left|y\ \chi(t_1)\chi'(t_2) + (y-1)\ \chi(t_2)\chi'(t_1)\right|^2 \tag{4.25}$$

The situation is different for the other two Bell states $|\Psi^\pm\rangle = \frac{1}{\sqrt{2}} (|i_{HV}\rangle \pm |i_{VH}\rangle)$. For the states the crossterms in the $G^{(2)}$-function behind the beamsplitter are not zero

$$K_{s,s'}(t_1,t_2) = \langle f_{HV}|\, \hat{a}^\dagger_{1,s}(t_1)\hat{a}^\dagger_{2,s'}(t_2)\hat{a}_{1,s}(t_1)\hat{a}_{2,s'}(t_2)\,|f_{VH}\rangle \neq 0, \quad (s \neq s') \tag{4.26}$$

From eqn. 4.20 and the above equation we obtain

$$G^{(2)}_{\Psi^\pm}(t_1,t_2) = \frac{1}{2}\left[G^{(2)}_{HV}(t_1,t_2) + G^{(2)}_{VH}(t_1,t_2) \pm 2\left(\sum_{\substack{s,s'\in\{H,V\}\\ s\neq s'}} K_{s,s'}(t_1,t_2)\right)\right] \tag{4.27}$$

Inserting the states representing the photons having passed the beamsplitter and using eqn. [A.21] we obtain with $K_{s,s'}(t_1,t_2) := K_{s,s'}$:

$$\begin{aligned} G^{(2)}_{HV}(t_1,t_2) &= xy\left|\chi(t_1)\chi'(t_2)\right|^2 + (1-x)(1-y)\left|\chi(t_2)\chi'(t_1)\right|^2) && (4.28)\\ G^{(2)}_{VH}(t_1,t_2) &= xy\left|\chi(t_1)\chi'(t_2)\right|^2 + (1-x)(1-y)\left|\chi(t_2)\chi'(t_1)\right|^2) && (4.29)\\ \sum_{\substack{s,s'\in\{H,V\}\\ s\neq s'}} K_{s,s'} &= -2\sqrt{xy(1-x)(1-y)}\, Re\left[\chi(t_1)\chi'(t_2)\chi^*(t_2)\chi'^*(t_1)\right] && (4.30)\end{aligned}$$

The crucial point is, that in this case there is a difference if we consider the effects of a beamsplitter on the states $|i_{HH}\rangle$ and $|i_{VV}\rangle$ or on the Bell-states $|\Psi^\pm\rangle$. For the Bell-states interference effects occurs from the last term of eqn 4.27 (see next sections), whereas the outcome of two photons, which are initially in $|i_{HH}\rangle$ or $|i_{VV}\rangle$ after a beamsplitter is completely random. For our experiment only the states $|\Psi^\pm\rangle$ are of interest, thus in the following only these two states are considered.

For the following considerations, the detection window T_d is an important parameter. In reality this window can't be chosen arbitrarily small, but it is limited by the detector itself and its electronics. We will consider two cases, one where the photons are so narrow-band that the detection window becomes much smaller than the photon duration and one where the photon duration is much shorter than the detection window. The latter case is the time-integral over the detection with time resolution. Therefore it is just introduced very shortly at the beginning of the next section.

Detection with time resolution

If we look at very long photons, e.g. very narrow-band ones, the time resolution of the detectors is much smaller than the duration of the photon, i.e. $min(\tau,\tau') >> \; T_d$. So the detection process can be localized within the photon durations with the time-resolution Δt_{det}. We can assume that $G^{(2)}$ is constant within the time-resolution T_d. Rewriting $G^{(2)}(t_1,t_2) = G^{(2)}(t,t+\delta T)$ with $t_1 = t$, and $\delta T = t_2 - t$ the probability

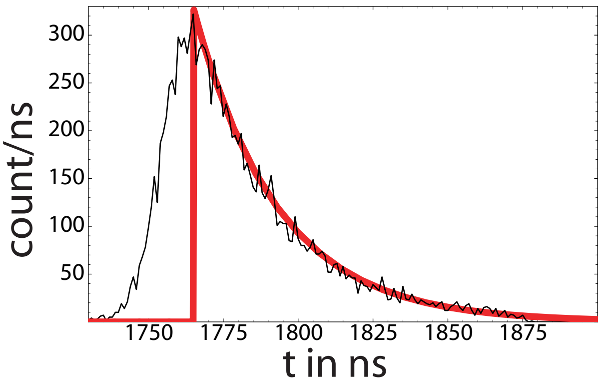

Figure 4.4: Experimentally measured probability distribution (black curve)and fitted function $|\chi|^2$ (red curve).

to detect one photon at the time t in detector 1 and to detect a photon at $t + \delta T$ in detector 2 reads:

$$P^{(2)}(t, t + \delta T) = \eta_1 \eta_2 T_{d1}\, T_{d2}\, G^{(2)}(t, t + \delta T)\ , \tag{4.31}$$

where T_{d1} and T_{d2} are the detection windows of detector 1 and detector 2, respectively. Since we are just interested in the time difference between two detections we can integrate over the detection time t, with $T_{d1} \rightarrow dt$. Renaming the detector resolution T_d instead of T_{d2} we get:

$$P^{(2)}(\delta T) = \eta_1 \eta_2 T_d \int_{-\infty}^{\infty} dt\ G^{(2)}(t, t + \delta T) \tag{4.32}$$

4.2.2 Two photon interference *without* time resolution

Detection without time resolution

The case of no time resolution occurs if the photon durations τ, τ' are much smaller than the time resolution T_d of the detectors $max(\tau, \tau') << T_d$. In this case the integration limits can be extended to $\pm\infty$ and we get:

$$P^{(2)} = \eta_1 \eta_2 \int_{-\infty}^{\infty} dt_1 \int_{-\infty}^{\infty} dt_2\ G^{(2)}(t_1, t_2) \tag{4.33}$$

Description of photons generated by spontaneous decay

The temporal shape of photons from spontaneous decay is in a very good approximation (except from the excitation) described at the detector with the following amplitude function:

$$\chi(t, t_0, \omega_0, \tau) = \sqrt{2/\tau}\, e^{-(t-t_0)/\tau} \Theta(t - t_0) e^{-i\omega_0 t} \tag{4.34}$$

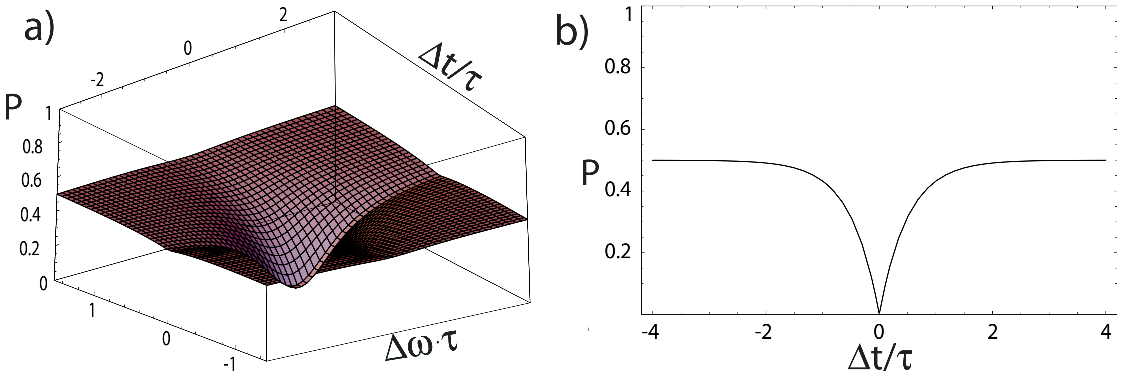

Figure 4.5: a) Graph of the coincidence probability P_{HH,VV,Ψ^+} for a $|HH\rangle, |VV\rangle$ and a $|\Psi^+\rangle$-state having passed a beamsplitter with $x = y = 0.5$. The photons durations are the same $\tau' = \tau$. b) shows a cut through the first graph along the time-axis at frequency-difference $\triangle\omega = 0$

with ω_0 defining the central frequency, t_0 the arrival (or creation-) time and τ the photon duration. Knowing this, the choice for $\chi(t) = \chi(t, t_0, \omega_0, \tau)$. For the state of a photon follows (see App. A.2.3):

$$|\psi\rangle = \hat{c}^{\dagger}_{\chi,H/V} |0\rangle = \sqrt{2/\tau} \int dt e^{-(t-t_0)/\tau} \Theta(t - t_0) e^{-i\omega_0 t} \hat{a}^{\dagger}_{H,V}(t) |0\rangle \tag{4.35}$$

$$\hat{c}^{(\dagger)}_{\chi,H/V} = \hat{c}^{(\dagger)}_{\chi,H/V}(t_0, \omega_0, \tau) \tag{4.36}$$

The photons to be analyzed in the following sections will be described by this temporal shape. From now on we will write P instead of $P^{(2)}$.

Interference effects

Having done the work in the preceding sections, what remains to do is solving the integral in eqn. [4.33] for the $G^{(2)}$-functions given in section 4.2.1. χ as well as χ' are the functions defined to describe our photons (see eqn. [4.34]). Putting all together, restricting ourselves to photons with the same duration $\tau' = \tau$, defining the creation time delay $\triangle t = t_0 - t'_0$ (we consider all distances to be the same for both photons), the frequency difference $\triangle\omega = \omega_0 - \omega'_0$ and supposing the detectors have perfect efficiency $\eta_1 = \eta_2 = 1$ we get ($P_m := P_m(\triangle t, \tau, \triangle\omega)$):

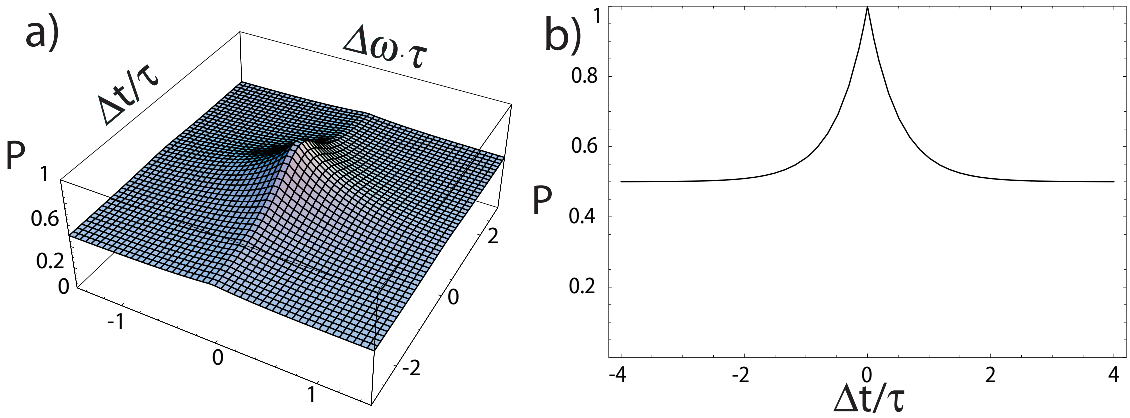

Figure 4.6: a) Graph of the coincidence probability P_{Ψ^-} for a $|\Psi^-\rangle$-state having passed a beamsplitter with $x = y = 0.5$. The photons durations are the same $\tau' = \tau$. b) shows a cut through the first graph along the time-axis at frequency-difference $\triangle\omega = 0$

$$P_{HH} = 1 + 2x(x-1)\left(1 + \frac{e^{-2|\triangle t|/\tau}}{1 + \left(\frac{\tau\triangle\omega}{2}\right)^2}\right) \tag{4.37}$$

$$P_{VV} = 1 + 2y(y-1)\left(1 + \frac{e^{-2|\triangle t|/\tau}}{1 + \left(\frac{\tau\triangle\omega}{2}\right)^2}\right) \tag{4.38}$$

$$P_{\psi^\pm} = (1-x)(1-y) \mp 2\sqrt{xy(1-x)(1-y)}\left(1 + \frac{e^{-2|\triangle t|/\tau}}{1 + \left(\frac{\tau\triangle\omega}{2}\right)^2}\right) \tag{4.39}$$

One observes that only for the $|\Psi^-\rangle$-state the probability to get a coincidence in the detectors exceeds the value 0.5 (see fig. 4.6), in the other cases the probability is always less than 0.5 (see fig. 4.5) what means the photons prefer to leave the beamsplitter in the same spatial mode (photon bunching), when they have the same polarization or are in a $|\Psi^+\rangle$-state.

4.2.3 Two photon interference *with* time resolution

Since the detectors in this case can resolve the photon durations we get in addition to the arrival time difference $\triangle t = t_0 - t_0'$ and the frequency difference $\triangle\omega = \omega_0 - \omega_0'$ a third degree of freedom: The detection time difference δT, defined in section 4.2.1. Thus $P_m := P_m(\delta T, \triangle t, \triangle\omega, \tau, \tau')$. Solving the integral in eqn. 4.32 for the above $G^{(2)}$-function

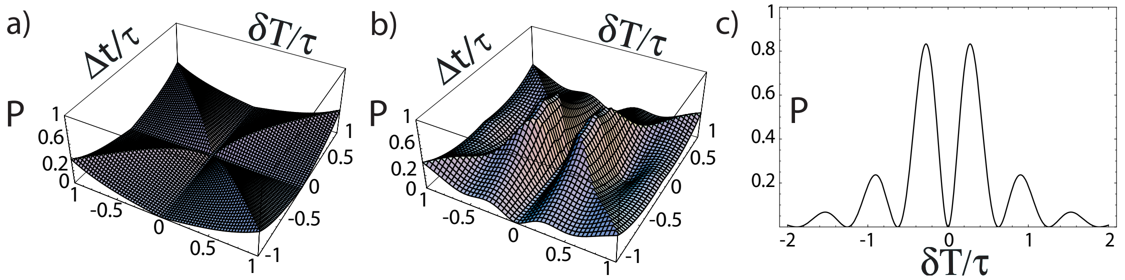

Figure 4.7: Graphs of the coincidence probability P_{HH,VV,Ψ^+} for a $|HH\rangle, |VV\rangle$ and a $|\Psi^+\rangle$-state having passed a beamsplitter with $x = y = 0.5$. The photons durations are the same $\tau' = \tau$. The creation time delay is $\triangle t = 0$, the detector resolution is $T_d = 1$. In a) the frequency difference is $\triangle\omega = 0$, in b) $\triangle\omega = 10/\tau$. c) shows a cut through the graph in b) along the δT-axis at $\triangle t = 0$.

and the photon-shape of eqn. 4.34 gives, because of the Θ-function in $\chi(t)$, eight functions defined on eight intervals in the $\triangle t$–δT-plane. Together they form one continuous function. The functions of the joint detection probability for the same initial states as above are described in Appendix A.3.5. The functions simplify when we assume that the photon duration is the same for both photons what should be the case in our experiments. In this case, all eight functions can be summarized into one function and we get:

$$\begin{aligned} P_{HH} &= \frac{T_d}{\tau}\Big[x^2 e^{-\frac{2}{\tau}|\triangle t+\delta T|} + (x-1)^2 e^{-\frac{2}{\tau}|\triangle t-\delta T|} \\ &\quad +2x(x-1)\cos(\triangle\omega\delta T)e^{-\frac{2}{\tau}(|\triangle t|+|\delta T|)}\Big] \qquad (4.40) \\ P_{\psi^\pm} &= \frac{T_d}{\tau}\Big[xy e^{-\frac{2}{\tau}|\triangle t+\delta T|} + (1-x)(1-y) e^{-\frac{2}{\tau}|\triangle t-\delta T|} \\ &\quad \mp 2\sqrt{xy(1-x)(1-y)}\,\cos(\triangle\omega\delta T)e^{-\frac{2}{\tau}(|\triangle t|+|\delta T|)}\Big] \qquad (4.41) \end{aligned}$$

P_{VV} is the same as P_{HH} with all x replaced by y.

Looking at the above two equations and the figs. 4.7 and 4.8 we see that the coincidence probability oscillates, if the photons have different frequencies. This oscillation of the joint measurement probability is a feature only arising by the ability of the detectors to resolve the photon detection within the photon durations.

A heuristic, intuitive interpretation is the following:

Suppose the photons have different frequency and one of them is detected earlier than the other one. Since the detectors have a better time resolution than the photon duration they can't resolve the frequency of the detected photon, thus the remaining photon is in a coherent superposition of the two frequency states. The time-evolution of this superposition is, as in classical interference, an oscillation between both spatial output modes of the beamsplitter. Depending on the time delay the photon is in mode one or in mode

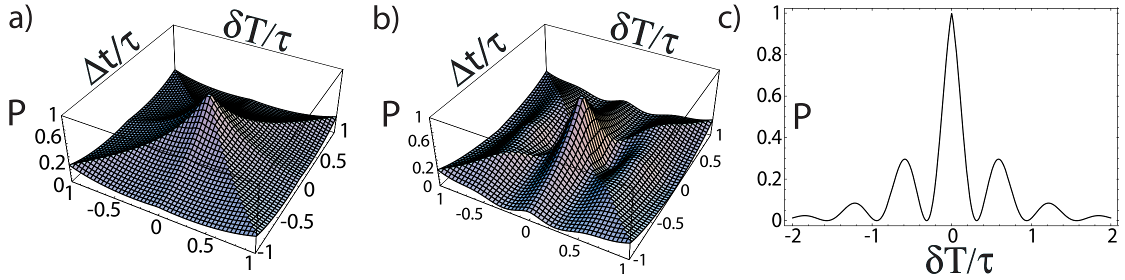

Figure 4.8: Graphs of the coincidence probability P_{Ψ^-} for a $|\Psi^-\rangle$-state having passed a beamsplitter with $x = y = 0.5$. The photons durations are the same $\tau' = \tau$. The creation time delay is $\triangle t = 0$, the detector resolution is $T_d = 1$. In a) the frequency difference is $\triangle\omega = 0$, in b)$\triangle\omega = 10/\tau$. c) shows a cut through the graph in b) along the δT-axis at $\triangle t = 0$.

VARIABLE	DESCRIPTION
τ	photon duration
Δt	creation (arrival) time difference of the two photons.
δT	detection time difference of the two photons
ΔT	time window around 0, on which we later on restrict our measurement
$\Delta\omega$	difference of the central frequencies of the photons
T_d	time resolution of the detectors

Figure 4.9: Table of the different variables used to describe the time-resolved two photon interference

two, interfering constructively or destructively with respect to the first detection event. If the polarizations are different no such effect occurs since for orthogonal polarizations no interference occurs. That is why the interference only occurs for identically polarized photons or the $|\Psi^{\pm}\rangle$-states, entangling the two photons. The phase with which the second photon starts its time evolution is given by the relative phase of the superposition.

4.2.4 Entanglement swapping with two entangled atom-photon pairs

One of the next experiments to be done is the entanglement swapping with two entangled atom-photon pairs to generate an entangled atom-atom pair. Therefore a second, improved setup is being set up to generate the second atom-photon pair. The two photons are to be overlapped at a fiber beamsplitter, performing the Bell-state measurement. For the realization of entanglement swapping between two ^{87}Rb atoms and of quantum teleportation of a photon onto a single ^{87}Rb atom we exploit the time-resolved two-photon interference described above to resolve one of the four Bell-states. In the case of the fiber

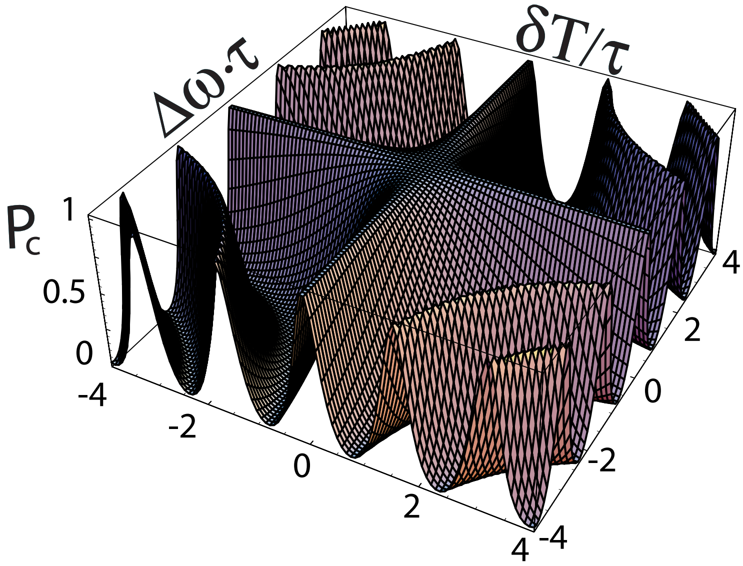

Figure 4.10: Graph of the conditional probability P_c of having projected into a $|\Psi^-\rangle$ state after a coincidence detection for varied δT and $\triangle\omega$ when using a 50 : 50 beamsplitter.

beamsplitter this is the $|\Psi^-\rangle$ state, as this is the only one resulting in a coincident detection event at both detectors. But since this is only true for ideal conditions, we are interested in the probability of projecting the photons in the $|\Psi^-\rangle$-state, when a coincidence was detected. This is important because it gives an upper bound to the fidelity of the entanglement/teleportation scheme. Assuming the photon durations are the same ($\tau = \tau'$)) and that the basis-states are uniformly distributed, the probability to have a coincidence in both detectors is

$$P = \sum_{i \in \{HH, VV, \Psi^\pm\}} P_i, \tag{4.42}$$

where the probabilities P_i are defined in eqns. [4.40] and [4.41]. The probability that this coincidence came from a projection onto a $|\Psi^-\rangle$-state is

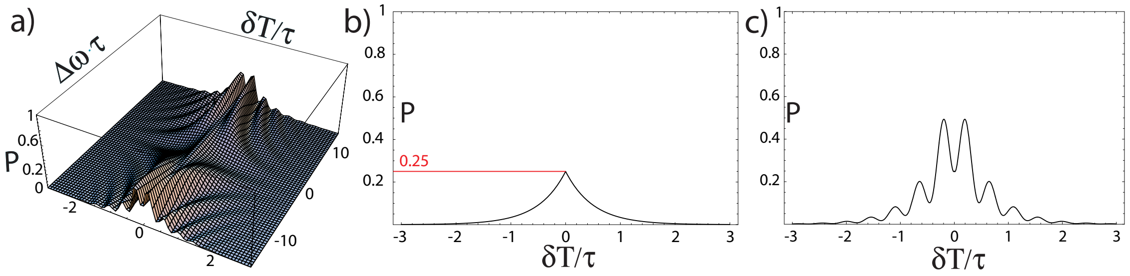

Figure 4.11: a) Graph of the probability P of eqn 4.42to have a coincidence with uniformly distributed polarization-states for a 50 : 50-beamsplitter. b) shows a cut along the $\triangle\omega$-axis at $\triangle\omega = 0$, c) shows cut at $\triangle\omega = 14/\tau$.

$$\begin{aligned}
P_{c,\Psi^-} &= \frac{P_{\Psi^-}}{P} \\
&= \frac{1}{4}\Big[xye^{-\frac{2}{\tau}|\triangle t+\delta T|} + (1-x)(1-y)e^{-\frac{2}{\tau}|\triangle t-\delta T|} \\
&\quad +2\sqrt{xy(1-x)(1-y)}\,\cos(\triangle\omega\delta T)e^{-\frac{2}{\tau}(|\triangle t|+|\delta T|)}\Big] \\
&\quad \Big[(x+y)^2e^{-\frac{2}{\tau}|\triangle t+\delta T|} + (x+y-2)^2e^{-\frac{2}{\tau}|\triangle t-\delta T|} \\
&\quad +2(x(x-1)+y(y-1))\cos(\triangle\omega\delta T)e^{-\frac{2}{\tau}(|\triangle t|+|\delta T|)}\Big]^{-1}
\end{aligned} \tag{4.43}$$

The equation simplifies if $\triangle t = 0$, what we will assume, since in the upcoming experiment the arrival time can be controlled to a good degree. In this way we obtain:

$$P_{c,\Psi^-}(\delta T, \triangle\omega) = \frac{1}{2}\frac{1+2xy-x-y+2\sqrt{xy(1-x)(1-y)}\cos(\triangle\omega\delta T)}{x^2+y^2+2xy-2x-2y+2+(x(x-1)+y(y-1))\cos(\triangle\omega\delta T)} \tag{4.44}$$

As you can see in fig. 4.10 the probability P_{c,Ψ^-} shows oscillatory behavior, when one varies δT or $\Delta\omega$. This seems irritating but we have to consider that the probability for a coincidence event converges to 0 for $|\delta T| \to \infty$ (see fig. 4.11).

The photons generated by spontaneous decay have a normalized Gaussian frequency distribution around the center frequency ω_0. This is because the trap induces lightshifts with a frequency, whose energy corresponds to the thermic energy of the trap [14]. Assuming that both traps have the same depth and that the photons have the same central frequency, the frequency difference is given again by a normalized Gaussian centered around 0:

$$p(\triangle\omega) = \frac{1}{\sqrt{2\pi}\sigma}e^{-\frac{(\triangle\omega)^2}{2\sigma^2}} \tag{4.45}$$

As we are interested in the conditional probability that the atoms were projected into a $|\Psi^-\rangle$-state after a coincidence detection, we weight $P_{c,\Psi^-}(\delta T, \triangle\omega)$ with the above distribution $p(\triangle\omega)$ and integrate over the frequency difference. The standard deviation σ is given by the full width at half maximum (FWHM) of the frequency distribution that we calculate out of the trap depth. In this way we obtain:

$$P_{c,\Psi^-}(\delta T) = \frac{1}{\sqrt{2\pi}\sigma} \int d(\triangle\omega)\ P_{c,\Psi^-}(\delta T, \triangle\omega) p(\triangle\omega) \tag{4.46}$$

In the real experiment the detection time difference can not be arbitrarily long. Via postselection only coincidence events with a time difference smaller than a time window $\triangle T$ will contribute ($|\delta T| < \triangle T/2$). For our purpose it is necessary to know how the conditional probability to project the atoms onto a $|\Psi^-\rangle$ depends on $\triangle T$, since we have to choose the size of this time window. This probability $\mathbf{P}_{c,\Psi^-}(\triangle T)$ can be calculated from $P_{c,\Psi^-}(\delta T)$ weighted with the probability distribution $p(\delta T)$ of the detection time delay. The shape of $p(\delta T)$ follows from the fact, that the photons arrive independently:

$$p(\delta T) = \int dt\ |\chi(t)|^2 |\chi'(t + \delta T)|^2 \tag{4.47}$$

We use the squared absolute values because we are interested in probabilities. For the probability of a projection into $|\Psi^-\rangle$ after a coincidence detection within ΔT follows:

$$\mathbf{P}_{c,\Psi^-}(\triangle T) = \frac{\int_{-\triangle T/2}^{\triangle T/2} d(\delta T)\ P_{c,\Psi^-}(\delta T) p(\delta T)}{\int_{-\triangle T/2}^{\triangle T/2} d(\delta T) p(\delta T)} \tag{4.48}$$

Using the photon shape from eqn. [4.34], equal arrival time at the beamsplitter and equal photon durations ($\tau = \tau'$), we get:

$$p(\delta T) = \frac{1}{\tau} e^{-2\frac{|\delta T|}{\tau}} \tag{4.49}$$

Putting everything together, the following expression gives $P_{c,\Psi^-}(\triangle T)$:

$$\mathbf{P}_{c,\Psi^-}(\triangle T) = \frac{1}{\sqrt{2\pi}\sigma} \frac{\int_{-\triangle T/2}^{\triangle T/2} d(\delta T) \int d(\triangle\omega)\ P_{c,\Psi^-}(\triangle T, \triangle\omega) e^{-2\frac{|\delta T|}{\tau} - \frac{(\triangle\omega)^2}{2\sigma^2}}}{\int_{-\triangle T/2}^{\triangle T/2} d(\delta T) e^{-2\frac{|\delta T|}{\tau}}} \tag{4.50}$$

From the preceding calculations we are now able to give an upper bound for the fidelity of the entangled atom-pair. Using the measured transmission and reflection coefficients of the beamsplitter and the known frequency distribution of the photons we can guess the probability of projecting the two photons onto the Ψ^- state. This allows us to estimate the dependency of the probability from the detection window. The FWHM of the frequency distribution for one photon is 8.8 MHz, the decay-time of ^{87}Rb is $\Gamma = 26.2$ ns[14], it

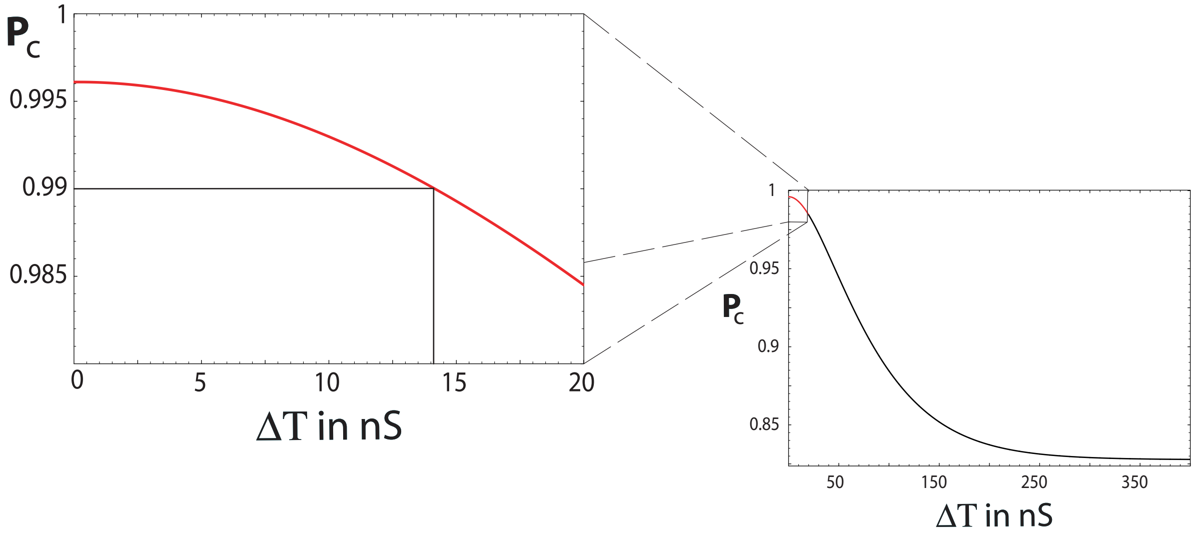

Figure 4.12: Graph of the conditional probability $\mathbf{P}_c$ of projecting into the $|\Psi^-\rangle$-state after the detection of a coincidence event in the time window ΔT. One observes that $\triangle T$ has to be smaller than 14 ns to get a probability bigger than 99%.

follows for the photon duration $\tau = 2\Gamma = 52.4$ ns. The fiber beamsplitter has the following specifications, where we chose the worst measured values for x and y. The measurement of the splitting ratios can't tell which polarization the measured splitting ratio can be associated to, since the fiber beamsplitter has been broke down and set up newly, whereby the adjustment is not necessarily the same anymore. Anyway that is no issue since the function $P_{c,\Psi^-}(\triangle T)$ is symmetric in x and y. We get $x = 0.5221$ and $y = 0.4779$ [42].
Fig. 4.12 shows the numerical solution of eqn. 4.50 with above parameters. As expected one gets the hightest fidelity for $\triangle T = 0$. The maximum is defined by the quality of the beamsplitter, in our case the maximal fidelity is

$$F_{max} = 0.9961 \tag{4.51}$$

We want to achieve a fidelity of about 99%, which requires a temporal-window of $\triangle T = 14$ nS.

4.3 Summary

This chapter gave an overview of the description of single photons created by spontaneous decay and their influence on two photon interference. The detection processes for single and two photon events were analyzed for two different types of detectors. One that can resolve the photon duration and one that can't. We analyzed the two-photon interference at a beamsplitter by using our previous results. The fundamental difference for the two processes is that in the case of time-resolved measurement the frequency difference is, in contrast to the other case, making the coincidence-probability oscillating for growing time-difference between the detection-events of the detectors, whereas for measurements without time-resolution the visibility of the interference effects is lowered. At the end an estimation of the expected results for the upcoming measurements was performed, bases on the measured and calculated experimental parameters. From this we obtain a maximal possible fidelity of $F_{max} = 0.9961$ for the entanglement swapping. Supposing that the arrival time of the photons is the same, the time window that allows fidelities bigger than 0.99 was estimated to be 14 ns.

Chapter 5

Summary and outlook

This thesis describes the generation of long distance entanglement between matter and light, namely a single ^{87}Rb atom and a photon passing a distance of 300 m. We verified the entanglement by performing measurements on the atom-photon pair and observed strong correlations between the internal atomic state and the polarization of the photon with a mean visibility of $V_{av} = 0.75$.

To achieve these results we implemented a 300 m long single mode fiber into the previous setup. To correct random rotations of the polarization state of the photon travelling through the fiber and thus the loss of the entanglement between the atom and the photon, the birefringence of the fiber was actively stabilized by a polarization control setup. This setup works by sending well defined input polarizations through the fiber, analyzing the output states very accurately (with an error less than 0.13%) and then minimizing the deviation of the input and output polarization with a fiber based polarization controller. Repeating this process up to 100 times we obtain an overlap between input and output polarization better than 99.8%. Thus the setup is capable of maintaining the polarization of light, passing a long optical fiber very accurately. The distribution of entanglement over long distances can thereby be performed without additional losses of coherence.

The setup presented in this work is a prototype which already shows a very high degree of reliability. Possible improvements should mainly address the speed of the polarization compensation. Due to limitations in the interactions between the CPU and the shutters the repetition frequency of one iteration is approximately 1.49 Hz. By implementing the algorithm electronically and using AOMs instead of shutters for faster switching, this frequency could be increased up to a factor of approximately 1000 , i.e. to 1 kHz, limited by the rise time of the photodiodes, used for the polarization analysis. This would allow online stabilization of the polarization by using short, well defined time intervals of several milliseconds . In this way it would be possible to compensate even fast polarization fluctuations caused by vibrations and the possible distances that can be stabilized could be increased to several 10 km.

With these improvements the polarization control will be the ideal tool to prevent errors for future applications in quantum computation and information like e.g. the quantum repeater, which rely on the transport of quantum information over long distances.

The future goal of this setup is to enable the generation of entanglement between two distant atoms using the entanglement swapping protocol. Therefore we exploit two photon interference on a beamsplitter by selecting the events having a coincident detection in both out putports of the beamsplitter. Therefore in the last part of this thesis the two photon interference effects on a fiber beamsplitter were considered theoretically. This allowed to give an upper bound for the visibility of the correlations of the entangled atom-atom pairs, depending on the arrival time of the photons, their frequency distribution and the properties of the used beamsplitter. It was shown that using a time-resolved detection with a coincidence time-window of 14 ns leads to a fidelity of 99% for the entanglement swapping protocol.

Thus it is possible to obtain a high degree of entanglement between two atoms which are separated by approximately 300 m.

A sub-microsecond readout of the internal atomic states using state selective ionization from which we expect to provide a detection efficiency of 96% [43] will close the detection loophole and together with the spatial separation of both setups the locality loophole will be closed. These are the final steps towards the loophole free test of Bells inequaltiy using entangled atoms.

Appendix A

Appendix

A.1 Level scheme of ^{87}Rb

A.2 Second quantization and its description in the time domain

A.2.1 Creation-/annihilation-operators and Fock-states

Lightfields in a cavity with length L can be described in the picture of an harmonic oscillator [44]. This is in particular true in quantum mechanics. Since the photons we will consider have passed a single-mode fiber, they are in a Gaussian transverse mode and we can ignore other transverse modes. In this case the corresponding Hamiltonian reads

$$\hat{H} = \hbar \sum_j \omega_j \left(\hat{a}_j^\dagger \hat{a}_j + \frac{1}{2} \right), \tag{A.1}$$

where ω_j gives the allowed frequency modes of the electric field that are separated by $\triangle\omega = \frac{2\pi c}{L}$, $\hat{a}_j$ and $\hat{a}_j^\dagger$ are the annihilation- and creation-operators for a photon in mode j respectively. They fulfill the following commutation relations:

$$\left[\hat{a}_i, \hat{a}_j^\dagger\right] = \delta_{ij} \tag{A.2}$$

$$\left[\hat{a}_i^{(\dagger)}, \hat{a}_j^{(\dagger)}\right] = 0 \tag{A.3}$$

A photon with energy $E_j = \hbar\omega_j$ can be described like an eigenmode of the Hamiltonian

$$\hat{H}_j = \hbar\omega_j \left(\hat{a}_j^\dagger \hat{a}_j + \frac{1}{2} \right). \tag{A.4}$$

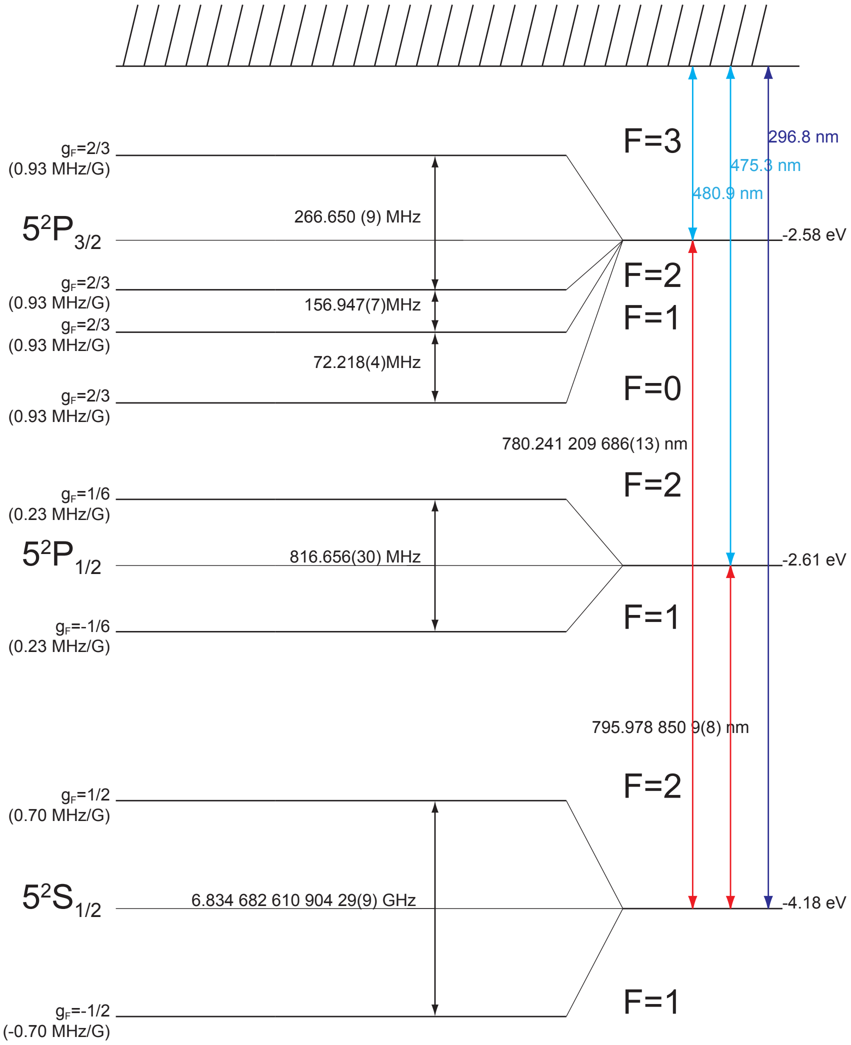

Figure A.1: Level scheme of ^{87}Rb (not to scale)

The energy eigenstates of $\hat{H}_j$ are

$$\left|n\right\rangle_j = \frac{(\hat{a}_j^\dagger)^n}{\sqrt{n!}} \left|0\right\rangle , \tag{A.5}$$

the so-called Fock- or number-states which form a complete set:

$$\sum_{n=0}^{\infty} \left|n\right\rangle \left\langle n\right| = 1 \tag{A.6}$$

Their corresponding eigenvalues are

$$E_{j,n} = (n + \frac{1}{2})\hbar\omega_j. \tag{A.7}$$

That makes it reasonable to identify the number of photons in the mode j with $|n\rangle_j$. The effect of $\hat{a}_j^\dagger$ ($\hat{a}_j$) is to create (destroy) one photon in mode j:

$$\hat{a}_j^\dagger |n\rangle_j = \sqrt{n+1}\,|n+1\rangle_j \qquad (\hat{a}_j |n\rangle_j = \sqrt{n}\,|n-1\rangle_j) \tag{A.8}$$

Looking at the Hamiltonian $\hat{H}$ in eqn. [A.1] one sees that the state-vectors are linear superpositions of the direct product of the single $\hat{H}_j$'s eigenstates states $|n_{j_1}, n_{j_2}, ..., n_{j_l}, ...\rangle := |n_{j_1}\rangle |n_{j_2}\rangle ... |n_{j_l}\rangle ...$:

$$|\psi\rangle = \sum_{n_{j_1}} \sum_{n_{j_2}} ... \sum_{n_{j_l}} ... c_{n_{j_l} n_{j_2} ... n_{j_l} ...} |n_{j_1}, n_{j_2}, ..., n_{j_l}, ...\rangle \tag{A.9}$$

If the polarization is taken into account too and we use horizontal and vertical polarization as basis $\hat{a}_j^{(\dagger)}$ becomes $\hat{a}_{j,H/V}^{(\dagger)}$ fulfilling the extended commutation relations ($n, m \in \{H, V\}$)

$$\begin{aligned} \left[\hat{a}_{i,n}, \hat{a}_{j,m}^\dagger\right] &= \delta_{ij}\delta_{nm} && \text{(A.10)} \\ \left[\hat{a}_{i,n}^{(\dagger)}, \hat{a}_{j,m}^{(\dagger)}\right] &= 0 && \text{(A.11)} \end{aligned}$$

A.2.2 Frequency dependent annihilation-/creation-operators

The creation-/annihilation-operators we have considered so far are implicitly frequency-dependent because they each just act on photons of the corresponding frequency ω_j. Considering the limit of the cavity being infinite ($L \to \infty$) all frequencies are allowed and $\hat{a}_{j,H/V}^{(\dagger)}$ becomes $\sqrt{\triangle\omega}\; a_{H/V}^{(\dagger)}(\omega)$, destroying (creating) a infinite expanded monochromatic wave with frequency $\omega/2\pi$ propagating along the z-axis [45]. The infinite size of the wave is a direct consequence of the Heisenberg energy-time uncertainty principle. The Kronecker and Dirac δ-functions are related by

$$\delta_{ij} \to \triangle\omega\delta(\omega - \omega'), \tag{A.12}$$

and the commutation relation [A.11] is converted to

$$\left[\hat{a}_n(\omega), \hat{a}_m^\dagger(\omega')\right] = \delta_{nm}\delta(\omega - \omega'), \quad (n, m \in \{H, V\}) \tag{A.13}$$

And the sum over the discrete frequencies becomes an integral by the following rule

$$\sum_j \to \frac{1}{\triangle\omega} \int d\omega \tag{A.14}$$

The problem when dealing with this form of modes is that they are not countable. So eigenstates of the Hamiltonian can not be written as simple product states of the eigenstates of single modes. It is possible to define a noncontinuous set of modes and it is useful since the notation of eqn. [A.9] can be used again to describe the states of the system. If we can construct a complete orthonormal set of functions $\phi_i(\omega)$, that not needs necessarily to be a set of eigenmodes, we can use these functions to define a set of countable modes with the annihilation operators

$$\hat{c}_{j,H/V} = \int d\omega\, \phi_j^*(\omega)\hat{a}_{H/V}(\omega) \tag{A.15}$$

the creation operators $\hat{c}^\dagger_{j,H/V}$ are the transposed of $\hat{c}_{j,H/V}$. The inverse transformation yields

$$\hat{a}_{H/V}(\omega) = \sum_j \phi_j(\omega)\hat{c}_{j,H/V} \tag{A.16}$$

A.2.3 From frequency dependence to the time domain

The transformation into the time-space domain is straight forward as long as the bandwidth κ of the photons fulfills $\kappa << \omega_0$ [45], where ω_0 is the central frequency of the photons. This is true in our case because the photons emitted from our source are very narrow-band (smaller $10MHz$) as the trapped atom is ultra cold and has very low kinetic energy. The transformation is a simple Fourier transformation. With $q := t - z/c$ follows

$$\begin{aligned}
\chi_i(q) &= (2\pi)^{-1/2}\int d\omega\, \phi_i(\omega)\; exp(-i\omega q) && \text{(A.17)}\\
\hat{a}_{H/V}(q) &= (2\pi)^{-1/2}\int d\omega\, \hat{a}_{H/V}(\omega)\; exp(-i\omega q) && \text{(A.18)}\\
\hat{c}_{j,H/V} &= \int dq\; \chi_i^*(q)\; \hat{a}_{H/V}(q) && \text{(A.19)}
\end{aligned}$$

We will just observe photons at a certain point where we choose $z = 0$. Using this definition we can replace q by t, what is done from now on. The new operators obey the following commutation relations

$$\begin{aligned}
\left[\hat{a}_n(t), \hat{a}^\dagger_m(t')\right] &= \delta_{nm}\delta(t-t') && \text{(A.20)}\\
\left[\hat{a}_n(t), \hat{c}^\dagger_{j,m}\right] &= \delta_{nm}\chi_j(t) && \text{(A.21)}
\end{aligned}$$

A.3 description of a beamsplitter

In this section the theoretical description of a beamsplitter is developed. We will see that there are basically two different kinds of beamsplitters that have a physical meaning.

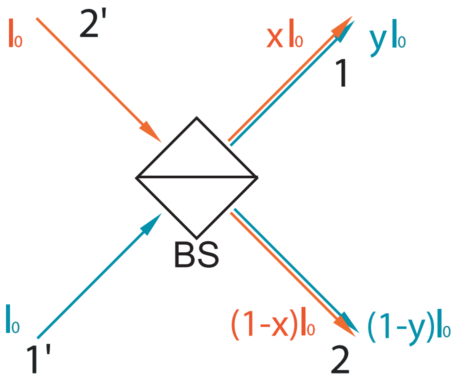

Figure A.2: Scheme of two lightfields on a beamsplitter, arriving at different spatial modes.

From an experimental point of view they can also quite easily be transformed into each other, but they have a significant difference, namely that they produce different interference. One makes the $|\Psi^+\rangle$-state having a coincidence at both detectors, while the other one splits up an incident $|\Psi^-\rangle$-state. All commercial available free space beamsplitters we have analyzed so far split up a $|\Psi^+\rangle$-state, what is the reason for us to consider this case (but that can easily be changed by using an additional $\lambda/2$-wave plate at 0^o in one of the inputs). A fiber beamsplitter has the advantage, that its behavior can be manipulated by changing the birefringence of the incoming optical fibers.

A.3.1 Basic requirements for a beamsplitter

We assume that the beamsplitter to describe meets some requirements:

- No absorption, the beamsplitter is a unitary transformation, i.e. $\hat{BS}^\dagger \hat{BS} = \mathbb{1}$
- The eigenbasis of the beamsplitter is the H/V-basis. That follows by the observation that a real, free-space beamsplitter maintains $H-$ and $V-$polarized light, except from a phase, observable with ±-polarized light.

A general beamsplitter meeting the above conditions can be described by the following transformations, where the subscripts denote in which spatial mode the photon is in (see fig. A.2):

$$\hat{c}_{\chi,H,1'} \overset{\hat{BS}}{\to} \sqrt{x}\; e^{i\varphi_1}\hat{c}_{\chi,H,1} + \sqrt{1-x}\; e^{i\varphi_2}\hat{c}_{\chi,H,2} \tag{A.22}$$

$$\hat{c}_{\chi,H,2'} \overset{\hat{BS}}{\to} \sqrt{1-x}\; e^{i\varphi_3}\hat{c}_{\chi,H,1} + \sqrt{x}\; e^{i\varphi_4}\hat{c}_{\chi,H,2} \tag{A.23}$$

$$\hat{c}_{\chi,V,1'} \overset{\hat{BS}}{\to} \sqrt{y}\; e^{i\varphi_5}\hat{c}_{\chi,V,1} + \sqrt{1-y}\; e^{i\varphi_6}\hat{c}_{\chi,V,2} \tag{A.24}$$

$$\hat{c}_{\chi,V,2'} \overset{\hat{BS}}{\to} \sqrt{1-y}\; e^{i\varphi_7}\hat{c}_{\chi,V,1} + \sqrt{y}\; e^{i\varphi_8}\hat{c}_{\chi,V,2} \tag{A.25}$$

The value x (y) is the transmittance of the beamsplitter for $|H\rangle$- ($|V\rangle$-) polarized light. The square roots arise from the fact that we are dealing with amplitudes that have to be normalized and not with lightfields. We need to know the different phases φ_i, that light can gain when passing the beamsplitter to get the full information of the beamsplitter. This will be done in the following two sections for a free space beamsplitter and a fiber beamsplitter, respectively. Some general properties, that are valid for all beamsplitters, are, that the phases φ_1 and φ_5 can be chosen to be zero, since they only give a global, not measurable phase.

A.3.2 Beamsplitter splitting up $|\Psi^+\rangle$

The description of a beamsplitter splitting up $|\Psi^+\rangle$ is straight forward since we do not consider any degrees of freedom except the ability to compensate phases, what simulates a commercial available beamsplitter cube. This compensation would then be done by shining $|+\rangle$-polarized light onto the beamsplitter and looking for this polarization to be maintained or at least being transformed into $|-\rangle$-polarization (i.e. a phaseshift of π for H- or V-polarization).

This π-phaseshift is indeed the case for the reflected part of the beam for both input modes. The beamsplitters we tested all transformed $|+\rangle$-polarized light into $|-\rangle$-polarized for the reflected arm. Taking this into account, using the fact that all additional phases have no effects since they can easily be eliminated. This, together with the unitarity lead to the following transformations:

$$\hat{c}_{\chi,H,1'} \overset{\hat{BS}}{\rightarrow} \sqrt{x}\,\hat{c}_{\chi,H,1} + \sqrt{1-x}\,\hat{c}_{\chi,H,2} \tag{A.26}$$

$$\hat{c}_{\chi,H,2'} \overset{\hat{BS}}{\rightarrow} -\sqrt{1-x}\,\hat{c}_{\chi,H,1} + \sqrt{x}\,\hat{c}_{\chi,H,2} \tag{A.27}$$

$$\hat{c}_{\chi,V,1'} \overset{\hat{BS}}{\rightarrow} \sqrt{y}\,\hat{c}_{\chi,V,1} - \sqrt{1-y}\,\hat{c}_{\chi,V,2} \tag{A.28}$$

$$\hat{c}_{\chi,V,2'} \overset{\hat{BS}}{\rightarrow} \sqrt{1-y}\,\hat{c}_{\chi,V,1} + \sqrt{y}\,\hat{c}_{\chi,V,2} \tag{A.29}$$

What at the first look seem curious is the fact, that using such a beamsplitter makes the Ψ^+-state having a coincidence at both detectors instead of the $|\Psi^-\rangle$-state. One can easily observe this behavior by using above transformations onto these states. This is interesting because it is the $|\Psi^-\rangle$-state from which the coincidence is expected as it is a singlet-state and by this asymmetric (One can heuristically argue that the $|\Psi^-\rangle$-state is fermionic and thus both particles do not end up in the same spatial mode, whereas the remaining three Bell states follow bosonic behavior, what means that both particles ”choose” the same spatial mode). To understand this feature we must look at the transformation of the $|\Psi^\pm\rangle$-states. Because of the phase shift they change roles $|\Psi^\pm\rangle \rightarrow |\Psi^\mp\rangle$ behind the beamsplitter, what leads to their exchanged behavior.

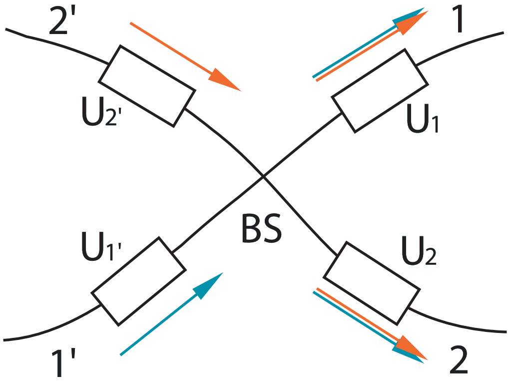

Figure A.3: Scheme of two lightfields passing a fiber beamsplitter, the transformations of the polarizations caused by birefringence in the fiber are symbolized as unitary transformations U_i.

A.3.3 Fiber beamsplitter

When considering a fiber beamsplitter, we will consider the beamsplitter itself and the fibers as one system. The beamsplitter itself is supposed to split up the incoming light according to its transmittances x and y, without giving additional phases to any polarization. All additional transformations of the light occur due to the unitary transformations of the fiber. The splitting of the transformations is justified, from the fact, that the we can only perform tests on the whole system, that is fully described by above assumptions. For simplicity we assume the eigenpolarizations to be $|H\rangle$ and $|V\rangle$, what can easily be adjusted. The beamsplitter is than fully described by eqns. A.22-A.25.

Practically, the polarizations in a fiber is manipulated by changing its birefringence. The manipulations in the fiber are represented by changes of the unitary transformations U_i. Together with above assumptions we overcome the problem, that it is impossible to measure which polarization arrives at the beamsplitter by observing one fact: To predict how the two photons interfere one needs to know the input two-photon state and make sure that the photons arrive at the beamsplitter having passed the same unitary rotations (i.e. $U_{1'} = U_{2'}$) , what does not mean that the birefringence of both input fibers have to be the same, they just should lead to the same result. This is sufficient if the beamsplitter makes the $|\Psi^-\rangle$-state having a coincidence since its representation is independent of the choice of bases and the other three Bell-states behave in the same way anyway.

This can be proven easily by looking at the transformation of the input polarization by following equations, that follow from the assumption $U_{1'} = U_{2'}$:

$$\begin{aligned}
\hat{c}_{\chi,H,1'} &\overset{\hat{BS}}{\rightarrow} \sqrt{x}\,\hat{c}_{\chi,H,1} + \sqrt{1-x}\,e^{i\varphi_2}\hat{c}_{\chi,H,2} && (A.30)\\
\hat{c}_{\chi,H,2'} &\overset{\hat{BS}}{\rightarrow} \sqrt{1-x}\,e^{i\varphi_3}\hat{c}_{\chi,H,1} + \sqrt{x}\,e^{i\varphi_4}\hat{c}_{\chi,H,2} && (A.31)\\
\hat{c}_{\chi,V,1'} &\overset{\hat{BS}}{\rightarrow} \sqrt{y}\,\hat{c}_{\chi,V,1} + \sqrt{1-y}\,e^{i\varphi_2}\hat{c}_{\chi,V,2} && (A.32)\\
\hat{c}_{\chi,V,2'} &\overset{\hat{BS}}{\rightarrow} \sqrt{1-y}\,e^{i\varphi_3}\hat{c}_{\chi,V,1} + \sqrt{y}\,e^{i\varphi_4}\hat{c}_{\chi,V,2}\ , && (A.33)
\end{aligned}$$

The three phases depend from each other because of unitarity:

$$\varphi_2 = \pi - \varphi_3 - \varphi_4 \tag{A.34}$$

A.3.4 Electric field operators

The operator describing the electric field is $\hat{E}(\mathbf{r},t) = \hat{E}^{+}(\mathbf{r},t) + \hat{E}^{-}(\mathbf{r},t)$. The parts of the electric field operator $\hat{E}^{+}(\mathbf{r},t)$ and $\hat{E}^{-}(\mathbf{r},t)$ are directly connected with the creation/annihilation of a photon [45, 44]. The quantization of the electric field gives

$$\hat{E}^{+}(z,t) \;=\; i\sum_{s=1,2}\int_0^{\infty} d\omega\,\left(\frac{\hbar\omega}{4\pi\epsilon_0 cA}\right)^{1/2}\hat{a}_s(\omega)\,\epsilon_s\,e^{-i\omega(t-z/c)}, \tag{A.35}$$

where A is the quantization cross section. The sum goes over two arbitrary, orthogonal polarizations, given by the complex vector ϵ_s. The frequency dependency can be simplified if only photons from narrow-band sources are concerned ($\kappa << \omega_0$), because ω in the squareroot can be replaced by ω_0. The integral range can be extended from 0 to $-\infty$ without significant errors [45]. Thus the field operator gets the following shape:

$$\hat{E}^{+}(z,t) \;=\; i\left(\frac{\hbar\omega_0}{4\pi\epsilon_0 cA}\right)^{1/2}\sum_s \epsilon_s\int_{-\infty}^{\infty} d\omega\;\hat{a}_s(\omega)\,e^{-i\omega(t-z/c)}. \tag{A.36}$$

A.3.5 Full solution of two photon interference with time-resolution

In section 4.2.2, the solution for two photon interference with time resolution is presented for photons with same duration $\tau = \tau'$. The solution of the integral 4.32 for the $G^{(2)}$-function 4.30and the photon-shape of eqn. 4.34 gives, because of the Θ-function in the photon-state function eight functions defined on eight intervals in the $\triangle t - \delta T$-plane, when we are considering photons with different durations ($\tau \neq \tau'$). The solutions read, considering a beamsplitter, that splits up $|\Psi^{-}\rangle$ for the state $|HH\rangle$ with $P_{k,HH}(\delta T, \triangle t, \tau, \tau', \triangle\omega) =: P_{k,HH}$ (the same is true for $|VV\rangle$, just use VV instead of HH):

$$\begin{aligned} P_{1,HH} &= \frac{2T_A}{\tau+\tau'}\Big[x^2 e^{+2(\triangle t+\delta T)/\tau} + (x-1)^2 e^{-2(\delta T-\triangle t)/\tau} \\ &\quad +2x(x-1)cos(\triangle\omega\delta T)e^{+2\triangle t/\tau-(\tau+\tau')(\delta T)/(\tau'\tau)}\Big], \\ \text{if} &\quad \delta T>0, \triangle t<0, \delta T<-\triangle t \end{aligned} \tag{A.37}$$

$$\begin{aligned} P_{2,HH} &= \frac{2T_A}{\tau+\tau'}\Big[x^2 e^{-2(\triangle t+\delta T)/\tau'} + (x-1)^2 e^{-2(\delta T-\triangle t)/\tau} \\ &\quad +2x(x-1)cos(\triangle\omega\delta T)e^{+2\triangle t/\tau-(\tau+\tau')(\delta T)/(\tau'\tau)}\Big], \\ \text{if} &\quad \delta T>0, \triangle t<0, \delta T>-\triangle t \end{aligned} \tag{A.38}$$

$$\begin{aligned} P_{3,HH} &= \frac{2T_A}{\tau+\tau'}\Big[x^2 e^{-2(\triangle t+\delta T)/\tau'} + (x-1)^2 e^{-2(\delta T-\triangle t)/\tau} \\ &\quad +2x(x-1)cos(\triangle\omega\delta T)e^{-2\triangle t/\tau-(\tau+\tau')(\delta T)/(\tau'\tau)}\Big], \\ \text{if} &\quad \delta T>0, \triangle t>0, \delta T>\triangle t \end{aligned} \tag{A.39}$$

$$\begin{aligned} P_{4,HH} &= \frac{2T_A}{\tau+\tau'}\Big[x^2 e^{-2(\triangle t+\delta T)/\tau'} + (x-1)^2 e^{-2(\triangle t-\delta T)/\tau'} \\ &\quad +2x(x-1)cos(\triangle\omega\delta T)e^{-2\triangle t/\tau-(\tau+\tau')(\delta T)/(\tau'\tau)}\Big], \\ \text{if} &\quad \delta T>0, \triangle t>0, \delta T<\triangle t \end{aligned} \tag{A.40}$$

$$\begin{aligned} P_{5,HH} &= \frac{2T_A}{\tau+\tau'}\Big[x^2 e^{-2(\triangle t+\delta T)/\tau'} + (x-1)^2 e^{-2(\triangle t-\delta T)/\tau'} \\ &\quad +2x(x-1)cos(\triangle\omega\delta T)e^{-2\triangle t/\tau+(\tau+\tau')(\delta T)/(\tau'\tau)}\Big], \\ \text{if} &\quad \delta T<0, \triangle t>0, \delta T>-\triangle t \end{aligned} \tag{A.41}$$

$$\begin{aligned} P_{6,HH} &= \frac{2T_A}{\tau+\tau'}\Big[x^2 e^{+2(\triangle t+\delta T)/\tau} + (x-1)^2 e^{-2(\triangle t-\delta T)/\tau'} \\ &\quad +2x(x-1)cos(\triangle\omega\delta T)e^{-2\triangle t/\tau+(\tau+\tau')(\delta T)/(\tau'\tau)}\Big], \\ \text{if} &\quad \delta T<0, \triangle t>0, \delta T<-\triangle t \end{aligned} \tag{A.42}$$

$$\begin{aligned} P_{7,HH} &= \frac{2T_A}{\tau+\tau'}\Big[x^2 e^{+2(\triangle t+\delta T)/\tau} + (x-1)^2 e^{-2(\triangle t-\delta T)/\tau'} \\ &\quad +2x(x-1)cos(\triangle\omega\delta T)e^{+2\triangle t/\tau+(\tau+\tau')(\delta T)/(\tau'\tau)}\Big], \\ \text{if} &\quad \delta T<0, \triangle t<0, \delta T<\triangle t \end{aligned} \tag{A.43}$$

$$\begin{aligned} P_{8,HH} &= \frac{2T_A}{\tau+\tau'}\Big[x^2 e^{+2(\triangle t+\delta T)/\tau} + (x-1)^2 e^{-2(\delta T-\triangle t)/\tau} \\ &\quad +2x(x-1)cos(\triangle\omega\delta T)e^{+2\triangle t/\tau+(\tau+\tau')(\delta T)/(\tau'\tau)}\Big], \\ \text{if} &\quad \delta T<0, \triangle t<0, \delta T>\triangle t \end{aligned} \tag{A.44}$$

These functions build one continuous function, that can not be further simplified. For $\tau' \rightarrow \tau$, these functions transform into the first function of eqn. 4.41.
The functions describing the interference of $|\Psi^{\pm}\rangle$ read:

$$\begin{aligned}
P_{1,\psi^{\pm}} &= \frac{2T_A}{\tau+\tau'}\Big[xye^{+2(\triangle t+\delta T)/\tau}+(1-x)(1-y)e^{-2(\delta T-\triangle t)/\tau} \\
&\quad \mp 2\sqrt{xy(1-x)(1-y)}\,cos(\triangle\omega\delta T)e^{+\frac{2\triangle t}{\tau}-\frac{(\tau+\tau')(\delta T)}{\tau'\tau}}\Big], \\
&\text{if} \quad \delta T>0, \triangle t<0, \delta T<-\triangle t
\end{aligned} \tag{A.45}$$

$$\begin{aligned}
P_{2,\psi^{\pm}} &= \frac{2T_A}{\tau+\tau'}\Big[xye^{-2(\triangle t+\delta T)/\tau'}+(1-x)(1-y)e^{-2(\delta T-\triangle t)/\tau} \\
&\quad \mp 2\sqrt{xy(1-x)(1-y)}\,cos(\triangle\omega\delta T)e^{+\frac{2\triangle t}{\tau}-\frac{(\tau+\tau')(\delta T)}{\tau'\tau}}\Big], \\
&\text{if} \quad \delta T>0, \triangle t<0, \delta T>-\triangle t
\end{aligned} \tag{A.46}$$

$$\begin{aligned}
P_{3,\psi^{\pm}} &= \frac{2T_A}{\tau+\tau'}\Big[xye^{-2(\triangle t+\delta T)/\tau'}+(1-x)(1-y)e^{-2(\delta T-\triangle t)/\tau} \\
&\quad \mp 2\sqrt{xy(1-x)(1-y)}\,cos(\triangle\omega\delta T)e^{-\frac{2\triangle t}{\tau}-\frac{(\tau+\tau')(\delta T)}{\tau'\tau}}\Big], \\
&\text{if} \quad \delta T>0, \triangle t>0, \delta T>\triangle t
\end{aligned} \tag{A.47}$$

$$\begin{aligned}
P_{4,\psi^{\pm}} &= \frac{2T_A}{\tau+\tau'}\Big[xye^{-2(\triangle t+\delta T)/\tau'}+(1-x)(1-y)e^{-2(\triangle t-\delta T)/\tau'} \\
&\quad \mp 2\sqrt{xy(1-x)(1-y)}\,cos(\triangle\omega\delta T)e^{-\frac{2\triangle t}{\tau}-\frac{(\tau+\tau')(\delta T)}{\tau'\tau}}\Big], \\
&\text{if} \quad \delta T>0, \triangle t>0, \delta T<\triangle t
\end{aligned} \tag{A.48}$$

$$\begin{aligned}
P_{5,\psi^{\pm}} &= \frac{2T_A}{\tau+\tau'}\Big[xye^{-2(\triangle t+\delta T)/\tau'}+(1-x)(1-y)e^{-2(\triangle t-\delta T)/\tau'} \\
&\quad \mp 2\sqrt{xy(1-x)(1-y)}\,cos(\triangle\omega\delta T)e^{-\frac{2\triangle t}{\tau}+\frac{(\tau+\tau')(\delta T)}{\tau'\tau}}\Big], \\
&\text{if} \quad \delta T<0, \triangle t>0, \delta T>-\triangle t
\end{aligned} \tag{A.49}$$

$$\begin{aligned}
P_{6,\psi^{\pm}} &= \frac{2T_A}{\tau+\tau'}\Big[xye^{+2(\triangle t+\delta T)/\tau}+(1-x)(1-y)e^{-2(\triangle t-\delta T)/\tau'} \\
&\quad \mp 2\sqrt{xy(1-x)(1-y)}\,cos(\triangle\omega\delta T)e^{-\frac{2\triangle t}{\tau}+\frac{(\tau+\tau')(\delta T)}{\tau'\tau}}\Big], \\
&\text{if} \quad \delta T<0, \triangle t>0, \delta T<-\triangle t
\end{aligned} \tag{A.50}$$

$$\begin{aligned}
P_{7,\psi^{\pm}} &= \frac{2T_A}{\tau+\tau'}\Big[xye^{+2(\triangle t+\delta T)/\tau}+(1-x)(1-y)e^{-2(\triangle t-\delta T)/\tau'} \\
&\quad \mp 2\sqrt{xy(1-x)(1-y)}\,cos(\triangle\omega\delta T)e^{+\frac{2\triangle t}{\tau}+\frac{\tau+\tau'(\delta T)}{(\tau'\tau)}}\Big], \\
&\text{if} \quad \delta T<0, \triangle t<0, \delta T<\triangle t
\end{aligned} \tag{A.51}$$

$$\begin{aligned}
P_{8,\psi^{\pm}} &= \frac{2T_A}{\tau+\tau'}\Big[xye^{+2(\triangle t+\delta T)/\tau}+(1-x)(1-y)e^{-2(\delta T-\triangle t)/\tau} \\
&\quad \mp 2\sqrt{xy(1-x)(1-y)}\,cos(\triangle\omega\delta T)e^{+\frac{2\triangle t}{\tau}+\frac{\tau+\tau'(\delta T)}{(\tau'\tau)}}\Big], \\
&\text{if} \quad \delta T<0, \triangle t<0, \delta T>\triangle t
\end{aligned} \tag{A.52}$$

Bibliography

[1] R. W. Clark. *Einstein: The Life and Times.* Avon, 1999.

[2] D Bohm. *Quantum Theory.* Prentice-Hall, Englewood Cliffs, New York, 1951.

[3] J. S. Bell. *Foundations of Quantum Mechanics.* Academic Press, New York, 1971.

[4] John F. Clauser, Michael A. Horne, Abner Shimony, and Richard A. Holt. Proposed experiment to test local hidden-variable theories. *Phys. Rev. Lett.*, 23(15):880–884, October 1969.

[5] Eugene P. Wigner. On hidden variables and quantum mechanical probabilities. *Am. J. Phys.*, 38(8):1005–1009, August 1970.

[6] S. Grblacher, T. Paterek, R. Kaltenbaek, S. Brukner, M. Dotukowski, M. Aspelmeyer, and A. Zeilinger. An experimental test of non-local realism. *Nature*, 446:871–875, 2007.

[7] Stuart J. Freedman and John F. Clauser. Experimental test of local hidden-variable theories. *Phys. Rev. Lett.*, 28(14):938–941, April 1972.

[8] Alain Aspect, Philippe Grangier, and Gérard Roger. Experimental tests of realistic local theories via bell's theorem. *Phys. Rev. Lett.*, 47(7):460–463, August 1981.

[9] Alain Aspect, Philippe Grangier, and Gérard Roger. Experimental realization of einstein-podolsky-rosen-bohm gedankenexperiment: A new violation of bell's inequalities. *Phys. Rev. Lett.*, 49(2):91–94, July 1982.

[10] Emilio Santos. Critical analysis of the empirical tests of local hidden-variable theories. *Phys. Rev. A*, 46(7):3646–3656, October 1992.

[11] Alain Aspect, Jean Dalibard, and Gérard Roger. Experimental test of bell's inequalities using time- varying analyzers. *Phys. Rev. Lett.*, 49(25):1804–1807, December 1982.

[12] Gregor Weihs, Thomas Jennewein, Christoph Simon, Harald Weinfurter, and Anton Zeilinger. Violation of bell's inequality under strict einstein locality conditions. *Phys. Rev. Lett.*, 81(23):5039–5043, December 1998.

[13] M. A. Rowe, D. Kielpinski, V. Meyer, C. A. Sackett, W. M. Itano, C. Monroe, and D. J. Wineland. Experimental violation of a Bell's inequality with efficient detection. *Nature*, 409:791–794, 2001.

[14] J Volz. *Atom-Photon Entanglement.* PhD thesis, Ludwigs-Maximilians-Universität München, 2006.

[15] M. Weber. *Quantum Optical Experiments towards Atom Photon Entanglement.* PhD thesis, Ludwigs-Maximilians-Universität München, 2005.

[16] B. B. Blinov, D. L. Moehring, L.-M. Duan, and C Monroe. Observation of entanglement between a single trapped atom and a single photon. *Nature*, 428:153, 2004.

[17] Jürgen Volz, Markus Weber, Daniel Schlenk, Wenjamin Rosenfeld, Johannes Vrana, Karen Saucke, Christian Kurtsiefer, and Harald Weinfurter. Observation of Entanglement of a Single Photon with a Trapped Atom. *Phys. Rev. Lett.*, 96(3):030404–4, January 2006.

[18] T. Wilk, S. C. Webster, A. Kuhn, and G. Rempe. Single-atom single-photon quantum interface. *Science*, 317(5837):488–490, July 2007.

[19] D. L. Moehring, P. Maunz, S. Olmschenk, K.C. Younge, D.N. Matsukevich, L.-M. Duan, and C. Monroe. Entanglement of single-atom quantum bits at a distance. *Nature*, 449:68–72, 2007.

[20] Jian-Wei Pan, Dik Bouwmeester, Harald Weinfurter, and Anton Zeilinger. Experimental entanglement swapping: Entangling photons that never interacted. *Phys. Rev. Lett.*, 80(18):3891–3894, May 1998.

[21] J. N. Damask. *Polarization Optics in Telecommunications.* Springer Science+Business Media, Inc, 2004.

[22] E Hecht. *Optik.* Oldenburg Wissenshaftsverlag GmbH, 2001.

[23] Alexander Ling, Kee Pang Soh, Antia Lamas-Linares, and Christian Kurtsiefer. Experimental polarization state tomography using optimal polarimeters. *Phys. Rev. A*, 74(2):022309–7, August 2006.

[24] R. M. A. Azzam, I.M. Elminyawi, and El-Saba A. M. General analysis and optimization of the four-detector photopolarimeter. *J. Opt. Soc. Am. A*, 5:681–689, 1988.

[25] M Nielsen and I Chuang. *Quantum Computation and Quantum Information.* Cambridge university press, 2000.

[26] A. Einstein, B. Podolsky, and N. Rosen. Can quantum-mechanical description of physical reality be considered complete? *Phys. Rev.*, 47(10):777–780, May 1935.

[27] N. Bohr. Can quantum-mechanical description of physical reality be considered complete? *Phys. Rev.*, 48(8):696–702, October 1935.

[28] E. Schrödinger. Die gegenwärtige Situation in der Quantenmechanik. *Die Naturwissenschaften*, 23:807–812;823–828;844–849, 1935.

[29] C. S. Wu and I. Shaknov. The angular correlation of scattered annihilation radiation. *Phys. Rev.*, 77(1):136, January 1950.

[30] J. S. Bell. On the Einstein-Podolsky-Rosen Paradox. *Physics*, 1:195–200, 1964.

[31] R. Grimm, M. Weidemller, and Ovchinnikov Y. B. Optical dipole traps for neutral atoms. *Advances in Atomic, Molecular and Optical Physics Vol. 42, 95-170 (2000)*, 42:95–170, 2000.

[32] H.J. Metcalf and P. van Straten. *Laser Cooling and Trapping.* Springer, New York, Berlin, Heidelberg, 1999.

[33] N. Schlosser, G. Reymond, I. Protsenko, and P. Grangier. Sub-poissonian loading of single atoms in a microscopic dipole trap. *Nature*, 411:1024–2027, 2001.

[34] N. Schlosser, G. Reymond, and P. Grangier. Collisional blockade in microscopic optical dipole traps. *Phys. Rev. Lett.*, 89(2):023005, June 2002.

[35] J.D. Jackson. *Classical electrodynamics.* Wiley, New York, 1962.

[36] N. V. Vitanov and S. Stenholm. Analytic properties and effective two-level problems in stimulated raman adiabatic passage. *Phys. Rev. A*, 55(1):648–660, January 1997.

[37] Charles H. Bennett, Gilles Brassard, Claude Crépeau, Richard Jozsa, Asher Peres, and William K. Wootters. Teleporting an unknown quantum state via dual classical and einstein-podolsky-rosen channels. *Phys. Rev. Lett.*, 70(13):1895–1899, March 1993.

[38] D. Bouwmeester, J.-W. Pan, K. Mattle, M Eibl, H. Weinfurter, and A. Zeilinger. Experimental quantum teleportation. *Nature*, 390:575–579, 1997.

[39] C. K. Hong, Z. Y. Ou, and L. Mandel. Measurement of subpicosecond time intervals between two photons by interference. *Phys. Rev. Lett.*, 59(18):2044–2046, November 1987.

[40] T Legero. *Zeitaufgelöste Zwei-Photonen-Interferenz*. PhD thesis, Technische Universitt Mnchen, 2005.

[41] D.F. Walls and G.J. Milburn. *Quantum Optics*. Springer-Verlag Berlin and Heidelberg GmbH & Co. K, 1994.

[42] *Pohlner, R. private communication*, 2007.

[43] M Krug. Atomic traps for efficient state detection of a single atom. Master's thesis, Ludwigs-Maximilians-Universität München, 2007.

[44] M. S. Scully, Mand Zubairy. *Quantum optics*. Cambridge university press, 1997.

[45] K. J. Blow, Rodney Loudon, Simon J. D. Phoenix, and T. J. Shepherd. Continuum fields in quantum optics. *Phys. Rev. A*, 42(7):4102–4114, October 1990.

Danksagung

An dieser Stelle möchte ich mich herzlich bei allen bedanken, die mich über die ganze Zeit hinweg unterstützt haben und die zum Entstehen dieser Diplomarbeit beigetragen haben:

- meinen Eltern für ihre ständige Unterstützung, sowohl finanziell, als auch moralisch.
- Harald Weinfurter für die freundliche Aufnahme in seine Gruppe.
- Jürgen Volz für die vielen hilfreichen Diskussionen und sein unglaubliches Verlangen nach Kuchen.
- Markus Weber für seine gute Laune und seinen Optimismus.
- Wenjamin Rosenfeld für seine Betreuung und seine Geduld mit mir, dank dir ich habe viel gelernt.
- Florian Henkel, der mir gerade am Anfang viele Grundlagen im Labor vermittelt hat.
- Henning Weier für die Hilfe beim Programmieren und die inneren Fette.
- Daniel Schlenk, Chunlang Wang und Henning Weier für die lustige Zeit im Büro und dafür, dass ihr mir so viel geholfen habt.
- Fürst Martin für seine Hilfe beim Einlesen von Spannungen.
- Michael Krug für die amüsanten Stunden im Labor.
- Christian Jakob und Andreas Deeg, dafür das (ungewollt?) lustigste Duo zu sein.
- Gabi, Nicole und Toni für die Hilfe in allen Verwaltungs-, Technik- und Elektronikfragen.
- Anuschka für deine Geduld mit mir und dafür, dass du für mich da bist.
- allen Freunden, die mich in und neben dem Studium unterstützt haben. Ohne euch wäre ich nichts.

Erklärung

Hiermit versichere ich, dass ich die vorliegende Arbeit selbständig und nur unter Verwendung der angegebenen Quellen und Hilfsmittel verfaßt habe.

München, den 2. Oktober 2007

Fredrik Hocke